Theory and modelling of organic molecules on surfaces

Thesis submitted in accordance with the requirements of
the University of Liverpool for the degree of Doctor in Philosophy
by
N. Jonas L. Björk

November 30, 2010

Theory and modelling of
organic molecules on surfaces

JONAS BJÖRK

"Jag är just den plats / där skapelsen arbetar på sig själv"

"I am the place / where creation is working itself out"

From Tomas Tranströmer's poem Posteringen (The Outpost), 1973.

Preface

This thesis covers the work I have performed since the 1st of October 2007 in the research group of Mats Persson at the Surface Science Research Centre, University of Liverpool. My work as a PhD student has involved theoretical modelling of molecular systems adsorbed on surfaces. Throughout the text, results from various experiments will appear. These experiments were not carried out by me, but by experimental partners, as stated in the beginning of each chapter, or found in literature in which case it is clearly stated in the text.

If not stated otherwise, the results presented in this thesis were obtained by me during my time as a PhD student at the University of Liverpool.

Jonas Björk
Liverpool November 30, 2010

Abstract

In this thesis intermolecular interactions as well as the interplay between molecule and surface are studied within the framework of density functional theory (DFT) for molecular surface structures. A brief introduction to the research carried out on molecular adsorption is given in Chapter 1, and points out how DFT can be used as a potential tool for characterisation of experimental results, something which will be further illustrated in Chapters 4 and 5. The introductory chapter also points out one of the main challenges of DFT today, namely the missing van der Waals interactions and the possible ways these interactions can be accounted for.

The theoretical methods used in this thesis are described in Chapter 2. Chapter 3 introduces the techniques behind the experimental results presented together with the theoretical results in Chapters 4 and 5. Furthermore, this chapter discusses how the experimentally measurable quantities can be modelled within the framework of DFT.

In Chapter 4 molecular structures formed through self-assembly on the Cu(111) surface are investigated, by either the 1,3,8,10-tetraazaperopyrene (TAPP) or 4,9-diaminoperylene-quinone-3,10-diimine (DPDI) molecules as building blocks. After deposition on the Cu(111) surface both molecules are able to form long-range ordered porous surface structures upon annealing of the surface, as observed in scanning tunnelling microscopy (STM) experiments. Through a theoretical DFT study together with results from x-ray photoelectron spectroscopy (XPS) and x-ray standing wave absorption (XSW) experiments it is concluded that the DPDI molecules dehydrogenate upon formation of the network and that the molecules in both networks are coordinated to adatoms thermally generated from the copper substrate. The coordination between molecules and adatoms give rise to a characteristic unoccupied electronic state which is observable as a fingerprint in STM. Furthermore, the nature of coordinative bonding in the two networks is characterised by lowering of lone-pair orbitals centred on nitrogen atoms, as well as charge transfer to the lowest unoccupied molecular orbitals, of the molecules.

Chapter 4 also discusses the covalently linked one-dimensional chains that are formed after annealing of the porous TAPP network. It is found that the chains are formed through a dehydrogenation of the TAPP molecule, and as for the porous network, the TAPP chains are coordinated to copper adatoms.

The last part of Chapter 4 investigates effect of non-local dispersion forces on the structures of the porous networks formed by either TAPP or DPDI as well as the single DPDI molecule

adsorbed on Cu(111). The first-principles van der Waals density functional (vdW-DF) and the semi-empirical correction scheme by Grimme are used as corrections to semi-local DFT. From comparison of the adsorption heights of the molecules above the first Cu layer with data from XSW experiments it is concluded that both the semi-empirical Grimme correction and a modified vdW-DF give fair results for the two adatom-coordinated structures, and that the Grimme correction gives the overall best description of the adsorption height of these molecules.

Chapter 5 deals with the adsorption of the 2,2,5,5-tetramethyl-3-carboxypyrrolidine nitroxide (3CP) molecule on the Cu(110) surface. The 3CP molecule is a free radical due to an un-paired electron in the NO-group of the molecule. The chemically reactive NO-group is protected by four methyl groups preventing it from interacting with other molecules as well as the Cu substrate. From DFT calculations of total energies and infrared absorption spectra, in combination with reflection absorption infrared spectroscopy experiments, conclusions are made about the adsorption geometry of the molecule. It is shown that at room temperature the 3CP molecule deprotonates and adsorbs through a resulting carboxylate group to the surface. In this adsorption configuration the NO-group is pointing in an almost perpendicular direction away from the surface. Finally, DFT calculations predict that the un-paired spin survives the adsorption of the molecule on the surface. In other words, the 3CP molecule is still a radical upon adsorption on the Cu(110) surface.

In Chapter 6 the adsorption of model polyaromatic hydrocarbons on graphene is studied as a prototypical system for π-π stacking. To account for dispersion interactions, the first-principles van der Waals density functional is compared with four semi-empirical corrections to density functional theory as well as two empirical force fields. It was found that the van der Waals density functional gives the most accurate description of binding energies, compared to available experimental data from literature. Comparison of the dispersive vs. electrostatic contributions to the total binding energies for the aromatic molecules suggests that the attractive part of π-π interactions can be regarded as being prevalently dispersive in nature at large separations, while close to the equilibrium bonding distance it is a complex interplay between dispersive and electrostatic Coulomb interactions. Furthermore the results indicate that the magnitude of π-π interactions normalised both per total atoms or carbon atoms increases significantly with the relative number of hydrogen atoms in the studied systems.

Contents

Abbrevations

3CP	2,2,5,5-tetramethyl-3-carboxypyrrolidine nitroxide
DPDI	4,9-diaminoperylene-quinone-3,10-diimine
DFT	Density functional theory
GGA	Generalized gradient approximation
HOMO	Highest occupied molecular orbital
LDA	Local density approximation
LDOS	Local density of states
LEED	Low-energy electron diffraction
LUMO	Lowest unoccupied molecular orbital
MO-PDOS	Molecular orbital projected density of states
NIXSW	Normal incident x-ray standing wave
PAH	Polycyclic aromatic hydrocarbons
PBE	Perdew-Burke-Ernzerhof
PBE-vdW	PBE based vdW-DF
RAIRS	Reflection absorption infrared spectroscopy
revPBE	Revised Perdew-Burke-Ernzerhof
revPBE-vdW	revPBE based vdW-DF
STM	Scanning tunneling microscopy
STS	Scanning tunneling spectroscopy
TAPP	1,3,8,10-tetraazaperopyrene
TPD	Temperature dependent desorption
UHV	Ultrahigh vacuum
vdW-DF	van der Waals density-functional
XC	Exchange-correlation
XPS	X-ray photoelectron spectroscopy
XSW	X-ray standing wave

Chapter 1

Introduction

1.1 Brief historical overview

Research of molecular adsorption on surfaces is a key area in surface science. The most significant contribution to society probably being heterogeneous catalysis [1,2] which was acknowledged most recently in the 2007 Nobel Prize in chemistry awarded to Gerhard Ertl. The whole field of surface science was in fact pioneered by research on heterogeneous catalysis, by scientists like Paul Sabatier who studied the hydrogenation of organic molecules using catalysts and Fritz Haber who was the first to synthesise ammonia from its elements. Sabatier's and Haber's contributions to the field are reflected in the Nobel Prizes in chemistry in 1912 and 1918, respectively. One of the most influential innovators for surface science in the early 20th century was however Irving Langmuir, who for example performed studies on the work function on metals, heterogeneous catalysis and adsorption kinetics. Furthermore, together with Katherine Blodgett he explored thin films and molecular adsorption [3]. In 1932 Langmuir was awarded a Nobel Prize in chemistry *"for his discoveries and investigations in surface chemistry"* [4].

Much of todays research of molecular adsorbates on surfaces were foreseen by Richard Feynman in his famous talk *"There's plenty of room at the bottom"* 1959, where he considered the possibility of direct manipulation of atoms and molecules. One of the most influential contributions to modern surface science came more than 20 years later; the design and demonstration of the scanning tunnelling microscope (STM) by Gerd Binnig and Heinrich Rohrer for which they were awarded the 1986 Nobel Prize in physics. The STM technique allowed for the first time real-space imaging [5] as well as manipulation [6] of surface structures at the atomic scale, hence realising Feynman's vision and revolutionising surface science.

Finally, during the last decade it has become possible to study adsorption of organic molecular systems on surfaces with first principles computational modelling. This is thanks to the development of density functional theory in the 60s by Pierre Hohenberg, Walter Kohn and Lu Jeu Sham [7,8] and more recent development of so called exchange-correlation functionals [9–11], in combination with powerful parallelised computational resources. Walter Kohn was in fact awarded the Nobel Prize in chemistry *"for his development of density functional*

theory" in 1998 [4]. The work presented in this thesis is highly dependent on the contributions by Kohn and his co-workers.

1.2 Organic molecules on surfaces

In this thesis the adsorption of organic molecules on surfaces will be studied, both by considering ordered surface structures as well as single molecular adsorption. Studies of organic molecules on surfaces have several applications, ranging from heterogeneous catalysis to light harvesting in organic-inorganic photo-voltaic devices [12], and in futuristic devices such as spintronics, molecular electronics, data storage [13, 14] and quantum computers [15]. For devices making use of the properties of single molecules it becomes important to understand from a fundamental level how molecules interact with the surface and with other molecules adsorbed on the surface.

By studying single molecules adsorbed on surfaces it is possible to learn about the adsorption process itself without having to consider the effect from interactions with other molecules. Such studies involve both simple systems such as carbon monoxide adsorbed on the Pt(111) surface [16, 17] and H_2 dissociation over the Cu(111) surface [18] and more complicated molecules [19], for example porphyrin complexes [20]. These studies also include the adsorption of molecules with some kind of function, like molecular switches [21, 22], so called "nanocars" [23], and molecular magnets [24–26]. The latter one will be illustrated with an example in Chapter 5.

Many studies concern not only single molecules adsorbed on surfaces, but rather the interactions between the molecules on a surface. Surface science has for example made it possible to study fundamental processes in nature, such as the nucleation of water molecules into ice crystals [27, 28], and enantioselective phase separation of racemic mixtures of chiral molecules [29]. A large area in surface science focuses on so called self-assembled monolayers which are often formed from sulfur-containing species, for example thiols sulfides and disulfides, on gold substrates [30, 31].

The surface does not only act as a support where functionalised molecules can adsorb, but the surface itself has inherent properties that can be more or less controlled by molecular adsorption. For example the free-electron like surface states on the Ag(111) and Cu(111) surfaces have been found to be tuneable by monolayer and sub monolayer coverages of molecules in ordered structures [32–37]. Furthermore, it has been shown that the probability of molecular adsorption within a porous network follows the distribution of the confined surface state in a cavity [36].

In this thesis much of the attention will be drawn towards long-range ordered porous surface structures, in which organic molecules are used as building blocks in sparsely packed nanomeshes. Such nanoporous networks can for example serve as a template for adsorption of functionalised guest molecules. The basic principle is illustrated in Figure 1.1. A porous network template of organic molecules is formed through self-assembly on a surface. Func-

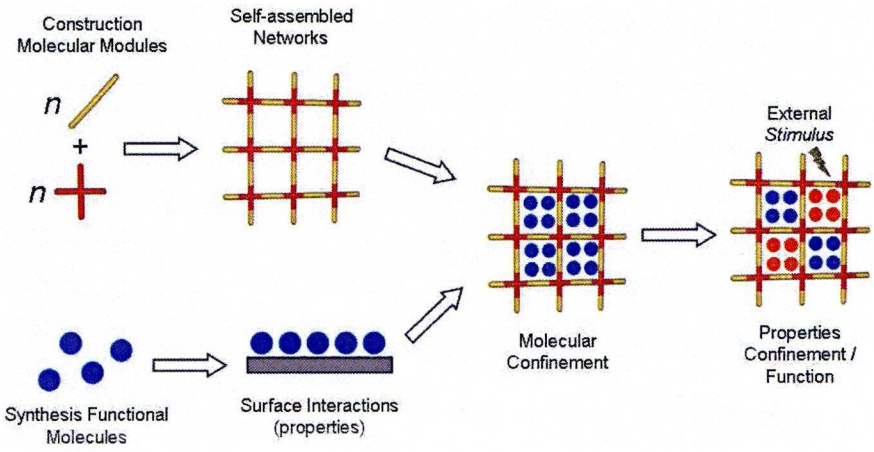

Figure 1.1: Basic principle of how nano-porous networks can be used to tailor functionalised surface structures. The porous surface network is able to host and confine the motion of functionalised guest molecules, creating an array of separated functionalisations on the surface. By external stimulus the functionalisations can be attributed different properties. From European Union MRTN-CT-2006-035810 grant proposal.

tionalised guest molecules or atoms are deposited onto the surface, and the porous template confines lateral movement of these adsorbates. In this way well-defined structures of functionalised molecules separated from each other can be formed. In princple, by applying external stimulus inside the pores the properties of the functional groups can be altered. Such a property would have future applications in for example data storage [13]. A realisation of this principle has been illustrated by Wintjes and co-workers [38] who were able to create a multiposition rotary device by adsorption of porphyrins in a porous network. It was shown in STM experiments that the alignment of a porphyrin within a pore can be switched by applying a voltage pulse with the STM tip. Other functionalised adsorbates inside the pores could be represented by for example azobenzene derivatives [39] (which can be switched between cis and trans configurations) and magnetic atoms or molecules.

Molecular surface-structures can effectively be formed through self-assembly of organic building blocks. In this process the molecules spontaneously organise under adequate conditions, for example by annealing at a certain temperature. The self-organisation is possible due to the inherent self-recognition of the adsorbed molecules, and the size and shape of the networks can be controlled by designing molecules with different size and functionality. The structure of a self-assembled network also depends on the molecule-surface interaction; hence by depositing the molecules on different surfaces it is possible to influence the structure of the final product. For example small coverages of water molecules on Cu(110) organise into one-dimensional chains consisting of pentagons whereas on Ag(110) instead chains consisting of hexagons are favoured [27]. Other essential parameters to control the self-assembly include the distribution of defect sites (steps, kinks, adatoms) which affect nucleation, temperature during the molecular deposition, temperature and duration of the post annealing process as well as the

surface concentration of molecules.

One of the basic methods for tailoring networks of different size and shape by self-assembly is through mastering the intermolecular interactions. The principle originates from supramolecular chemistry [40] and the idea is to synthesise molecules in such way that they interact with each other in a preferred direction via functional groups. The crystal nucleation of the molecules is then controlled on the level of molecular synthesis, and different structures can be formed by directing the molecular interactions. Self-assembly into ordered patterns due to directed intermolecular interactions is often referred to as molecular recognition [40]. Molecular recognition is nothing invented by man, but rather a way of mimicking nature. For example the DNA double helix is a good example of self-assembly due to molecular recognition.

Most self-assembled structures reported in the literature are based on supramolecular chemistry, in other words non-covalent interactions are the driving forces between molecules. These inter-molecular interactions are in many systems characterised by hydrogen bonding [41–46]. For example porous structures formed by trimesic acid molecules [41] as well as two-component networks of melamine and uracil derivatives [42,43] have been observed on graphite. Furthermore, various architectures formed by melamine and PTCDA have been observed on the Au(111) by tuning the molecular ratio between the two components [46]. Also networks stabilised by van der Waals interactions exist [47]. These systems are often characterised by close-packed networks, but also porous network structures can be found in literature [47]. Finally, in supramolecular chemistry the intermolecular interactions can be mediated by metal atoms, in which coordination bonds between metal centres and organic ligands drive the formation of networks [48]. This type of network will be discussed further in the following section.

In recent years quite a few studies have focused on the possibility of covalently linking molecules into one-dimensional [49, 50] as well as two-dimensional [50, 51] macromolecular structures. For example it has been possible to covalently link porphyrin derivatives to build nanoarchitectures in both one and two dimensions on the Au(111) surface [50]. Another example is the 1,3,9.10-tetraazaperylene molecule on the Cu(111) which forms covalently linked molecular chains at elevated temperatures [49]. The chemical nature of these chains is the subject of section 4.4 of this thesis. Covalent interactions allow for much stronger networks to be formed. The major drawback of using covalent interactions as driving force for the self-assembly is the missing self-correction which is inherent to reversible non-covalent interactions [52]. A major challenge of forming especially long-range ordered two-dimensional covalent networks is to deal with the problem of the missing self-correction.

1.3 Metal-organic coordination networks

The concept of metal-organic coordination networks in surface science [48, 53, 54] is normally used to describe ordered networks of organic molecules coordinated to metal centres. The metal-ligand bonding as driving mechanism for the self-assembly has been used both for the formation of two-dimensional [49, 53–57] and one-dimensional [58, 59] structures. Due to

the reversibility (self-correction) of the coordination bond it has been possible to form highly ordered two-dimensional networks over large areas. Furthermore, metal-organic coordination networks have shown a high thermal stability and are stable well above room temperature [60, 61], in special cases up to 450 °C [62]. This last example is one of the networks which is studied in more detail in Chapter 4 where for example the origin of this extra-ordinary stability will be discussed.

There have been many examples of two-dimensional porous metal-organic coordination networks [49,60–62]. In these examples the organic molecules coordinated to the metal centres can be seen as linker units. A nice example of network control through molecular design has been illustrated by depositing linker molecules of various length, but the same functionality, resulting in honeycomb nanomeshes with tuneable cavity size [55].

Metal-organic coordination gives the possibility of creating ordered porous structures in networks, where the pores can host organic molecules by confining their lateral motion on the surface. Also, the metal centres supporting the organic ligands can themselves have interesting properties. It has been found that these adatoms can have peculiar electronic and magnetic properties for potential applications in for example heterogeneous catalysis. It has for example been suggested from a DFT study that the Fe adatoms coordinating terephtalic acid molecules on the Cu(100) surface have unusual magnetic properties [63]. Furthermore, Pawin and co-workers have shown that the Cu adatoms in a coordination network on Cu(111) are negatively charged, a property which generally does not occur [64].

The substrates on which metal-organic coordination networks are formed vary, but normally transition metals are used. Furthermore, the metal centres/adatoms used to coordinate the molecules vary and can be divided into two groups: *Native* adatoms which originate intrinsically from the metal substrate or *non-native* adatoms which are foreign atoms deposited onto the substrate.

1.3.1 Identifying the adatoms

Non-native adatoms are of different chemical species to the substrate atoms. This is for example the case for the terephtalic acid molecules coordinated to Fe adatoms [63] on the Cu(100) surface (see above), and in several other systems [53, 55, 56]. As this group of adatoms has to be vapour-deposited onto the substrate, it is possible to study the self-assembly both in the presence and absence of the adatoms while keeping other parameters, such as temperature, fixed; therefore, *non-native* adatoms provide an unambiguous method of proving the role of adatoms in the self-assembly, which is a much greater challenge for *native* adatoms, which are thermally generated from the substrate.

The other group is represented by systems where native adatoms are generated intrinsically from the substrate by thermal annealing. For example, the herringbone reconstruction of the Au(111) surface has shown [65, 66] to serve as a source of reactive Au adatoms that subsequently can coordinate to molecules such as thiolate species deposited on the surface.

Furthermore, several cases have been reported [64, 64, 67–70] where free Cu adatoms are generated from steps on Cu surfaces, and consequently coordinate to organic molecules. For example, adatoms have been reported from an STM study to coordinate benzoate molecules on the Cu(110) surface [70]. Furthermore, trimesic acid molecules have been found to be coordinated to Cu adatoms on the Cu(100) surface [67, 68] as well as on the Cu(110) surface [69]. Finally, adatoms have also been found to take part on the Cu(111) surface in the formation of networks build up by 9,10-anthracenedicarbonitrile molecules [64].

The formation of bonds between organic ligands and metal adatoms is highly dependent on the concentration of free adatoms on the terraces, which is controlled by the temperature of the substrate. However, the temperature also has a great influence on other parameters, such as the mobility of the adsorbed molecules as well as the surface concentration of molecules. It is therefore a challenge to study how the native adatoms affect the self-assembly, while keeping other parameters which also affect the self-assembly, such as the temperature, fixed. In many studies based on analysing topographic STM images it was concluded that the adatoms are coordinated to the organic adsorbates. However, the adatoms cannot always be seen topographically in STM, and other methods for making conclusions about the adatoms taking part in the self-assembly are needed. In section 4.3 a novel approach for identifying native adatoms in metal-organic coordination networks will be presented.

1.4 Combined theoretical and experimental approach

What will be illustrated in Chapter 4 and 5 is that modelling of organic molecules on surfaces from first principles can give additional information and help the interpretation of experimental data. The strength of using theory as an interpretation tool is that it works from a different starting point than experiments: While one in experiments builds models of a material by studying its properties, in theory one makes predictions about the properties given a model. In other words, in the first principles approach the model is already known (or assumed) but the properties unknown, while in experiments it is the other way around. This section aims to briefly introduce modern modelling tools as well as experimental techniques used in surface science. For more details of the particular techniques used in this thesis see Chapter 2 for the theory and Chapter 3 for the experiments.

1.4.1 Theoretical modelling techniques

Molecular modelling stretches across several research fields, and there are consequently several levels of theories in which molecular modelling can be performed: There are first principles methods in which the properties of a molecule or material are predicted using only the coordinates and chemical elements of the atoms as input in the calculations. The first principles methods include for example wave function based methods such as coupled cluster, second order Møller Plesset perturbation theory (MP2), and Hartree-Fock. However, as the size of

the wave function grows linearly with respect to the number of electrons, these methods are intractable for the sizes of systems that will be considered in this thesis. Instead of treating a system within a wave function approach, in principle all the ground state properties of the system can be obtained from the electron density of the system. This is the very basic idea of density-functional theory (DFT). DFT is in principle exact in the ground-state of a system, but only if the universal form of the so called exchange-correlation functional would be known. This will be further discussed in Chapter 2. Other computational methods include for example the tight binding model which is a special case of DFT, and force field methods, in which the interactions between the atoms are parameterised within an analytical formula. Since the force-field methods are based on parameterisations there is always a question about how transferable these methods are.

Often the size of the studied system puts limits on which method one can use. The more accurate theory, the more costly the calculation will be. For the size of the surface systems treated in this thesis, DFT gives a good compromise between computational accuracy and efficiency. Therefore this method has been used for obtaining the results in this thesis. In DFT the crucial approximations are hidden in the exchange-correlation (XC) functional. The standard today is semi-local DFT using the so called generalised gradient approximation (GGA) in which not only the density, but also the gradient of the density enters the XC-functional. The GGA functional has had a great amount of success describing bulk materials, internal structure of molecules as well as adsorption of atoms and small molecules on surfaces. One of the main drawbacks of semi-local DFT is the absence of non-local correlation interactions, usually referred to as non-local dispersion or van der Waals (vdW) interactions. These interactions are of major importance in sparsely packed systems, such as molecular crystals and biological systems, and can also play a crucial role for the adsorption of planar organic molecules on surfaces, even for chemisorbed species. For example it has been shown that vdW interactions are crucial for the 3,4,9,10-perylene-tetracarboxylic acid dianhydridie (PTCDA) molecule to chemisorb to the Cu(111) surface since these without these interactions the molecule is at a distance above the surface where no chemisorption occurs [71]. Therefore, it becomes obvious that for the molecules (very similar to PTCDA) that will be presented in Chapter 4 we have to account for vdW interactions, but it is less obvious how it can be done.

During the last decade several methods accounting for the vdW interactions in DFT calculations have become available [11, 72–80]. These methods include both non-local density functionals [11, 72–75], which are introduced in subsection 2.2.3, and semi-empirical corrections to DFT [76–80], which are introduced in subsection 2.2.4. Also high level quantum chemistry methods exist [17, 81], but remain too numerically expensive for the systems studied in this thesis. Due to the many available methods accounting for the vdW interactions, together with the very limited number of studies comparing the different methods in an unbiased fashion, it is not clear which method to choose when facing a new problem. Hence, benchmarking studies are needed, motivating two of the studies in this thesis: Section 4.5 studies

the structural changes imposed by different corrections for perylene derivatives on the Cu(111) surface in comparison with experimental data. In chapter 6 the adsorption energy of polycyclic aromatic hydrocarbons on graphene is thoroughly studied as a typical system for π-π interactions, and seven different methods for calculating the binding energy are benchmarked against calorimetric data from temperature programmed desorption experiments.

1.4.2 Experimental techniques

Experiments are generally done on well-defined clean flat surfaces under ultrahigh vacuum conditions. In surface science there is a whole range of experimental techniques available which can be used to gain different kinds of information of a system:

Scanning probe microscopy methods, such as scanning tunnelling microscopy and atomic force microscopy, give different types of information on the electronic structure of a system. Chemical information of atoms can be obtained through core-level binding energies using photoelectron spectroscopy techniques and from vibrational frequencies using infrared absorption, electron energy loss spectroscopy and inelastic tunnelling spectroscopy techniques.

Adsorption height of atomic species can be obtained from X-ray standing wave absorption and further information about the structure of adsorbed molecules can be obtained from the near-edge X-ray absorption fine structure technique. Surface structure and lattice dynamics of a material can be determined from helium atom scattering experiments, and low-energy electron diffraction can be used to gain information about the periodicity of superstructures, which will be used for building the unit cells of different models. The band structure resulting from the periodicity of a structure can be measured by angle-resolved photoemission spectroscopy. Finally, results from temperature programmed desorption experiments can be used to obtain for example binding energies of adsorbates on surfaces.

Having all these experimental techniques in mind, one can question whether theory can add any new information about a system. However, as we will illustrate in Chapter 4 and 5 the information obtained from experimental observations can only get scientists to a certain point due to the many plausible models that can be made from one set of experiments. By reproducing the experimental observations from theory for a certain model, we can with more confidence be sure that the model does indeed give a realistic atomistic picture of the system. Furthermore, theory can be used as a powerful tool for predicting properties of materials where experiments are less feasible, such as for interstellar materials and in geology. Finally, it can predict properties of materials not yet synthesised, and hence be used for discovering new materials.

Chapter 2

Theory and methodology

In order to obtain a microscopic description of the interactions taking place between molecules, as well as molecules with surfaces, we first apply the Born-Oppenheimer approximation in order to separate the electronic and nuclear motions. The fast electronic motion is assumed to follow instantaneously the slow nuclear motion so that the many-electron ground state follows adiabatically the nuclear motion. For each set of coordinates of the nuclei one must then in principle solve the time-independent many-body Schrödinger equation for the ground state of N interacting electrons, given by

$$\left\{ -\frac{1}{2}\sum_{i=1}^{N}\nabla_i^2 + \sum_{i>j}\frac{1}{|\vec{r}_i - \vec{r}_j|} + \sum_{i=1}^{N} v_{\text{ext}}(\vec{r}_i) \right\} \Psi(\vec{r}_1, \vec{r}_2, ..., \vec{r}_N) = E\Psi(\vec{r}_1, \vec{r}_2, ..., \vec{r}_N). \quad (2.1)$$

The ground state is then governed by a potential energy given by the ground state energy E. Since the dimension of the wave function grows as $3N$ the computational effort grows very fast with number of electrons, making it intractable to handle any type of systems of interest in this thesis. Therefore one has to find an alternative method to simplify the mathematical description of the system. Nowadays the most successful and often used technique to solve the many-electron problem is based on density functional theory (DFT) by Hohenberg, Kohn and Sham. In DFT the interacting many-electron problem is replaced by a non-interacting electron problem, where the Coulomb interaction is replaced with an effective potential. The many-electron wave function is replaced by the electron density, reducing the problem in $3N$ dimensions to a problem of N one-electron problems.

In this chapter we will introduce some of the basics of DFT, how DFT was implemented in the calculations and the general functionals we have used in our calculations. For a more complete introduction to DFT see for example "The ABC of DFT" by Kieron Burke [82]. We will also introduce different methods on how non-local dispersion forces can be included, both directly in DFT as well as a semi-empirical post-correction to DFT (the so called DFT+D).

2.1 Density-functional theory

2.1.1 The self-consistent Kohn-Sham equations

Hohenberg and Kohn [7] showed that the ground state energy of an inhomogeneous electron gas with density $n(\mathbf{r})$ in an external potential $v(\mathbf{r})$ can be written as

$$E[n] = \int d\mathbf{r}\, v(\mathbf{r})n(\mathbf{r}) + \frac{1}{2}\int d\mathbf{r}d\mathbf{r}' \frac{n(\mathbf{r})n(\mathbf{r}')}{|\mathbf{r}-\mathbf{r}'|} + G[n], \tag{2.2}$$

where the second term is the Hartree (or Coulomb) energy and $G[n]$ is an unknown universal functional of the electron density $n(\mathbf{r})$. The total energy $E[n]$ has a minimum for the correct ground state density.

It was later suggested by Kohn and Sham [8] that the functional $G[n]$ can be divided into the kinetic energy of a system of non-interacting electrons, $T_\mathrm{s}[n]$, with electron density $n(\mathbf{r})$ and the exchange-correlation (XC) energy of the interacting system, E_xc, with electron density $n(\mathbf{r})$:

$$G[n] \equiv T_\mathrm{s}[n] + E_\mathrm{xc}[n]. \tag{2.3}$$

Equation (2.2) then becomes

$$E[n] = T_\mathrm{s}[n] + \int d\mathbf{r}\, v(\mathbf{r})n(\mathbf{r}) + \frac{1}{2}\int d\mathbf{r}d\mathbf{r}' \frac{n(\mathbf{r})n(\mathbf{r}')}{|\mathbf{r}-\mathbf{r}'|} + E_\mathrm{xc}[n], \tag{2.4}$$

in which all terms can be determined exactly, except the exchange correlation energy $E_\mathrm{xc}[n]$, for which several approximations exist, see Section 2.2. The external potential $v(\mathbf{r})$ describes the interaction between the electrons and the nuclei of the system.

The aim is now to minimise Eq. (2.4) with respect to the electron density under the constraint of a fixed number of electrons, in other words we want to find an electron density n that fulfils the equation

$$\frac{\delta E[n]}{\delta n(\mathbf{r})} = \frac{\delta T_\mathrm{s}[n]}{\delta n(\mathbf{r})} + \varphi(\mathbf{r}) + \mu_\mathrm{xc}(\mathbf{r}) = \mu, \tag{2.5}$$

with

$$\varphi(\mathbf{r}) = v(\mathbf{r}) + \int d\mathbf{r}' \frac{n(\mathbf{r}')}{|\mathbf{r}-\mathbf{r}'|} \tag{2.6}$$

and

$$\mu_\mathrm{xc}\,(n) = \frac{\delta E_\mathrm{xc}}{\delta n(\mathbf{r})}, \tag{2.7}$$

is the exchange correlation contribution to the chemical potential of an electron gas with density $n(\mathbf{r})$. Equation (2.5) is the same equation one obtains for a system of non-interacting electrons moving in an external potential $\varphi(\mathbf{r}) + \mu_\mathrm{xc}\,(n(\mathbf{r}))$. Therefore, for given φ and μ_xc, one obtain the electron density n which fulfils (2.5) by solving the one-particle time-independent Schrödinger equation

$$\left\{-\frac{1}{2}\nabla^2 + [\varphi(\mathbf{r}) + \mu_{\text{xc}}(n(\mathbf{r}))]\right\}\psi_i(\mathbf{r}) = \epsilon_i\psi_i(\mathbf{r}) \tag{2.8}$$

with the electron density n given by

$$n(\mathbf{r}) = \sum_{i=1}^{N} |\psi_i(\mathbf{r})|^2, \tag{2.9}$$

where N is the total number of electrons.

Equations (2.6-2.9) need to be solved self-consistently, illustrated in Figure 2.1. One begins with an assumed electron density $n(\mathbf{r})$, from which $\varphi(\mathbf{r})$ and $\mu_{\text{xc}}(n(\mathbf{r}))$ are constructed using Eq. (2.6) and (2.7), respectively. A new electron density $n(\mathbf{r})$ is then found from Eq. (2.8) and (2.9). For each iteration the energy is calculated as

$$E = \sum_{i}^{N} \epsilon_i - \frac{1}{2}\int\int d\mathbf{r}d\mathbf{r}' \frac{n(\mathbf{r})n(\mathbf{r})}{|\mathbf{r}-\mathbf{r}'|} + E_{\text{xc}}[n] - \int d\mathbf{r}\, n(\mathbf{r})\mu_{\text{xc}}(n(\mathbf{r})). \tag{2.10}$$

The self-consistent loop is interrupted when the energy is converged, for example when the difference in energy from two (or more) consequent iterations is less than a break condition. The energy given by Eq. (2.10) after the last iteration is the ground state energy for the specific configuration of the nuclei.

2.2 Exchange-correlation (XC) functional

2.2.1 Local density approximation (LDA)

In the local density approximation (LDA) one assumes a slowly varying electron gas and approximates the XC-energy as

$$E_{\text{xc}}^{\text{LDA}}[n] = \int d^3r\, n(\mathbf{r})\epsilon_{\text{xc}}^{\text{hom}}(n(\mathbf{r})), \tag{2.11}$$

where $\epsilon_{\text{xc}}^{\text{hom}}(n(\mathbf{r}))$ is the XC-energy per electron for a homogeneous electron gas with density $n(\mathbf{r})$. This definition of the XC-energy is exact for the special case of a uniform jellium gas in which the electrons move in a uniform positive background chosen to preserve overall charge neutrality.

The homogeneous electron gas is characterised by a single parameter, r_{s}, and is defined as the radius of a sphere containing on average one electron

$$r_{\text{s}} = \left(\frac{3}{4\pi n}\right)^{1/3} = \frac{1.919}{k_{\text{F}}}, \tag{2.12}$$

where k_{F} is the Fermi wavevector, which for the uniform electron gas is given by

$$k_{\text{F}} = (3\pi^2 n)^{1/3}. \tag{2.13}$$

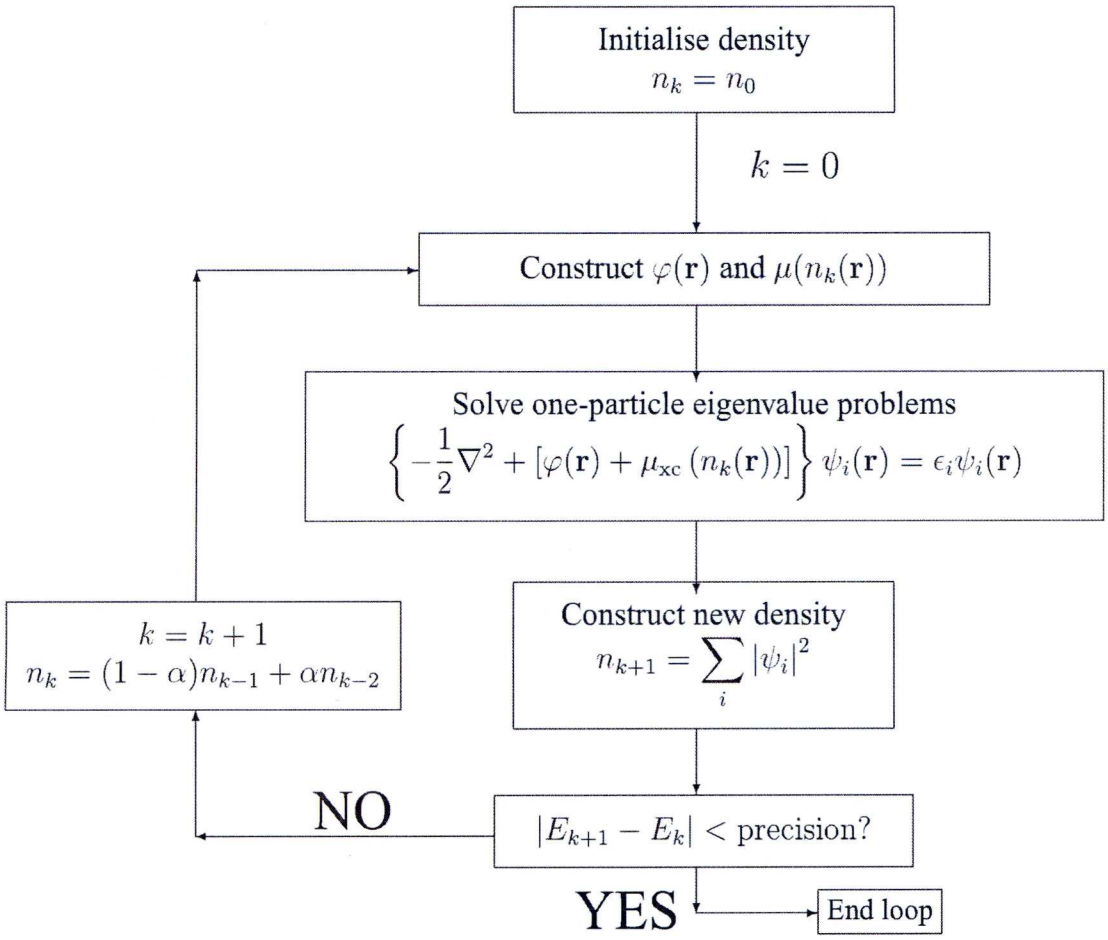

Figure 2.1: The very basic of the self-consistent algorithm of finding the minimum energy with respect to the electron density within the framework of Kohn-Sham DFT.

The total XC-energy can be divided into individual contributions of exchange and correlation as

$$E_{\mathrm{xc}}^{\mathrm{LDA}} = E_{\mathrm{x}}^{\mathrm{LDA}} + E_{\mathrm{c}}^{\mathrm{LDA}} \tag{2.14}$$

The LDA exchange energy is given by

$$E_{\mathrm{x}}^{\mathrm{LDA}}[n] = \int d^3r\, n(\mathbf{r})\epsilon_{\mathrm{x}}^{\mathrm{hom}}(n(\mathbf{r})), \tag{2.15}$$

where $\epsilon_{\mathrm{x}}^{\mathrm{hom}}(n(\mathbf{r}))$ is the exchange energy per electron in the uniform gas given by

$$\epsilon_{\mathrm{x}}^{\mathrm{hom}}(n(\mathbf{r})) = A_{\mathrm{x}} n^{1/3} \tag{2.16}$$

with $A_{\mathrm{x}} = -(3/4)(3/\pi)^{1/3} = -0.738$. Finally, the correlation energy is given by

$$E_{\mathrm{c}}^{\mathrm{LDA}}[n] = \int d^3r\, n(\mathbf{r})\epsilon_{\mathrm{c}}^{\mathrm{hom}}(r_{\mathrm{s}}(\mathbf{r})), \tag{2.17}$$

where $\epsilon_{\mathrm{c}}^{\mathrm{hom}}(r_{\mathrm{s}})$ is the correlation energy per electron of the uniform gas. $\epsilon_{\mathrm{c}}^{\mathrm{hom}}(r_{\mathrm{s}})$ cannot be determined analytically except for the high- and low-density limits, where $r_{\mathrm{s}} \to 0$ and $r_{\mathrm{s}} \to \infty$, respectively. For intermediate values of r_{s}, accurate quantum Monte Carlo simulations have

been performed on the homogeneous electron gas [83]. These results have been used to derive approximate analytical forms of $\epsilon_{\mathrm{c}}^{\mathrm{hom}}(r_{\mathrm{s}})$ [84–86].

2.2.2 Generalised gradient approximation (GGA)

In the generalised gradient approximation (GGA) the exchange has the form

$$E_{\mathrm{x}}^{\mathrm{GGA}}[n] = \int d^3r\, \epsilon_{\mathrm{x}}^{\mathrm{hom}}(n(\mathbf{r}))F_{\mathrm{x}}(s(\mathbf{r})). \tag{2.18}$$

The factor F_{x} is the exchange enhancement factor, which tells how much exchange is enhanced over its LDA value. The parameter $s(\mathbf{r})$ is defined as

$$s(\mathbf{r}) = \frac{|\nabla n(\mathbf{r})|}{2k_{\mathrm{F}}n(\mathbf{r})}. \tag{2.19}$$

Hence, as the name suggests, GGA depends not only on the electron density, but also on the gradient of the density. This type of the gradient corrected DFT is often referred to as semi-local DFT.

The full exchange-correlation energy is written as (in the spin-unpolarised case)

$$E_{\mathrm{x}}^{\mathrm{GGA}}[n] = \int d^3r\, \epsilon_{\mathrm{x}}^{\mathrm{hom}}(n(\mathbf{r}))F_{\mathrm{xc}}(r_{\mathrm{s}}(\mathbf{r}), s(\mathbf{r})). \tag{2.20}$$

The enhancement factor has the limiting behaviours

$$F_{\mathrm{xc}}(r_{\mathrm{s}}, s=0) = F_{\mathrm{xc}}^{\mathrm{hom}}(r_{\mathrm{s}}), \qquad F_{\mathrm{xc}}(r_{\mathrm{s}}=0, s) = F_{\mathrm{x}}(s). \tag{2.21}$$

F_{xc} is often evaluated on analytical forms, which are designed to satisfy certain criterions, such as the correct uniform electron gas limit (recovering LDA for s=0) and the LDA linear response, or by fitting parameters to experimental data [87].

There exist several flavours of GGA, of which the Perdew-Wang 91 (PW91) [9], Perdew-Burke-Ernzerhofer (PBE) [10] and the revised form of PBE (revPBE) proposed by Zhang and Wang [88] have been used in this thesis.

2.2.3 The van der Waals density functional

Several versions of the van der Waals density-functional (vdW-DF) exist, in this work we are exclusively using the van der Waals density functional for general geometries introduced by Dion and coworkers 2004 [11], which also goes under the name of the *Langreth-Lundqvist* functional.

In the vdW-DF, the correlation energy is divided into two parts

$$E_{\mathrm{c}}[n] = E_{\mathrm{c}}^{0}[n] + E_{\mathrm{c}}^{\mathrm{nl}}[n]. \tag{2.22}$$

The first term is treated within LDA. This is according to the authors of Ref. [11] appropriate since the second term is designed to give the non-local correlation energy, which can be expressed as

$$E_c^{nl}[n] = \frac{1}{2}\int d^3r d^3r' n(\mathbf{r})\phi(\mathbf{r},\mathbf{r}')n(\mathbf{r}'), \tag{2.23}$$

where the kernel $\phi(\mathbf{r},\mathbf{r}')$ depends on $|\mathbf{r}-\mathbf{r}'|$ and the densities n close to $\mathbf{r}$ and $\mathbf{r}'$. The full derivation of the kernel $\phi(\mathbf{r},\mathbf{r}')$ can be found in Ref. [11], and is based on a model response function. The detailed form of this response function is still a subject of research [73].

In the vdW-DF the E_c^{nl} term is designed to take care of all non-local, including semi-local, contributions to the correlation energy. Hence, in the vdW-DF methodology the total *vdW-corrected* energy is given by

$$E_{vdW} = E_{GGA} - E_{c,GGA} + E_{c,LDA} + E_c^{nl}. \tag{2.24}$$

where $E_{c,GGA}$ is the correlation part of the GGA XC-energy, $E_{c,LDA}$ is the correlation energy given by LDA, and E_c^{nl} is the non-local correlation energy given by Eq. (2.23). Note that the GGA correlation energy is replaced by LDA correlation plus the non-local correlation energy. It was first suggested to use the revPBE-functional for GGA exchange-part since it has no non-physical bonding contribution in the exchange energy for purely dispersion bonded systems [89]. However later studies [74, 75] have suggested that other flavours of the GGA exchange energy may be better suited.

Both non-selfconsistent [11] and self-consistent implementations [72, 74, 75, 90, 91] of the vdW-DF exist. In a non-selfconsistent calculation the non-local correlation energy is calculated as a post-correction to the semi-local DFT calculation using the self-consistent GGA electron density as input.

For a self-consistent calculation the vdW-DF is included in the potential of each iteration in the self-consistent DFT calculation. The main advantage of the self-consistent approach is that the vdW-correction is not only included in the total energies, but also in the forces.

The most demanding part for calculating the non-local correlation energy in the vdW-DF scheme is evaluating the six-dimensional integral in Eq. (2.23). Several implementations for evaluating this integral are available [74, 75, 91]. For example it can be done from integration of the density on spherical Lebedev grids centred on each atom [74], or by making use of fast Fourier transforms [91].

2.2.4 Semi-empirical "C_6-corrections"

An empirical approach to include non-local dispersion interactions in semi-local DFT is by adding pair wise interaction between all atoms in the system. The total dispersion energy for a system of N atoms is then given by

$$E_{disp}^{tot} = \sum_{i=1}^{N}\sum_{j>i}^{N} V\left(R_{ij}\right), \tag{2.25}$$

where the pair-potential $V\left(r_{ij}\right)$ between two atoms i and j has the general form

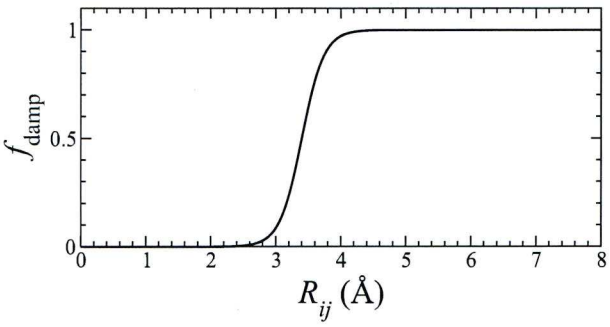

Figure 2.2: The damping function f_{damp} as function of the distance between two carbon atoms used in the Grimme correction [77]. The damping function is equal unity at large separations and zero for small separations and is used avoid divergence due to the C_6 correction for small separations.

$$V\left(r_{ij}\right) = -f_{\text{damp}}\left(R_{ij}\right)\frac{C_{6ij}}{R_{ij}^{6}}. \tag{2.26}$$

Here R_{ij} is the distance between the two atoms, C_{6ij} is the C_6 coefficient determining the strength of the interaction between the atoms and $f_{\text{damp}}\left(R_{ij}\right)$ is a damping function which has the value 1 for large separations and 0 for small separations between the two atoms. The damping function is needed to avoid divergence in the energy at small distances. There exists several methods for applying this type of correction to DFT [76–79] with different definitions of the damping function as well as the C_{6ij} coefficients, which are discussed in more detail below. Figure 2.2 shows the damping function applied in the Grimme correction [77] as a function of the distance between two carbon atoms.

The forces contributed by the C_6 correction are obtained analytically by taking the gradients of Eq. (2.26), with the force acting on atom i due to the interaction with atom j given by

$$F_i = -\boldsymbol{\nabla}_i V(R_{ij}) = C_{6,ij}\frac{\mathbf{R}_j - \mathbf{R}_i}{R_{ij}^{7}}\left[\frac{6f_{\text{damp}}(R_{ij})}{R_{ij}} - f'_{\text{damp}}(R_{ij}))\right] \tag{2.27}$$

Note that for periodic systems the atoms from periodic images have to be included in Eq. (2.25) for the total energy, and in a similar manner for the forces.

Various C_6 schemes

In this thesis four different C6-correction schemes will be discussed, namely Wu-Yang (WY) [76], Grimme [77], Ortmann-Bechstedt-Schmidt (OBS) [78] and Tkatchenko-Scheffler (TS) [79], where each scheme has given the name of their respective inventors. All schemes have in common that the dispersion energy contributed by one pair of atoms is given by Eq. (2.26) and the total energy by Eq. (2.25). However, how the C_6 coefficients and damping functions are evaluated differ for each method.

In the OBS scheme the C_6 parameters are obtained in a similar manner for unlike and like atom pairs using the original description by London [92]. In this description the coefficients are obtained from the ionisation potentials and polarisabilities of the atoms [78]. In the WY, Grimme and TS schemes the $C_{6,ij}$ coefficients for unlike atoms are obtained from those of like atoms pairs using combination rules. However, the combination rules vary between the schemes and in particular other parameters than homonuclear interaction coefficients enter these combination rules. For example in the WY scheme the effective number of electrons enters the combination rule [76] and in the TS scheme static polarisabilities of free atoms are used [79], while no parameters other than interaction coefficients enter the combination rule in the Grimme scheme [77]. Also the interaction coefficients between homonuclear atoms are obtained by different means in these three schemes. In the Grimme scheme they are obtained from the ionisation potential, dipole polarisability and an additional parameter depending on which row in the periodic table the atom can be found [77], while in the WY scheme the coefficients are calculated by least square fitting of molecular C_6 coefficients obtained experimentally.

In none of the WY, Grimme or OBS schemes are the chemical environments of the atoms accounted for, although the WY scheme has different coefficients for example, and sp, sp^2 and sp^3 carbon atoms are all treated differently. This raises the question about transferability of these schemes from one system to another. In the TS scheme one has tried to circumwent this problem by defining the interaction coefficients by relating the effective volume of an atom with the volume of the free atom, which is done through a Hirchfeld decomposition of the electron density [79]. Hence, the interaction coefficients have to be calculated on the fly for each atomic configuration and according to the authors of Ref. [79] the coefficients are determined from first principles.

However, although the C_6 coefficients are determined from first principles in the TS scheme, this is not the case for the accompanying damping function. The damping function contains two free parameters of which one was fitted to reproduce binding energies for the S22 database obtained from coupled cluster calculations by Jurecka and co-workers [93]. In other words, the damping function in fact makes the TS scheme semi-empirical. The Grimme correction has a similar damping function as the TS scheme, but without this fitting parameter. However, another parameter enters this function which according to Grimme does not affect the results [77], but is chosen to a seemingly arbitrary number. The damping function entering the OBS scheme has a different form than Grimme and TS and was designed to reproduce the interlayer spacing of graphite. A third form of damping function is found in the WY scheme, where also a seemingly arbitrary parameterisation is made. One can question how these damping functions affect the final result of a calculation, especially since each approach uses their own damping function, which supposedly work best for the particular parameterisation of C_6-coefficients.

2.3 Solutions of the Kohn-Sham equations

2.3.1 Plane wave basis set and Bloch's theorem

In density-functional theory the many-body problem of interacting electrons is simplified to a problem of non-interacting electrons experiencing an effective potential $V(\mathbf{r})$. In other words, we are searching for solutions to the one-particle time-independent Schrödinger equation:

$$\left[-\frac{1}{2}\nabla^2 + V(\mathbf{r})\right]\psi_n(\mathbf{r}) = \epsilon_n\psi_n(\mathbf{r}). \tag{2.28}$$

For a system where the nuclei are arranged in a periodic structure, for example in a crystalline solid, $V(\mathbf{r})$ is also periodic

$$V(\mathbf{r}+\mathbf{R}) = V(\mathbf{r}), \tag{2.29}$$

where $\mathbf{R}$ is a lattice vector

$$\mathbf{R} = n_1\mathbf{a}_1 + n_2\mathbf{a}_2 + n_3\mathbf{a}_3. \tag{2.30}$$

Here n_1, n_2 and n_3 are integers, and $\mathbf{a}_1$, $\mathbf{a}_2$ and $\mathbf{a}_3$ are the three unit cell vectors of the system. Our first assumption is that the system is confined into a large volume Ω which consists of N primitive unit cells with volume Ω_c, so that $\Omega = N\Omega_c$.

According to Bloch's theorem, a wave function of such a periodic system can be written as a product of a plane wave function and a periodic function, $u_\mathbf{k}(\mathbf{r})$, with the same periodicity as the potential

$$\psi_\mathbf{k}(\mathbf{r}) = \mathrm{e}^{i\mathbf{k}\cdot\mathbf{r}}u_\mathbf{k}(\mathbf{r}), \tag{2.31}$$

from which it follows that

$$\psi_\mathbf{k}(\mathbf{r}+\mathbf{R}) = \psi_\mathbf{k}(\mathbf{r})e^{i\mathbf{k}\cdot\mathbf{R}}. \tag{2.32}$$

Here, $\mathbf{k}$ is a wavevector in the first Brillouin zone and attains N discrete values due to the periodic boundary conditions over the large volume. The physical meaning of the Bloch's theorem is that the wave functions at positions $\mathbf{r}$ and $\mathbf{r}+\mathbf{R}$ are the same except for the phase factor $\exp(i\mathbf{k}\cdot\mathbf{R})$, and more importantly, the electron density has the same periodicity as the potential.

The periodic function $u(\mathbf{r})$ can be expanded in terms of plane waves

$$u_\mathbf{k}(\mathbf{r}) = \sum_\mathbf{G} c_\mathbf{k}(\mathbf{G})\mathrm{e}^{i\mathbf{G}\cdot\mathbf{r}}. \tag{2.33}$$

Due to the periodicity of $u(\mathbf{r})$ only the reciprocal lattice vectors enter the expansion, which are defined as

$$\mathbf{G} = \sum_i m_i\mathbf{b}_i, \tag{2.34}$$

where m_i are integers and $\mathbf{b}_i$ are the basis vectors of the reciprocal lattice. Note that the reciprocal lattice vectors are defined such that they fulfil $\mathbf{R} \cdot \mathbf{G} = 2\pi l$, where l is an integer. The full wave function can then be written as

$$\psi_{\mathbf{k}}(\mathbf{r}) = \sum_{\mathbf{G}} c_{\mathbf{k}}(\mathbf{G}) \mathrm{e}^{i(\mathbf{k}+\mathbf{G})\cdot\mathbf{r}}. \tag{2.35}$$

The periodic potential can also be expanded in plane waves

$$V(\mathbf{r}) = \sum_{\mathbf{G}} V(\mathbf{G}) \mathrm{e}^{i\mathbf{G}\cdot\mathbf{r}} \tag{2.36}$$

By insertion of Eq. (2.35) and (2.36) into Eq. (2.28) the following eigenvalue problem is obtained

$$\sum_{m'} H_{mm'}(\mathbf{k}) c_{\mathbf{k}}(\mathbf{G}_{m'}) = \epsilon(\mathbf{k}) c_{\mathbf{k}}(\mathbf{G}_m), \tag{2.37}$$

The original problem has been transformed to N independent equations, one for each k-point in the first Brillouin zone. The matrix elements of the Hamiltonian are given by

$$H_{mm'} = \frac{|\mathbf{k}+\mathbf{G}_m|^2}{2}\delta_{mm'} + V(\mathbf{G}_m - \mathbf{G}_{m'}), \tag{2.38}$$

By diagonalisation of the Hamiltonian a set of discrete eigenvalues $\epsilon_n(\mathbf{k})$ together with their corresponding eigenvectors $\mathbf{c}_{n,\mathbf{k}}$ are obtained, one for each $\mathbf{k}$-value. The label n for the different eigenvalues is the band index and the energy eigenvalue for the electrons in the periodic potential defines the band structure $\epsilon_n(\mathbf{k})$.

Equation 2.37 can be solved numerically when the number of plane waves is truncated. This is done by introducing a kinetic energy cut-off, often referred to as the plane wave cut-off defined as

$$\frac{|\mathbf{k}+\mathbf{G}|^2}{2} < E_{\text{cutoff}}. \tag{2.39}$$

The convergence of the solution is controlled by varying the value of the plane wave cut-off E_{cutoff}. The convergence is also controlled by the number of k-points included in the calculations. In practice only a few k-points of the first Brillouin zone are included and the actual number required for convergence of the total energy depends on both the size and the type of the system under study. Several methods exist for generating the k-points in the first Brillouin zone, the most common one being the Monkhorst-Pack scheme [94].

Plane wave basis set for non-periodic structures

The plane wave basis set requires periodic boundary conditions in all the three real-space coordinates. The method is however not restricted to study periodic structures. The periodic

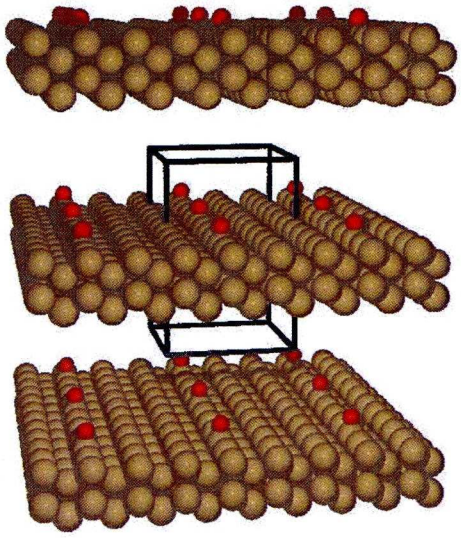

Figure 2.3: Illustration of the supercell approach for atomic oxygen adsorbed on a Cu(110) slab. The vacuum region between slabs prevent interactions between periodic images in the direction perpendicular to the surface. Furthermore, the size of the surface unit cell prevents interactions between oxygen atoms of periodic images parallel to the surface unit cell. The boundaries of the periodic supercell are indicated by black lines.

supercell can be designed so that when applying the periodic boundary conditions, the interactions between supercells in certain dimensions are made negligible by adding a vacuum region. The principle is illustrated for a single oxygen atom adsorbed on Cu(110) in Figure 2.3. The copper substrate is modelled by a slab of four copper layers perpendicular to the surface that are indefinitely repeated along the principle axes of the surface. A vacuum region is used to prevent the slab to interact with its periodic images (perpendicular to the surface). Furthermore, the surface unit cell should be chosen to be large enough to prevent interaction of the oxygen atom with its periodic images.

2.3.2 Pseudopotentials

All pseudopotential approaches are based on the frozen core approximation. In this approximation the effect of the local chemical environment on core-electrons is assumed to be weak and treated by first order perturbation theory. Therefore, the wave functions of the core-electrons are frozen and equal to those of the isolated atom. Only the valence electron wave functions are updated during the self-consistent iterations.

Due to the requirement of orthogonality, valence wave functions have rapid oscillations in the core region of the core wave functions. Outside this core region, the core wave functions are essentially zero, which results in much smoother valence wave functions in this region. To treat the rapid variation of the valence wave functions in the core region a large number

of plane waves are needed for convergence. One way of getting around this problem is the use of a pseudopotential, in which the interactions of the valence electrons with the nuclei and the core-electrons are described by an effective, much weaker potential. The resulting pseudo-wave functions are smooth inside the core region and are equal the real wave functions outside the core region. The number of plane waves required to describe the pseudo-wave functions is much less than for the real wave functions, rendering the solution of Eq. (2.37) much more feasible.

Several different pseudopotentials exist, for example orthogonalised plane wave (OPW), norm-conserving pseudopotentials (NCPP), ultra-soft pseudopotentials (USPP) and the projected augmented waves (PAW) method. The USPP and PAW methods are known to converge with a relative small number of plane waves. Since the PAW is a more general method compared to USPP, the PAW method has been used for the plane waves calculations presented in this thesis. The PAW method was originally developed by Blöchl, and for a description of how this method works see the original publication by Blöchl in Ref. [95] or the paper by Kresse and Joubert in Ref. [96].

Chapter 3

Experimental characterisation

The aim of this chapter is to give a brief introduction to the principles of the different experimental characterisation techniques behind the experimental results presented with our theoretical results in Chapter 4 and 5. It will also be discussed how the quantities measured in the different experiments can be evaluated within density functional theory as well as how the theory relates to the experimental observations.

3.1 Scanning tunnelling microscopy

Since its invension in 1981 by Gerd Binnig and Heinrich Rohrer [97], the scanning tunnelling microscope (STM) has had a great influence on surface science since it for the first time allowed scientists to study surfaces on a sub-nanometer scale in real space. In an STM a metal tip is approached very close ($\sim$10 Å) to a (semi) conducting surface and a bias voltage is applied between the tip and surface. Although the bias voltage would not classically allow the electrons to overcome the potential barrier between the tip and surface, quantum mechanics introduces a small probability of tunnelling between tip and sample. The basic principle behind the quantum tunnelling is illustrated in Figure 3.1, where a particle with mass m and energy level E tunnels through a square potential V. The energy of the particle is conserved but the amplitude of the particle's wave function is decreased. The probability for the tunnelling to occur is given approximately by

$$\mathrm{P} \propto \exp\left[-d\frac{\sqrt{2m(V-E)}}{\hbar}\right], \tag{3.1}$$

where d is the width of the barrier, E is the energy of the particle, V is the height of the potential barrier. The tunnelling probability, and the resulting tunnelling current in STM, decay exponentially with respect to the width of the potential barrier, which is related to the distance between tip and sample in the STM setup. Typically, the tunnelling probability decreases by an order of magnitude when increasing the tip-surface distance by 1 Å. Due to this exponential behaviour of the tunnelling probability it is possible to achieve spatial resolution on the atomic

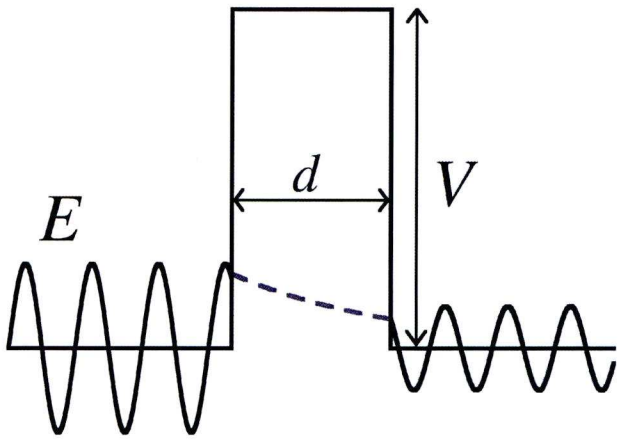

Figure 3.1: An electron with energy E tunnelling through a potential barrier $V > E$ of width d. The probability of the tunneling in given by Eq. (3.1).

scale.

In STM, electrons tunnel between electronic states of the tip and the sample. From first order perturbation theory the tunnelling current from the tip to the sample is given by Fermi's golden rule as

$$I = (2\pi e/\hbar) \sum_{\mu\nu} \{f(\epsilon_\mu)\,[1 - f(\epsilon_\nu + eV)] - f(\epsilon_\nu)\,[1 - f(\epsilon_\mu + eV)]\} \times |M_{\mu\nu}|^2\, \delta(\epsilon_\mu - \epsilon_\nu), \tag{3.2}$$

where $f(\epsilon)$ is the Fermi function, V is the applied voltage, $M_{\mu\nu}$ is the tunnelling matrix element between states ψ_μ of the probe and ψ_ν of the sample and ϵ_μ is the energy of state ψ_μ in the absence of tunnelling.

Assuming a constant density of states of the tip, the tunnelling current depends on the electronic structure of the sample as well as the distance between tip and sample. STM images with both these aspects are illustrated in Figure 3.2. The contrast difference between the tetragonal networks in Figure 3.2 (a) results from a topographic effect, since two terraces of the Cu(111) surface (with adsorbed molecular network) is imaged, while the waves on the atomically flat terrace in Figure 3.2 (b) is an electronic effect. The white protrusions in Figure 3.2 (b) are molecules which change both topography and electronic structure compared to the metal substrate, which means that molecular adsorbates are not necessarily imaged as bright protrusions [98]. An ability of STM to image the electronic structure, also makes it possible to image molecular orbitals [99] which is illustrated in Figure 3.2 (c).

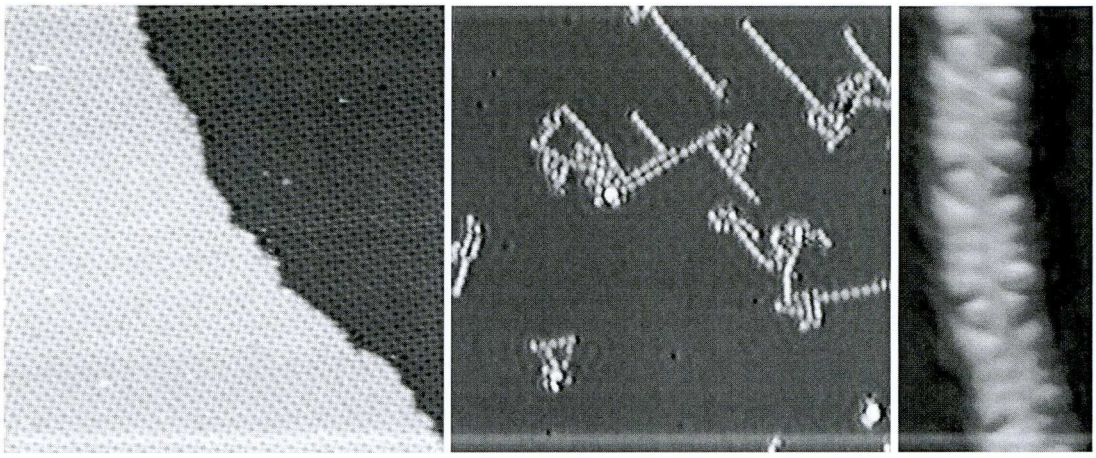

(a) (b) (c)

Figure 3.2: (a) Molecular networks on two terraces of the Cu(111) surface, wth the difference in contrast being due to topographical differences. (b) Molecular chains imaged brighter due to topographical differences, wavelike features on surface standing wave pattern due to scattering of the surface state from the chains, (c) topographical contrast (molecules imaged brighter than surface) as well as electronic contrast (imaging of a molecular orbital).

3.1.1 The Tersoff-Hamann approximation

From the Bardeen's approximation [100] of the matrix elements $M_{\mu\nu}$ in Eq. (3.2) and by assuming a spherical tip one can show that the tunnelling current is proportional to the local density of states (LDOS) of the sample

$$I(V, \vec{r}_0) \propto \int_{\epsilon_F}^{\epsilon_F + eV} d\epsilon \, \rho(\epsilon, \vec{r}_0) \tag{3.3}$$

and the first derivative of the tunnelling current is given by

$$\frac{dI}{dV}(V, \vec{r}_0) \propto \rho(\epsilon_F + eV, \vec{r}_0) = \sum_\alpha |\psi_\alpha(\vec{r}_0)|^2 \, \delta(\epsilon_F + eV - \epsilon_\alpha), \tag{3.4}$$

where $\rho(\epsilon_F + eV, \vec{r}_0)$ is the LDOS at point $\vec{r}_0$ and energy $\epsilon_F + eV$, $\psi_\alpha(\vec{r}_0)$ are the wavefunctions of the sample. This is the Tersoff-Hamann approximation [101, 102] which has been used in all STM simulations within this thesis.

In DFT the wave functions in Eq. (3.4) are given by the Kohn-Sham wave functions. In the STM simulations the wave functions have been extrapolated far away from the surface by an exponentially decaying function where the matching distance was determined at a height above the surface where the electrostatic potential becomes constant, corresponding to the vacuum region. Figure 3.3 illustrates the electrostatic potential averaged over the xy-plane along a vector perpendicular to a four layer Cu(111) slab. The matching distance is chosen at the distance above the surface where the vacuum region begins (grey area).

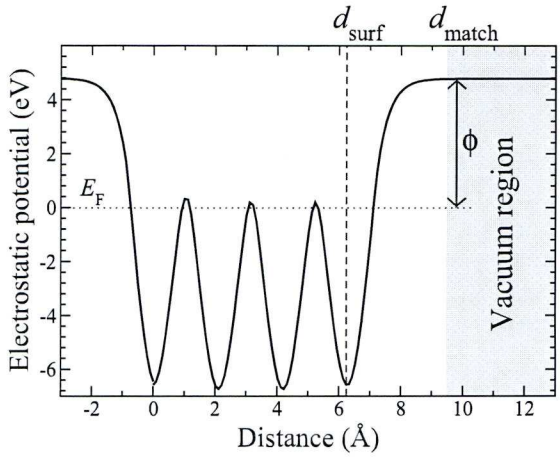

Figure 3.3: Average electrostatic potential perpendicular to a four layer Cu(111) slab illustrating the choice of matching distance from the first surface layer, defined as $d_{\mathrm{match}} - d_{\mathrm{surf}}$.

3.2 Infrared absorption spectroscopy

Infrared (IR) absorption spectroscopy probes the fundamental vibrations, or normal modes, of molecules. The vibrations can be excited by irradiating an infrared light, if the energy of the photon matches the energy of the vibration. Furthermore, the vibration must be infrared active, in other words the vibrational excitation must give rise to a dynamic dipole moment of the molecule. Hence IR spectroscopy is sensitive both to the vibrational frequencies and the dynamic dipole moments of molecules. By irradiating a molecule by infrared light of different frequencies (typical in a range 0–4000 cm^{-1}) a characteristic spectrum will be obtained which provides information about the molecule itself, but also about the interaction of the molecule with for example other molecules.

For molecules adsorbed on metal surfaces, one has to use reflection absorption infrared spectroscopy (RAIRS). In RAIRS the metal substrate is irradiated and the photons are reflected from the metal surface. A vibration in a molecule adsorbed on the surface can absorb a photon, but only if it has the same frequency as the photon and has a dynamical dipole moment perpendicular to the surface. This dipole selection rule is due to the screening by the metal substrate, illustrated in Figure 3.4: Dipole moments parallel to the surface will be cancelled out due to the screening from the metal substrate, while dipole moments perpendicular to the surface are instead enhanced.

3.2.1 The harmonic approximation

In the harmonic approximation the change of the potential energy due to a displacement of an atom away from its equilibrium position is approximated to be quadratic. Here we will show how the harmonic approximation can be used to obtain vibrational spectra first for a model system of a single atom moving in a one-dimensional harmonic potential, which will be followed by a generalisation to a molecule of N atoms in three dimensions. In the general case

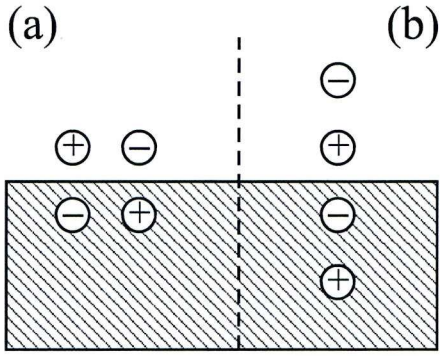

Figure 3.4: Illustration of the screening of an external dipole moment by a metal substrate. If the external dipole moment is aligned parallel to the metal surface the induced image charge will cancel out the dipole moment (a). If the external dipole is aligned perpendicular to the metal surface, the induced image charge will reinforce the dipole moment (b). Therefore, when modelling RAIRS spectrum only dipole moments that are perpendicular to the metal surface are taken into account.

it will also be shown how the infrared activities of the vibrational modes can be obtained.

Single atom in one dimension

Let us begin with deriving the eigenfrequency of an atom moving in a one dimensional potential $V(x)$. For small displacements x around the equilibrium position x_0 the potential can be expanded in a Taylor series with respect to the powers of the displacement x

$$V(x_0 + x) = V(x_0) + x \left.\frac{\mathrm{d}V}{\mathrm{d}x}\right|_{x=x_0} + x^2 \frac{1}{2} \left.\frac{\mathrm{d}^2V}{\mathrm{d}x^2}\right|_{x=x_0} + \ldots \tag{3.5}$$

At equilibrium positions the derivative of the potential equals zero. Furthermore, by making the variable substitution $x \rightarrow x - x_0$ and setting the potential to zero at equilibrium, Eq. (3.5) simplifies to

$$V(x) = x^2 \frac{1}{2} \left.\frac{\mathrm{d}^2V}{\mathrm{d}x^2}\right|_{x=0} = \frac{1}{2}kx^2, \tag{3.6}$$

where k is a force constant determined by the curvature of the harmonic potential. To find the solutions of x first consider the force acting on the atom in the harmonic potential

$$F = -\frac{\mathrm{d}V}{\mathrm{d}x} = -kx \tag{3.7}$$

combined with Newton's second law of motion

$$F = m\frac{\mathrm{d}^2x}{\mathrm{d}t^2}, \tag{3.8}$$

resulting in

$$m\frac{\mathrm{d}^2x}{\mathrm{d}t^2} = -kx, \tag{3.9}$$

where m is the mass of the atom. The general solutions for x is then given by

$$x(t) = A\sin\left(\sqrt{\frac{k}{m}}t\right) + B\cos\left(\sqrt{\frac{k}{m}}t\right) \tag{3.10}$$

Hence the atom oscillates with the frequency

$$\nu = \frac{1}{2\pi}\sqrt{k/m}. \tag{3.11}$$

By using the definition of k in Eq. (3.6) one obtains

$$\left.\frac{d^2V}{dx^2}\right|_{x=0} = -\left.\frac{dF}{dx}\right|_{x=0} = (2\pi\nu)^2 m, \tag{3.12}$$

which gives the fundamental vibration frequency ν of an atom of mass m, oscillating in a harmonic potential described by V. Hence, if the first derivative of the force acting on the particle at the equilibrium position as well as the mass of the atom are known, the fundamental frequency of the atom's motion in the potential is also known.

Molecule of N atoms in three dimensions

Equation (3.12) gives the foundation for calculations of the normal modes of a molecule within the framework of the harmonic approximation. For a molecule of N atoms, Eq. (3.12) is generalised to the eigenvalue problem [103]

$$\sum_{k=1}^{3N}\left(H_{\mathrm{jk}} - \lambda_i M_{jk}\right)X_{ki} = 0, \qquad \lambda_i = (2\pi\nu_i)^2, \tag{3.13}$$

where ν_i is the frequency of the normal mode i and X_{ki} are the elements of its eigenvector. H is the force constant matrix of the system with matrix elements

$$H_{jk} = \frac{\partial^2 V}{\partial x_j \partial x_k}, = -\frac{\partial F_j}{\partial x_k} \tag{3.14}$$

where the indices $i, j = 1, ..., 3N$ are over all atoms and the three Cartesian directions. For example, for a molecule of two atoms a and b the matrix H is given by

$$H = -\begin{pmatrix}
\frac{\mathrm{d}F_x^a}{\mathrm{d}x^a} & \frac{\mathrm{d}F_x^a}{\mathrm{d}y^a} & \frac{\mathrm{d}F_x^a}{\mathrm{d}z^a} & \frac{\mathrm{d}F_x^a}{\mathrm{d}x^b} & \frac{\mathrm{d}F_x^a}{\mathrm{d}y^b} & \frac{\mathrm{d}F_x^a}{\mathrm{d}z^b} \\
\frac{\mathrm{d}F_y^a}{\mathrm{d}x^a} & \frac{\mathrm{d}F_y^a}{\mathrm{d}y^a} & \frac{\mathrm{d}F_y^a}{\mathrm{d}z^a} & \frac{\mathrm{d}F_y^a}{\mathrm{d}x^b} & \frac{\mathrm{d}F_y^a}{\mathrm{d}y^b} & \frac{\mathrm{d}F_y^a}{\mathrm{d}z^b} \\
\frac{\mathrm{d}F_z^a}{\mathrm{d}x^a} & \frac{\mathrm{d}F_z^a}{\mathrm{d}y^a} & \frac{\mathrm{d}F_z^a}{\mathrm{d}z^a} & \frac{\mathrm{d}F_z^a}{\mathrm{d}x^b} & \frac{\mathrm{d}F_z^a}{\mathrm{d}y^b} & \frac{\mathrm{d}F_z^a}{\mathrm{d}z^b} \\
\frac{\mathrm{d}F_x^b}{\mathrm{d}x^a} & \frac{\mathrm{d}F_x^b}{\mathrm{d}y^a} & \frac{\mathrm{d}F_x^b}{\mathrm{d}z^a} & \frac{\mathrm{d}F_x^b}{\mathrm{d}x^b} & \frac{\mathrm{d}F_x^b}{\mathrm{d}y^b} & \frac{\mathrm{d}F_x^b}{\mathrm{d}z^b} \\
\frac{\mathrm{d}F_y^b}{\mathrm{d}x^a} & \frac{\mathrm{d}F_y^b}{\mathrm{d}y^a} & \frac{\mathrm{d}F_y^b}{\mathrm{d}z^a} & \frac{\mathrm{d}F_y^b}{\mathrm{d}x^b} & \frac{\mathrm{d}F_y^b}{\mathrm{d}y^b} & \frac{\mathrm{d}F_y^b}{\mathrm{d}z^b} \\
\frac{\mathrm{d}F_z^b}{\mathrm{d}x^a} & \frac{\mathrm{d}F_z^b}{\mathrm{d}y^a} & \frac{\mathrm{d}F_z^b}{\mathrm{d}z^a} & \frac{\mathrm{d}F_z^b}{\mathrm{d}x^b} & \frac{\mathrm{d}F_z^b}{\mathrm{d}y^b} & \frac{\mathrm{d}F_z^b}{\mathrm{d}z^b}
\end{pmatrix} \tag{3.15}$$

where for example $\mathrm{d}F_z^b/\mathrm{d}x^a$ is the derivative of the force of atom b in the y-direction with respect to displacement of atom a in the x-direction (from the equilibrium configuration of the system). The elements of the diagonal matrix M in Eq. (3.13) are given by

$$M_{kl} = \delta_{kl} m_n, \qquad k = 3n-2,\ 3n-1,\ 3n, \tag{3.16}$$

where m_n is the mass of the nth atom.

Finally, the infrared intensity of a normal mode i is given by the derivative of the electrostatic dipole moment with respect to a displacement of the atoms in the directions of the eigenvector i:

$$I_{\mathrm{i,abs}} = \left| \frac{d\boldsymbol{\mu}}{dQ_{\mathrm{i}}} \right|^2 \tag{3.17}$$

where $I_{\mathrm{i,abs}}$ is the absolute infrared intensity, Q_{i} is referred to as a normal mode coordinate of eigenvector X_i. The derivative with respect to Q_{i} can be calculated as as a sum over the derivatives of the dipole moment with respect to the Cartesian atomic coordinates x_k

$$\frac{d\boldsymbol{\mu}}{dQ_{\mathrm{i}}} = \sum_{k=1}^{3N} \frac{\partial \boldsymbol{\mu}}{\partial x_k} X_{ki}. \tag{3.18}$$

Computational approach

The derivatives of the forces in the force constant matrix, as well as the derivatives of the dipole moment are calculated using central finite differences. We can illustrate how central differences work by considering a function $f(x)$ for which we want to calculate the derivative at the point x_0

$$\left. \frac{\mathrm{d}f}{\mathrm{d}x} \right|_{x=x_0} = \frac{f(x_0 + \Delta x) - f(x_0 - \Delta x)}{2\Delta x} + O(\Delta x^2), \tag{3.19}$$

where Δx is the finite displacement of an atom. Hence to obtain the derivative using central differences two calculations are needed. The error of this approximation is proportional to the square of the spacing Δx, which is an improvement over forward and backward differences where the error is linearly dependent on the spacing Δx.

For each DFT calculation the forces on all atoms are calculated, this means that to setup the force constant matrix using central differences for a system of N molecules, $6N$ calculations are required, two calculations per atom and Cartesian coordinate. For each DFT calculation also the electric dipole moment of the system is calculated, which is used to determine the infrared intensity for each normal mode, using Eq. (3.17) to calculate the derivative of the dipole moment with respect to the eigenvectors and Eq. (3.16) to calculate the infrared intensity. Note that for calculations of RAIR spectra only the dipole moment perpendicular to the substrate has to be considered (see Section 3.2).

A module for calculating infrared spectra was implemented into the Atomic Simulation Environment [104] which is available for download for free at *https://wiki.fysik.dtu.dk/ase/* under the GNU Lesser General Public License.

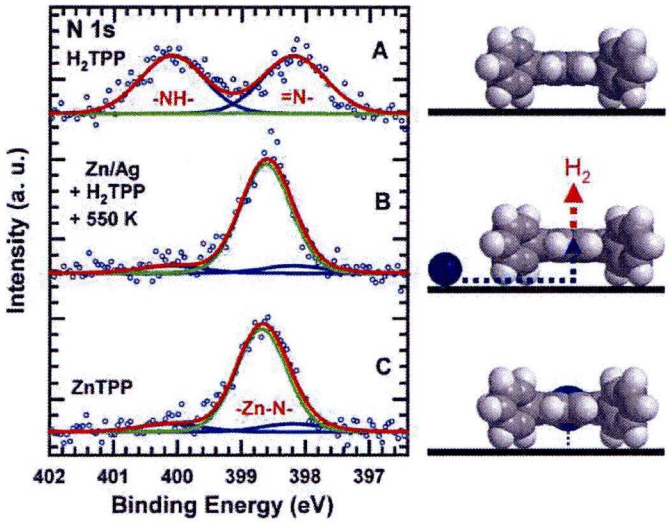

Figure 3.5: N1s spectra from XPS experiments of (A) a free-based tetraphenylporphyrin (H_2TPP) on Ag(111) and (B) after deposition of Zn atoms in which the porhyrins dehydrogenate and picks up the Zn atoms to form ZnTAPP. (C) N1s spectra of a directly deposited monolayer of ZnTAPP on Ag(111) for comparison. [20] - Reproduced by permission of The Royal Society of Chemistry.

3.3 X-ray photoelectron spectroscopy

X-ray photoelectron spectroscopy (XPS) experiments measure the energy cost to remove core-electrons from atoms. Since the core levels are very sensitive to the local electrostatic potential, XPS can be used to determine the local chemical environments an atom experiences in a molecule. Figure 3.5 shows the XPS spectra of the nitrogen 1s (N1s) core levels of the free-based tetraphenylporphyrin molecule (H_2TPP) adsorbed on the Ag(111) surface from Kretschmann and co-workers [20]. The nitrogen atoms in the molecule exhibit two different chemical environments, one with and one without attached hydrogen atoms, which results in two peaks in the spectrum (A). After deposition of Zn atoms on the surface, the molecule dehydrogenates and picks up a Zn atom to form the ZnTPP species. This results in a symmetrisation of the nitrogen atoms, hence only one peak is observed in the spectrum (B). In (C) the N1s spectrum of a directly deposited monolayer of ZnTPP on Ag(111) is shown for comparison.

This section will describe how core-hole binding energies can be calculated using DFT and how the results are related to experiments. For more details see for example the book by Hüfner [105].

Figure 3.6 illustrates the basic principles behind the XPS technique: X-ray radiation with energy $h\nu$ per photon core-ionises an atom. For a metallic system, the kinetic energy E_k of the emitted electron is measured and the core level binding energy E_b (relative to the Fermi level) is given by

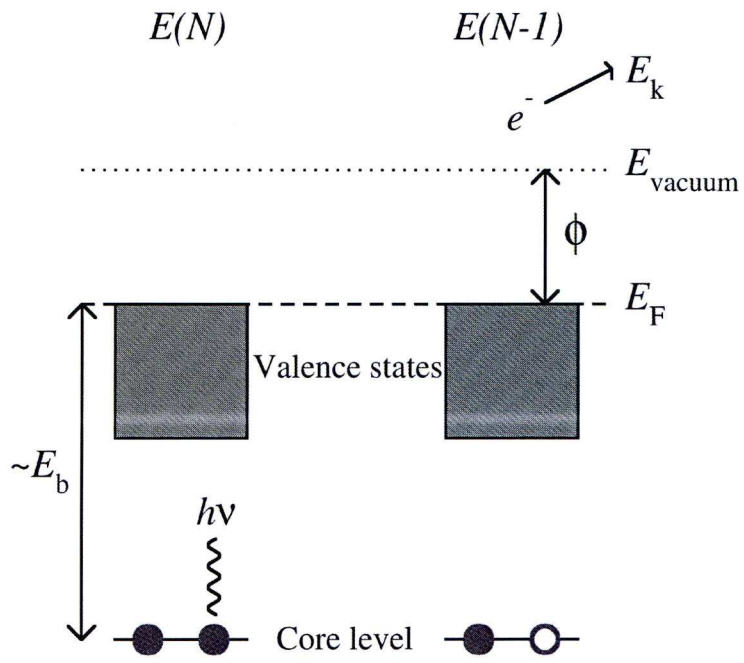

Figure 3.6: Sketch illustrating the principle of the XPS technique. A photon with energy $h\nu$ core-ionises an atom and generates a photoelectron.

$$E_{\mathrm{b}} = h\nu - E_{\mathrm{k}} - \phi = E(N-1) - E(N), \tag{3.20}$$

where $E(N)$ is the total energy of the neutral system, $E(N-1)$ is the total energy of the core-ionised system, and ϕ is the work function. The work function is experimentally determined as the smallest energy required to generate a photoelectron, in other words the energy required to excite an electron at the Fermi level to the vacuum level. It is important to note that the relation between the measured core level binding energy and the energy of the occupied core level is only approximate. In reality the measured core level binding energy is related to the total energies of a state with N electrons $E(N)$ and the one with $N-1$ electrons $E(N-1)$ [105].

3.3.1 Chemical shifts from density-functional theory

According to Eq. (3.20), the core level binding energy of an atom in a molecule can in principle be determined if the total energies of the core-ionised and neutral molecule is known. However, in practice the absolute core level binding energies are not what we will calculate, but rather the core level (chemical) shifts E_{CLS} of an element in a system a with respect to system b

$$E_{\mathrm{CLS}} = [E^{\mathrm{a}}(N-1) - E^{\mathrm{a}}(N)] - \left[E^{\mathrm{b}}(N-1) - E^{\mathrm{b}}(N)\right], \tag{3.21}$$

where $E^{\mathrm{a}}(N)$ is the total energy of the neutral system a and $E^{\mathrm{a}}(N-1)$ is the total energy of system a without an electron on a core level, and similar for system b.

The total energies of the neutral systems are obtained from DFT calculations. The core-ionised system will be treated within the frozen core approximation [106]. In this approximation the core-hole is assumed to stay entirely localised at the excited atom. For molecular adsorbates on metals this is a valid approach since the metal substrate acts as an electron reservoir, and the effect on the total energy when adding or removing an electron from the system is negligible. Within this approximation we will discuss two possible ways of treating the core-ionised atom, namely through the *Z+1 approximation* or a *core-ionised PAW potential.*

Z+1 approximation

In the *Z+1 approximation* [107] the effect of removing a core-electron is approximated by adding a proton to the core of the atom under consideration. In other words, the core-ionised atom with atomic number Z is replaced by a valence-ionised atom with atomic number $Z+1$. In practise a neutral atom with atomic number $Z+1$ is used since we are working on metallic substrates.

Core-ionised PAW potential

A more sophisticated method to the *Z+1 approximation* is to use a specially designed core-ionised potential to describe the core-ionised atom [106]. The principle is the same as for the *Z+1 approximation*, but the core-hole is better described this way, and hence this method gives more accurate results for chemical shifts.

3.4 X-ray standing wave absorption

X-ray standing wave (XSW) absorption experiments can be used both to determine the height, and in principle, also lateral position of molecular adsorbates above a surface. In this thesis, only XSW measurements of adsorption height will be presented. With this technique, it is possible not only to determine the height of an adsorbate but the individual heights of the different chemical species making up the adsorbate. It is important to notice that XSW is a laterally averaging technique, hence a reasonable coverage of the surface is necessary and it is not possible to determine the height of a single molecule.

The aim of this section is to give a brief introduction of the basic principles of XSW. For a more detailed description of the technique see for example the reviews by J. Zegenhagen [108] and D. P. Woodruff [109].

The basic principle of XSW is illustrated in Figure 3.7. By irradiating a single crystal by X-ray photons whose energy fulfils the Bragg condition, the superposition of the incident and reflected wave results in a standing wave field. If an atom of chemical species A of the adsorbate is located in one of the anti-nodes of the standing wave field it will be core-ionised and emit a photoelectron. If instead the atom is located in one of the nodes of the standing wave field the atom would not be core-ionised, and the intensity of emitted photoelectrons is

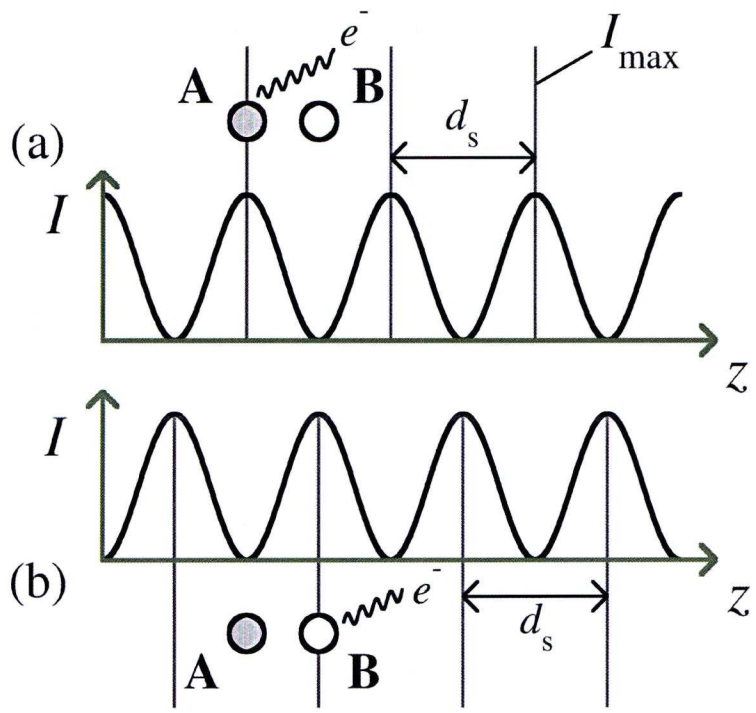

Figure 3.7: Sketch illustrating the basic principle of the XSW technique. Maximum intensity of photoelectrons is observed if the maxima of the intensity I_{max} of the standing wave field coincide with the atomic positions. The maxima are adjusted by tuning the phase between the incident and reflected beam. (a) The intensity maxima of the standing wave field coincide with atom A, and consequently the intensity of photoelectrons emitted from atom A will be at a maximum. (b) The intensity maxima of the standing wave field coincide with atom B, and consequently the intensity of photoelectrons emitted from atom B will be at a maximum.

therefore zero. By tuning the incident phonon energy in a small range around the Bragg energy (typically about ± 2 eV) the phase difference between incident and reflected beam can be tuned, which means that the position of the nodes and antinodes of the standing wave field will move. By recording the intensity of the emitted electrons as a function of the incident photon energy one will obtain a unique function for each adsorbate height (modulus the distance between the Bragg planes). These functions are determined experimentally and the heights of different atoms above a surface are calculated from their profiles.

The intensity profiles are determined indirectly by measuring the numbers of photoelectrons emitted by the adsorbate in an X-ray photoelectron spectroscopy (XPS) setup. This makes it possible to determine the height of each chemical species of the adsorbate (and even diffentiate between atoms of identical chemical species) as the energy of the emitted photoelectron is dependent on the core-level binding energy (as in XPS). It is important to notice that the heights of the adsorbates are determined modulus the distance between Bragg planes.

For the experimental results presented in this thesis the normal incidence XSW (NIXSW) was performed on a Cu(111) surface in which the X-ray beam was perpendicular to the Bragg

planes. The Bragg distance between the Bragg planes is then equal to the interplanar spacing perpendicular to the surface of the substrate. The height from NIXSW, h_{XSW} is then given by

$$h_{\mathrm{XSW}} = h_{\mathrm{ads-Cu}} \,(\mathrm{mod}\, d_{<111>}), \tag{3.22}$$

where $h_{\mathrm{ads-Cu}}$ is the height of the adsorbate above the first Cu(111) bulk layer and $d_{<111>}$ is the interlayer spacing in the $< 111 >$ direction. $h_{\mathrm{ads-surface}}$ can be approximated as the height above the outermost surface layer since relaxations of the surface layers are small. For the Cu(111) surface the relaxation of the first surface layers is less than 2 % (inwards) with respect to $d_{<111>}$ [1], so for simplicity $h_{\mathrm{ads-surface}}$ has been interpreted as the height above the first Cu layer.

[1]This value was obtained from a fully converged calculation of a four layered Cu(111) slab where the two outermost layers relaxed.

Chapter 4

Surface structures of perylene derivatives on Cu(111)

In this chapter various structures formed through self-assembly of either of the two perylene derivatives 1,3,8,10-tetraazaperopyrene (TAPP) or 4,9-diaminoperylene-quinone-3,10-diimine (DPDI) molecules on the Cu(111) surface will be discussed and compared. The main focus will be on the porous surface networks, but other structures will also be investigated.

The TAPP molecule self-assembles into two-dimensional as well as one-dimensional structures on the Cu(111) surface. Figure 4.1 depicts images from STM experiments showing different structures adapted by TAPP molecules at different annealing temperatures under UHV conditions: A close-packed network (a) was observed at temperatures of -70 °C in very small patches After annealing to around 150 °C a long-range ordered tetragonal porous network (b) was found. The long range-order in the porous network was destroyed around 190 °C, and after further annealing to 250 °C, one-dimensional chains (c) were formed.

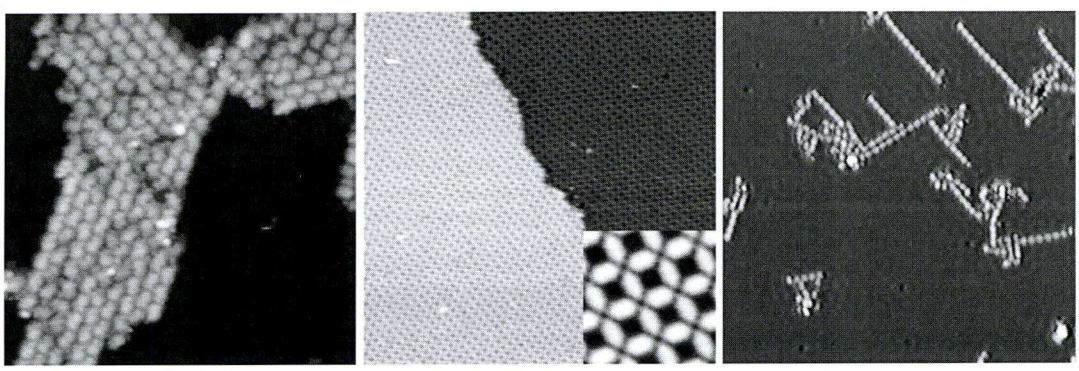

(a) (b) (c)

Figure 4.1: STM images from UHV experiments of the TAPP molecule adsorbed on the Cu(111) surface. (a) At around -70°C the molecules self-assemble into small patches of a close-packed network (1.5 V, 12 pA, 20×20 nm^2), (b) after annealing at around 150 °C a long-range ordered tetragonal porous structure is formed (1.4 V, 20 pA, 70×70 nm^2), and (c) finally at 250°C the TAPP molecules polymerise to form 1-D covalently linked chains (0.1 V, 20 pA, 50×50 nm^2). The inset in (b) shows a close-up of the porous network (1.4 V, 20 pA, 5.3×5.3 nm^2).

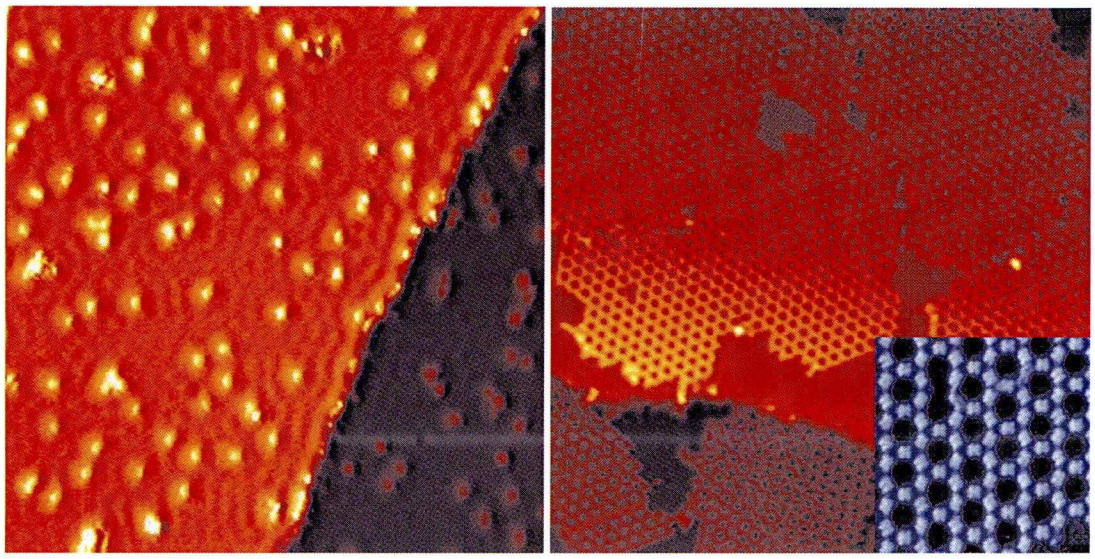

(a) (b)

Figure 4.2: STM images from UHV experiments of the DPDI molecule adsorbed on the Cu(111) surface. Before annealing a mobile phase is observed in which the molecules are isolated from each other on the surface. The image in (a) shows a snapshot of this mobile phase at 5 K, at this temperature the mobility of the molecules is frozen (0.1 V, 50 pA, 50×50 nm^2). (b) After annealing of the sample around 200 °C the molecules organise in a honeycomb structure, (-2 V, 30 pA, 100×100 nm^2). The inset in (b) shows a high resolution image (-1.4 V, 25 pA, 15×15 nm^2), exhibiting the honeycomb network in detail and showing a defect.

DPDI molecules are able to self-assemble into several different structures on the Cu(111) surface, depending on the surface coverage of molecules and the annealing temperature [62]. For coverages below 0.7 ML ordered and disordered phases have been observed in STM experiments at different temperatures: In the disordered phase the molecules are very mobile on the surface at room temperature, and we refer to this phase as the mobile phase. At 5 K the translational motions of the molecules are frozen, and it is possible to image individual molecules in STM, furthermore they are found to be isolated from each other on the surface, Figure 4.2 (a). After annealing of the mobile phase to around 200 °C the molecules self-assemble into a hexagonal porous network, Figure 4.2 (b). This honeycomb network has an extraordinary structural stability, which is reflected in its inertness towards manipulations of monomers in the network with the STM tip. Furthermore LEED studies show that the long-range order of the network persists up to temperatures of 450 °C [62].

We will start to discuss the structures and stability of the two porous surface networks formed either by the TAPP or DPDI molecules, illustrated in Figure 4.1 (b) and 4.2 (b), respectively. Furthermore, it will also be shown how the adatoms, which were found to coordinate to the molecules in the two networks, can be identified by an STM fingerprint of the adatom-ligand coordination. Moreover, the chemical bonding of the covalently linked chains of TAPP molecules will be discussed. The chapter ends with a section on what influence non-local dispersion interactions have on the different structures.

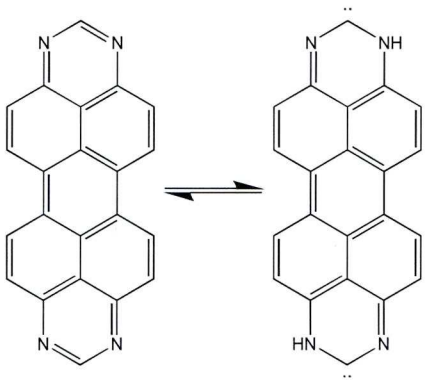

TAPP taut-TAPP

Figure 4.3: Schematics of the TAPP tautomers.

The details of the experimental work of TAPP is given in Chapter 5 of the PhD thesis by Manfred Matena [110]. This thesis also contains the experiments on the porous DPDI network, which was a continuation of the PhD project by Marcus Wahl [111] on this system. My theoretical work was done in close collaboration with Prof. Thomas Jung's group at the University of Basel and Meike Stöhr's group at Zernike institute of advanced materials, who performed all the UHV experiments presented in this chapter, and with Prof. Lutz Gade's group at the University of Heidelberg, who synthesised the TAPP and DPDI molecules.

4.1 Molecular building blocks

4.1.1 1,3,8,10-tetraazaperopyrene (TAPP)

1,3,8,10-tetraazaperopyrene (TAPP) [112] with the chemical formula $C_{22}H_{10}N_4$ is a perylene derivative featuring two pyrimidine end groups, Figure 4.3. The possible chemistry of the molecule happens around the four nitrogen atoms: They can function as hydrogen bond donors, but also coordinate to metal atoms due to the four lone-pair orbitals associated with the four nitrogen atoms. There is also a possibility of a tautomerisation of the molecule, in which the hydrogen in the CH-group separating two nitrogen atoms hops to one of the adjacent nitrogen atoms, illustrated in Figure 4.3.

4.1.2 4,9-diaminoperylene-quinone-3,10-diimine (DPDI)

The chemistry of the 4,9-diamino-quinone-3,10-diimine molecule (DPDI) [113, 114] with the chemical formula $C_{20}H_{14}N_4$ is more complex than the TAPP molecule because of the many possible transformations the molecule can undergo. For example the molecule can dehydrogenate, forming one of two possible forms of dehydrogenated DPDI (dehydro-DPDI): On the one hand the amine group can lose the hydrogen atom not involved in the intramolecular hydrogen bond, resulting in a dehydro-DPDI with only imine groups (dehydro-DPDI-imine). On the other hand it is possible to form a covalent bond between the two nitrogen atoms, resulting

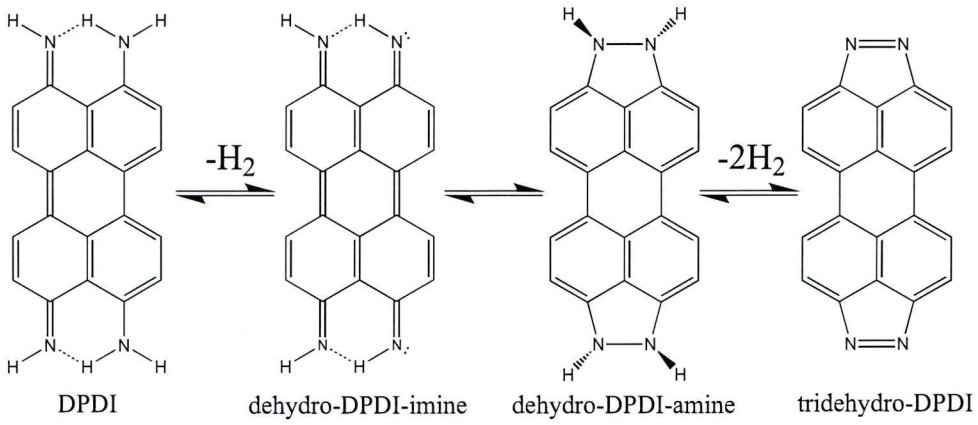

Figure 4.4: Schematics of DPDI and three of its derivatives formed by dehydrogenation: dehydro-DPDI-imine, the trans form of dehydro-DPDI-amine and tridehydro-DPDI.

in a dehydro-DPDI with only secondary amines (dehydro-DPDI-amine), which in turn can take either cis or a trans form depending on the direction in which the amine hydrogen atoms point. In vacuum the trans and cis forms of dehydro-DPDI-amine were shown from our calculations to be 1.12 eV and 0.71 eV more stable than dehydro-DPDI-imine, respectively.

Furthermore, by splitting off all the H-atoms from the N-atoms of dehydro-DPDI-amine a molecule with a double bond between two nitrogen atoms is formed (tridehydro-DPDI). Further transformations of the DPDI molecule by removing (or adding) H-atoms to the nitrogen atoms are probable, however, these are not of interest for the structures formed by DPDI molecules on Cu(111).

4.2 Structure and stability of porous surface networks

In this section we will show how the structures of the porous networks formed by deposition of either TAPP or DPDI on the Cu(111) surface were determined from combined theoretical and experimental studies. Furthermore, the underlying mechanism making the DPDI network considerably more stable than the TAPP network will be discussed.

The results presented here were achieved from GGA-DFT calculations; hence non-local dispersion forces were neglected. How these interactions affect the geometric structure as well as electronic structure of the coordination networks will be discussed in Section 4.5.2. More details of the calculations are given in Appendix A.1.

4.2.1 Structure of the tetragonal TAPP network

Experimental background

The porous network of TAPP on Cu(111) is formed through self-assembly either after annealing of a pre-formed close-packed phase to 150 °C, or by direct deposition of the molecules on the surface at 150 °C. The network is stable up to about 190 °C [49]. Above this temper-

ature the long-range order is lost, and after annealing of the sample to around 250 °C oligo- and polymeric chains are formed [49], which will be discussed in Section 4.4. A large domain of the self-assembled porous TAPP network is shown in the experimental STM image in Figure 4.1 (b).

Low-energy electron diffraction (LEED) experiments have established that the TAPP network is commensurate with the underlying Cu(111) substrate with a unit cell given by

$$\begin{pmatrix} 8 & 5 \\ -1 & 6 \end{pmatrix} \begin{pmatrix} \vec{a}_1 \\ \vec{a}_2 \end{pmatrix}, \tag{4.1}$$

where $\vec{a}_1$ and $\vec{a}_2$ are the primitive surface unit cell vectors of Cu(111). The unit cell has the dimensions 17.9 × 16.8 Å^2 and an almost orthorombic shape, with an angle of 89.4° spanned by the two unit cell vectors. Note that each unit cell contains two molecules.

Furthermore, X-ray standing wave (XSW) experiments have been performed, showing that the average heights of the nitrogen and carbon atoms above the Cu(111) surface are 2.89 Å and 2.81 Å, respectively. The combined vdW radius of copper (1.40 Å) and nitrogen (1.55 Å) is 2.95 Å. Comparing the height of the nitrogen atoms from the XSW experiments with the vdW radii it is possible to exclude a direct chemisorption of TAPP to the Cu surface since the molecule is adsorbed too far away from the surface for this to occur. The LEED results, on the other hand, indicate a strong chemical interaction between the molecules and the substrate, since the molecular overlayer is commensurate with the Cu substrate. Instead it was suggested from the experimental XSW and LEED data that the molecules are coordinated to Cu adatoms. This finding is corroborated by our theoretical DFT study.

DFT investigations

On the basis of the measured unit cell in Eq. (4.1) two different structures were investigated for the porous network; one with and one without adatoms. In the absence of adatoms, Figure 4.5 (b), the network was found to be stabilised by weak C-H...N hydrogen bonds between adjacent molecules which is made possible by a slight rotation of the molecules. The adsorption energy of this structure was found to be -0.33 eV molecule^{-1}, defined as

$$E_{\text{ads}} = \frac{1}{2}\left[E_{\text{TAPP/Cu(111)}} - \left(2E_{\text{TAPP}} + E_{\text{Cu(111)}}\right)\right], \tag{4.2}$$

where $E_{\text{TAPP/Cu(111}}$ is the total energy of the TAPP network on Cu(111), E_{TAPP} is the total energy of an isolated TAPP molecule, and $E_{\text{Cu(111)}}$ is the total energy of the isolated Cu(111) surface. Negative adsorption energy indicates a stabilisation with respect to the reference structures.

An adatom supported network (Cu-TAPP), Figure 4.5 (a), was found to be significantly more stable than the hydrogen-bonded network, with an adsorption energy of -2.40 eV molecule^{-1}, calculated using Eq. (4.2) with $E_{\text{Cu(111)}}$ redefined as the total energy of the bare Cu(111) surface with adatoms adsorbed in the closest hollow site in the structure shown in Figure 4.5 (a).

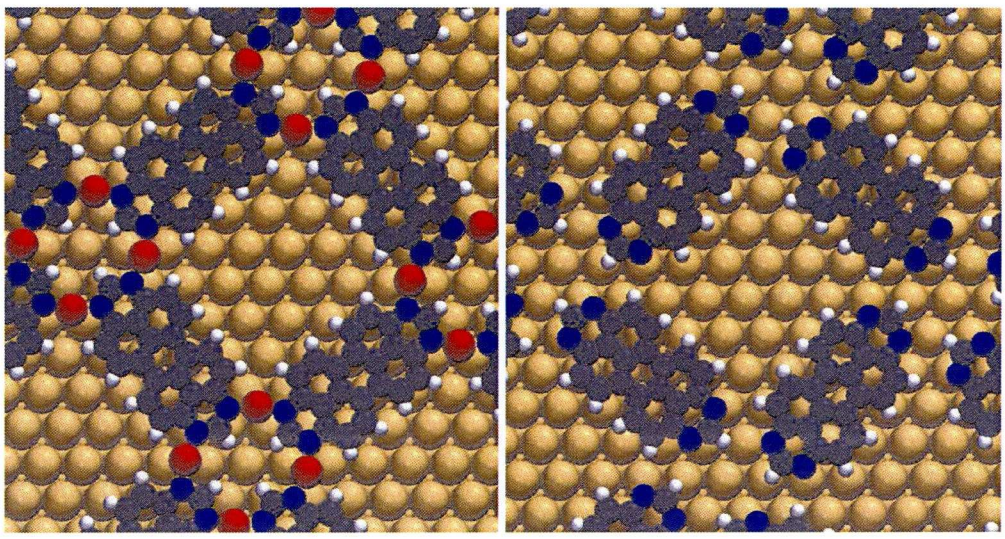

(a) (b)

Figure 4.5: Minimum energy structures of the porous network of TAPP on Cu(111) (a) with and (b) without Cu adatoms. The adatoms are illustrated as red balls. The calculations show that the adatom-coordinated structure (a) is energetically favourable.

In the Cu-TAPP network each Cu adatom is coordinated to two nitrogen atoms of adjacent molecules, resulting in a ratio of two Cu adatoms per TAPP molecule. The average N–Cu distance was found to be 2.06 Å, hence a N–Cu–N distance of 4.12 Å. Because of the different symmetry of the TAPP–Cu overlayer and the Cu(111) substrate and the preference of the Cu adatoms to adsorb on hollow sites, the bond lengths of the different N–Cu bonds in a supercell differ slightly. Further support for the adatom-supported Cu-TAPP network was found in bias dependent STM images, and will be discussed in Section 4.3.

4.2.2 Structure of the DPDI honeycomb network

Experimental background

Figure 4.2 (b) illustrates the honeycomb network which is formed from DPDI molecules on the Cu(111) after annealing to around 200 °C. The network exhibits an extraordinary stability, as is reflected by its inertness towards manipulation of single DPDI molecules with the STM tip, as well as the long-range order of the network persisting to above 450 °C [62].

LEED experiments have shown that also the DPDI network is commensurate with the Cu(111) substrate with a p(10 × 10) unit cell containing three molecules [62]. Furthermore, X-ray photoelectron spectroscopy (XPS) has shown [111] that all nitrogen atoms exhibit the same chemical environment. In contrast, the two peaks observed in XPS experiments for the mobile phase (Figure 4.2) are due to the different core-level binding energies of the amine and imine nitrogen atoms. Since only a single peak is observed in the XPS experiments for the honeycomb network, a symmetrisation of the nitrogen atoms occurs in the formation of the network. In Table 4.1 the N1s chemical shifts from XPS as well as the heights of the nitrogen

atoms above the Cu surface from XSW experiments are summarised.

Table 4.1: Observed N1s chemical shifts and distances of the two nitrogen atoms to the first surface layer, given by XPS and XSW experiments, for the mobile phase and the honeycomb network of DPDI on Cu(111). The chemical shifts are given with reference to the low-energy N1s peak of the mobile phase.

		Mobile phase		Honeycomb network
Relative chemical shift (eV)	N-atoms	0	1.82	1.50
Distance to surface (Å)	N-atoms	2.20	2.42	2.83
	C-atoms	2.68		3.00

The commensurability of the DPDI based network with respect to the Cu(111) substrate and the stability of the network, suggest a strong molecule-substrate interaction. However, the observed heights of the N and C atoms above the surface from XSW experiments are 2.83 Å and 3.00 Å respectively. Considering that the combined vdW radius of nitrogen and copper is 2.95 Å a direct chemisorption of the molecules in the honeycomb network to the copper substrate does not seem likely. Instead, in a similar manner as for the tetragonal TAPP network, the honeycomb network of DPDI molecules is suggested to be stabilised by Cu adatoms. Furthermore, as mentioned in the previous paragraph, the honeycomb network exhibits only one type of nitrogen atom indicating a symmetrisation of the nitrogen atoms during the formation of the honeycomb network, through a thermally activated dehydrogenation of the molecule into one of three possible derivatives: dehydro-DPDI-imine, dehydro-DPDI-amine, or tridehydro-DPDI, shown in Figure 4.4.

DFT investigation

The DFT investigation was done first of all with the experimental LEED and XSW data in mind. Hence, the p(10×10) unit cell was assumed and in all models (except one) the molecules coordinate to copper adatoms. The calculations took into account the possible transformations the molecule can undergo through dehydrogenation. Thus all four derivatives of DPDI illustrated in Figure 4.4 (including the intact molecule) were considered as possible building blocks in the honeycomb network.

Figure 4.6 shows the most stable configurations with intact DPDI molecules found with either three (a) or six (b) Cu adatoms per crossing of three intact DPDI molecules. These structures are stabilised due to the interaction between the molecules and adatoms, as well as the interaction between adatoms. It is important to notice that it was not possible to find a structure for the intact DPDI molecule where two adjacent molecules share an adatom. Hence the formation of the honeycomb network does in this case rely on a molecule-molecule interaction mediated through two Cu adatoms, which seems unlikely.

In the first report [62] of the DPDI honeycomb network it was suggested that the DPDI molecule dehydrogenates to form the dehydro-DPDI-imine species, and that the network is stabilised by hydrogen bonding between adjacent molecules. The resulting network assuming

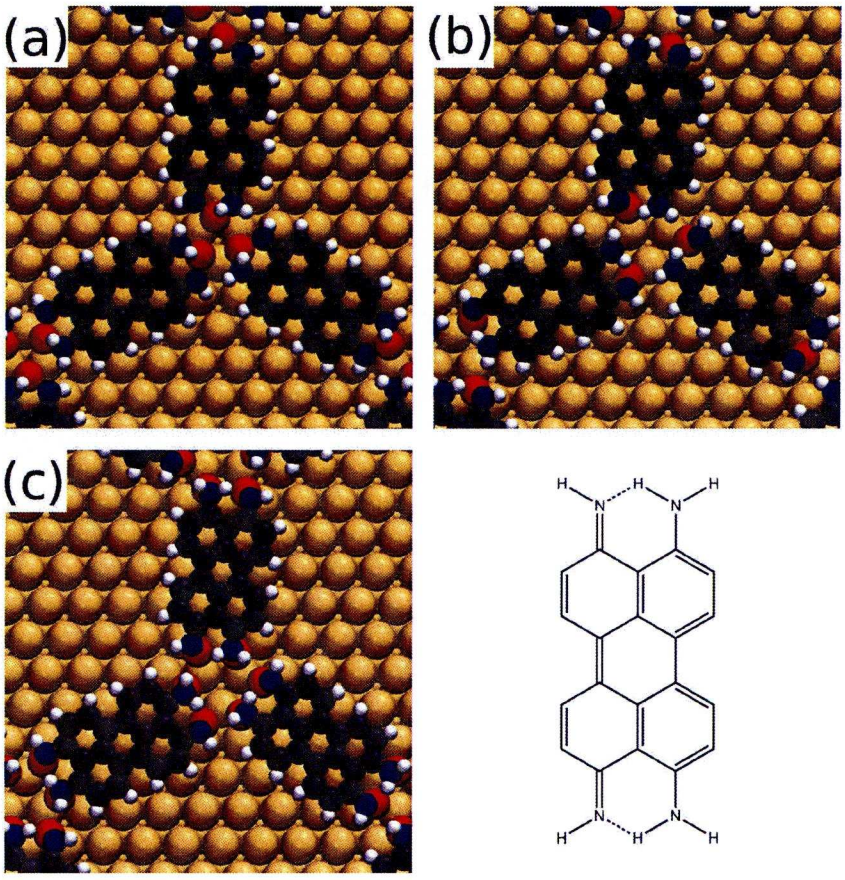

Figure 4.6: Most stable structures of honeycomb networks investigated on the Cu(111) using the intact DPDI molecule as molecular building block with (a,b) three Cu adatoms (c) six Cu adatoms per crossing between three molecules. The adatoms are illustrated as red balls.

a hydrogen bonded network as initial structure is shown in Figure 4.7 (a), and the simulations show that each individual dehydro-DPDI-imine molecule rather bonds directly to the copper substrate than forming a hydrogen bonded network. In fact the distance, 2.85Å, between a hydrogen and nitrogen acceptor atom is larger than a typical hydrogen bond distance. Therefore, the possibility of a strongly hydrogen bonded network can be excluded. It was also investigated whether dehydro-DPDI-imine can be used to form a honeycomb network through coordination to Cu adatoms. The most stable structure is illustrated in Figure 4.7 (b) with three adatoms per crossing of three molecules. In this structure each adatom is shared between nitrogen atoms of adjacent molecules, similar to the Cu-TAPP coordination network.

Figure 4.8 illustrates the most stable structures found using the dehydro-DPDI-amine molecule as building blocks for the network using either three (a) or six (b) Cu adatoms per crossing between three molecules. Note that to ensure as strong interaction of the nitrogen atoms with the adatoms we only considered the form of the molecule where the NH hydrogen atoms point in the same direction (away from the substrate). Similarly to the intact DPDI molecules, the dehydro-DPDI-amine molecules do not like sharing a Cu adatom between them, and the networks using these molecules as building blocks are dependent on a molecule-molecule inter-

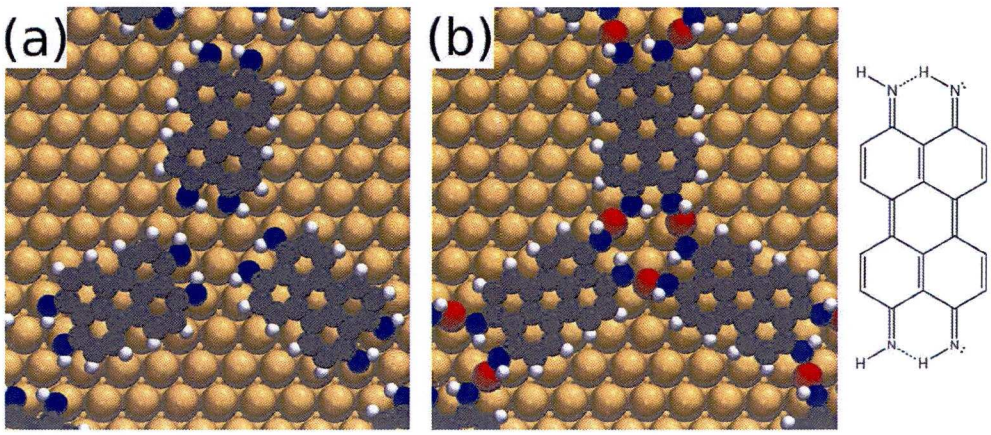

Figure 4.7: Most stable structures of investigated honeycomb networks on the Cu(111) using the dehydro-DPDI-imine as molecular building block with (a) no Cu adatoms and (b) three Cu adatoms per crossing between three molecules. The adatoms are illustrated as red balls.

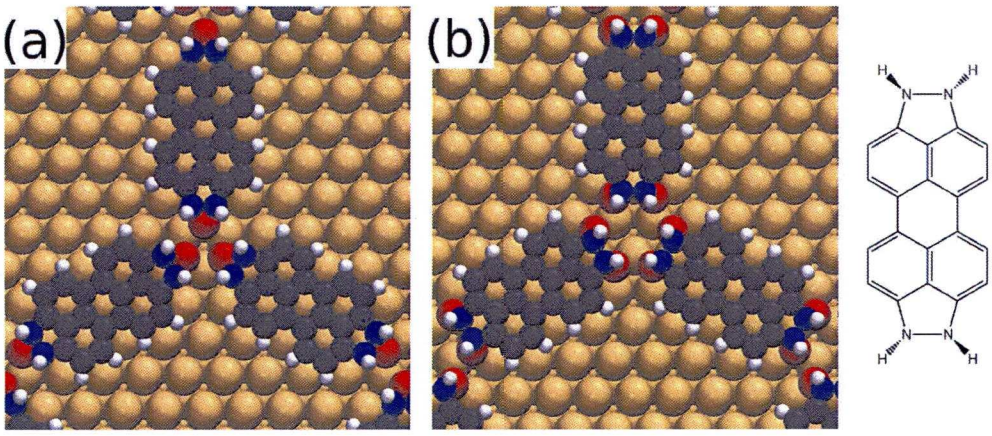

Figure 4.8: Most stable structures of investigated honeycomb networks on the Cu(111) using the dehydro-DPDI-amine as molecular building block with (a) three Cu adatoms and (b) six Cu adatoms per crossing between three molecules. The adatoms are illustrated as red balls.

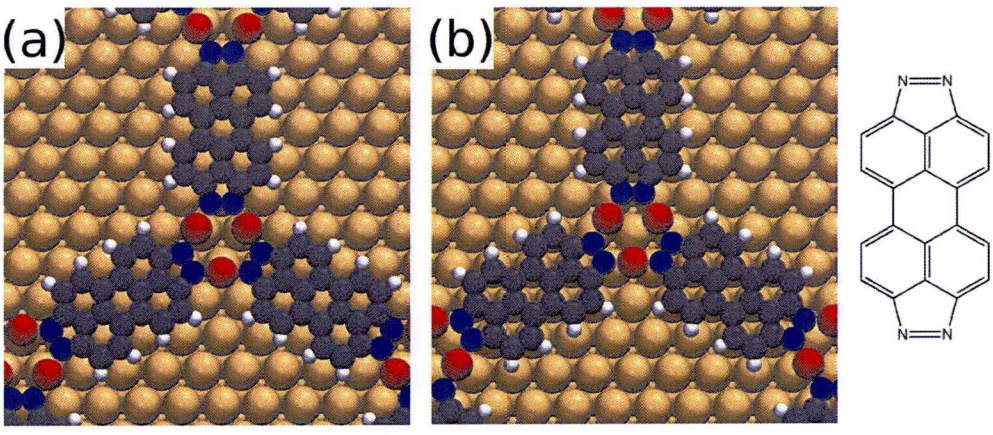

Figure 4.9: Most stable structures of honeycomb networks investigated on the Cu(111) using the tridehydro-DPDI as molecular building block with three Cu adatoms per crossing between three molecules. The adatoms are illustrated as red balls.

action mediated by two Cu adatoms.

Finally, honeycomb networks were investigated using the DPDI molecule with completely dehydrogenated nitrogen atoms, namely tridehydro-DPDI, as molecular building block. Figure 4.9 illustrates two networks with three Cu adatoms per crossing between three molecules. These two networks are identical, except for the lateral position of adatoms and molecules with respect to the copper substrate. This difference will be discussed later. In these networks an adatom is shared equally between two adjacent molecules, which makes it a promising building block for the formation of the honeycomb network.

Figure 4.10 shows a diagram of the formation energies for the different structures. This energy was defined as

$$\begin{aligned} E_{\text{form}} &= \frac{1}{3}\left[E_{\text{tot}} - \left(3E_{\text{DPDI}} + E_{\text{Cu(111)}}\right)\right. \\ &- n\left(E_{\text{Cu/Cu(111)}} - E_{\text{Cu(111)}}\right) \\ &+ \left. 3m\left(E_{\text{H/Cu(111)}} - E_{\text{Cu(111)}}\right)\right], \end{aligned} \tag{4.3}$$

where E_{tot} is the total energy of the investigated network, E_{DPDI} is the energy of a DPDI molecule in vacuum, $E_{\text{Cu(111)}}$ the energy of the bare Cu(111) slab, $E_{\text{Cu/Cu(111)}}$ is the energy of a copper slab with one adatom, and $E_{\text{H/Cu(111)}}$ is the energy of a single hydrogen atom adsorbed on a Cu(111) slab. The integer n is the total number of adatoms in the network per surface unit cell, and m is the total number of H atoms dehydrogenated from each DPDI molecule. In other words $m = 0$ for the intact molecule, $m = 2$ for the dehydro-DPDI species, and $m = 6$ for the tridehydro-DPDI species. Negative formation energy indicates an exothermic reaction (stabilisation) with respect to the reference systems.

The trend of the formation energies in Figure 4.10 shows that the structures consisting of intact DPDI molecules are the most stable ones. This is due to the energy cost to dehydrogenate the molecule. However, the calculated formation energies are those at 0 K. The network formation occurs at temperatures of around 200 °C and at these temperatures one can expect that dehydrogenation of the nitrogen atoms does occur. The question then raises what is the probability for an already dehydrogenated H-atom atom to rejoin a molecule. It is known that atomic hydrogen is desorbed from the Cu(111) surface at these temperatures [115], and hence in the UHV system these dehydrogenated atoms are most probably removed from the thermal equilibrium.

For a more correct analysis of the energetics one would need to take into account the temperature and entropy in the calculations. However, due the the size and the many degrees of freedom of the system, such approach is not practical. Our approach to make conclusions about the structure of the honeycomb network relies instead on the core-level binding energies of the nitrogen atoms. We know from the XPS experiments that the nitrogen atoms in the network only exhibit one chemical environment. Hence, by determining the core-level shifts between the nitrogen atoms within the separate networks it is possible to exclude networks that exhibit

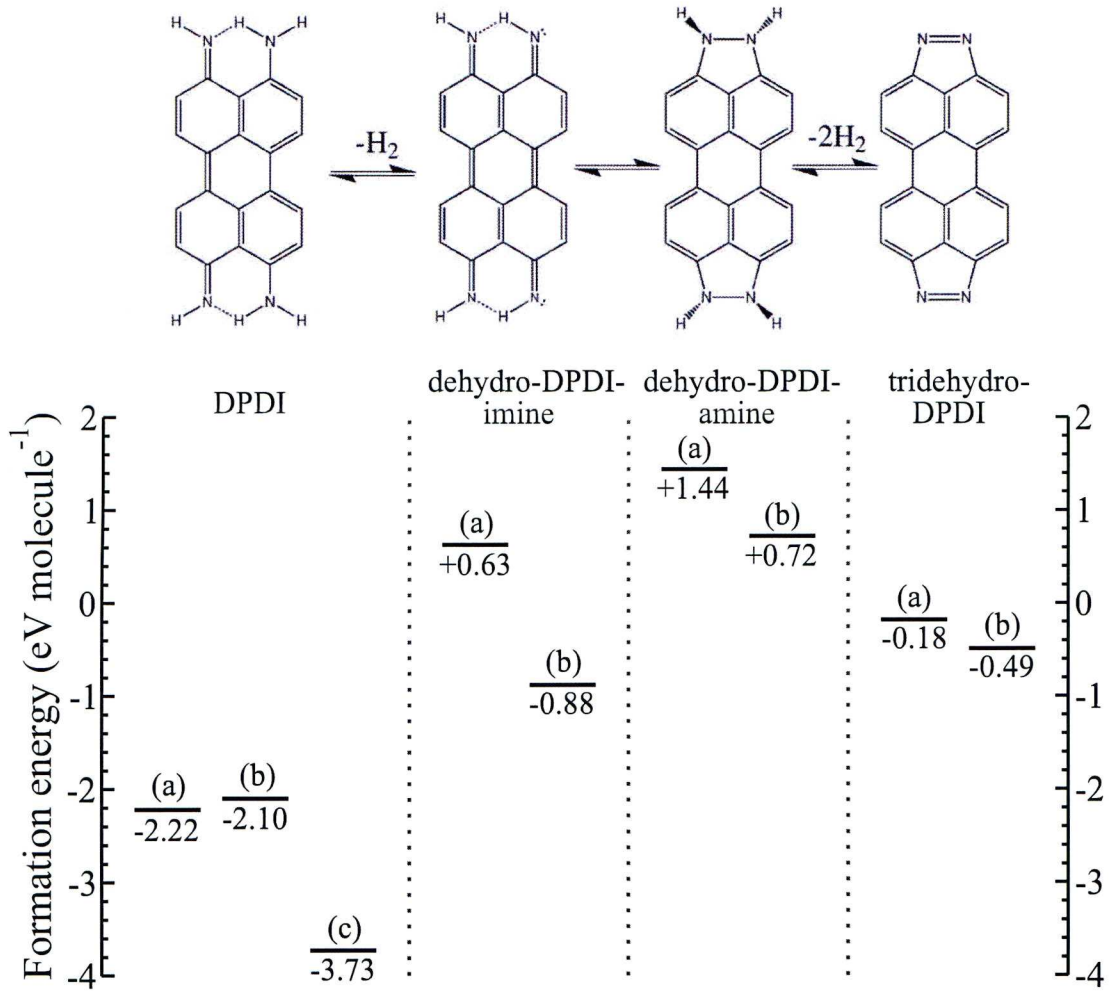

Figure 4.10: Formation energies for the honeycomb structures illustrated in Figures 4.6-4.9 consisting of DPDI, tridehydro-DPDI-imine, tridehydro-DPDI-amine and tridehydro-DPDI, respectively. The energies were calculated using Eq. (4.3). Note that the honeycomb network will later be shown to have structure (b) of tridehydro-DPDI species which is not the most energetically favourable network.

different core-level binding energies of the nitrogen atoms. Furthermore, the relative chemical shift of the nitrogen atoms in the honeycomb network with respect to that in the mobile phase is known experimentally from XPS. If the structure of the molecules in the mobile phase was known it would in principle be possible to simulate the chemical shift of the nitrogen atoms in the honeycomb networks relative to the mobile phase, and compare these simulated shifts to the experimental chemical shift given by the XPS data.

Understanding the mobile phase is thus important for making conclusions about the honeycomb network. Therefore, before discussing further the structure of the honeycomb network the geometrical structure of the molecules in the mobile phase will be discussed.

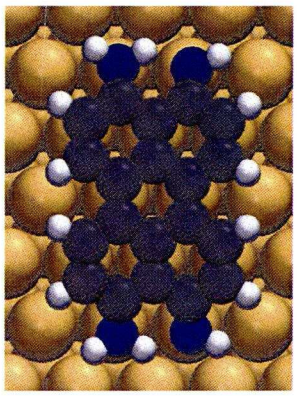

Figure 4.11: The most stable adsorption configuration of a single DPDI molecule adsorbed on Cu(111).

Mobile phase of DPDI on Cu(111) To model the mobile phase of DPDI on Cu(111), illustrated in Figure 4.2 (a), we assumed that the molecules behave like a two-dimensional lattice gas, and only the adsorption configuration of a single molecule on the surface was considered. An extensive study of different adsorption geometries of the isolated molecules was carried out, and a detailed description of the different adsorption geometries which were investigated is given in Appendix A.2.

The most stable adsorption configuration, illustrated in Figure 4.11, has an adsorption energy of -0.59 eV molecule^{-1}, defined by

$$E_{\text{ads}} = E_{\text{DPDI/Cu(111)}} - \left(E_{\text{DPDI}} + E_{\text{Cu(111)}}\right), \tag{4.4}$$

where $E_{\text{DPDI/Cu(111)}}$ is the total energy of DPDI adsorbed on Cu(111), E_{DPDI} is the total energy of the isolated DPDI molecule, and $E_{\text{Cu(111)}}$ is the total energy of the isolated Cu(111) surface. The calculated chemical shift with respect to the imine (NH) nitrogen is given in Table 4.2.

Table 4.2: Simulated core-level shifts and distances from first surface layer for the most energetically favourable adsorption site for an isolated DPDI molecule on Cu(111), as illustrated in Figure 4.11. The experimental values are given in the paranthesis, with the chemical shift given with respect to the NH nitrogen atoms.

		Chemical environment	
		NH	NH_2
Relative chemical shift (eV)	N-atoms	0 (0)	1.86 (1.82)
Distance to surface (Å)	N-atoms	2.31 (2.20)	2.42 (2.40)
	C-atoms	3.36 (2.68)	

Considering the nitrogen atoms, the model of the isolated DPDI on Cu(111) agrees well both with the chemical shift from the XPS experiments as well as the height of nitrogen atoms above the surface from XSW experiments of the mobile phase. The height of the amine nitrogen atoms above the surface agrees very well with the XSW experiments, while the imine

nitrogen atoms are found slightly too far away from the surface in the calculations. However, the average height of the C-atoms to the Cu surface is too large in the simulations. We will show in Section 4.5 that this discrepancy is due to the absence of non-local dispersion interactions in semi-local DFT. The perylene core mainly experiences a repulsive interaction from the substrate in semi-local DFT and by including the dispersion interactions the perylene core comes closer to the surface. However, the effects of the non-local dispersion forces on the core-level shifts on the nitrogen atoms are very small. The low-energy peak and the high energy peaks in the XPS experiments are assigned to the imine nitrogen and the amine nitrogen, respectively. The calculations are consistent with the XSW experiments showing that the imine nitrogen is closer than the amine nitrogen to the copper substrate.

In the following paragraphs the nitrogen atoms in the most stable adsorption geometry of the isolated DPDI molecule adsorbed on Cu(111) will be used as the reference for the calculation of chemical shifts of the nitrogen atoms in the different honeycomb networks in Figures 4.6–4.9.

Core-level shifts of honeycomb networks Before considering the results from the calculations we recall the results from the XPS experiments. These latter results showed that the honeycomb network exhibits only one chemical environment on the nitrogen atoms. Furthermore, the chemical shift of the core-levels for the nitrogen atom is (1.50 ± 0.10) eV relative to the imine nitrogen of the molecules in the mobile phase.

The simulated N1s core-level shifts with respect to the imine nitrogen of the isolated molecule, together with the heights of nitrogen and carbon atoms, are summarised in Table 4.3. From the simple fact that we are searching for a structure with one N1s core-level binding energy it is possible to reject the structures formed by the intact DPDI molecule, which all exhibit two distinct N1s core levels.

Also the structures formed from dehydro-DPDI-imine molecules can be excluded using the same argument as for the intact DPDI. The nitrogen atoms in this molecule experience two different chemical environments due to the intra-molecular hydrogen bond, which is reflected in the simulated core-level shifts. Furthermore the calculated N1s core-level binding energies are both too small and have the wrong sign for this molecule to explain the XPS results.

Regarding the structures formed with the dehydro-DPDI-amine molecule as a building block, they are symmetric with respect to the nitrogen atoms and exhibit a single N1s core-level. However, the simulated shift is much larger than the observed one in the XPS experiments. Hence also dehydro-DPDI-amine can be rejected as a possible molecular building block.

Tridehydro-DPDI honeycomb networks We find that one of the two networks formed by the tridehydro-DPDI molecules, Figure 4.9 (b), gives excellent agreement with the experimental XPS data. In these networks the molecules are coordinated to Cu adatoms in a similar

Table 4.3: Simulated N1s chemical shifts and heights above the surface of the N-atoms, and average height to the surface of the C-atoms for the investigated honeycomb structures, in which either DPDI, dehydro-DPDI-imine, dehydro-DPDI-amine or tridehydro-DPDI were used as molecular building block. The structures for the different molecules are illustrated in Figure 4.6, 4.7, 4.8 and 4.9, respectively. The chemical shifts are given with the imine nitrogen of the isolated DPDI molecule adsorbed on Cu(111) as reference, *i.e.* with respect to the low-energy peak in XPS of the mobile phase.

	Chemical shifts (eV)	Distance to surface (Å)	
	N-atoms	N-atoms	C-atoms
Experimental			
	1.50 ± 0.10	2.83 ± 0.03	3.00 ± 0.04
DPDI			
(a)	-0.25, 2.13	3.11, 3.79	3.64
(b)	0.24, 1.40	3.77, 4.27	4.25
(c)	0.10, 2.14	3.89, 4.05	4.37
Dehydro-DPDI-imine			
(a)	-0.49, -0.06	2.15, 2.18	3.31
(b)	-0.61, -0.37	2.92, 3.55	3.47
Dehydro-DPDI-amine			
(a)	3.44, 3.83	3.85, 4.35	3.95
(b)	3.91	3.99	4.46
Tridehydro-DPDI			
(a)	1.76	3.05	3.37
(b)	**1.47,1.52**	**2.90**	**3.20**

manner as for the Cu-TAPP network: One adatom is shared between two nitrogen atoms of adjacent tridehydro-DPDI molecules, resulting in a junction of three molecules coordinating through three adatoms. The adsorption energy of the two networks was defined as

$$E_{\text{ads}} = \left[E_{\text{tot}} - \left(3E_{\text{tridehydro-DPDI}} + E_{\text{Cu(111)}}\right)\right]/3, \tag{4.5}$$

where, E_{tot} is the total energy of the structurally optimised coordination network on Cu(111), $E_{\text{tridehydro-DPDI}}$ is the total energy of the structurally optimised tridehydro-DPDI molecule in vacuum and $E_{\text{Cu(111)}}$ is the total energy of the structurally optimised Cu slab with Cu adatoms. It was found that the network in Figure 4.9 (a) has an adsorption energy of -3.96 eV molecule^{-1} whereas the network in Figure 4.9 (b) has an adsorption energies -4.27 eV molecule^{-1}. Thus, the most stable one is also the one which is in best agreement with the XPS experiments.

The structural differences between the two tridehydro-DPDI networks are understood from Figure 4.12 where larger areas of the two networks are shown. In the first structure (a) all adatoms are symmetrically positioned with respect to the first Cu layer and the tridehydro-DPDI molecules. Due to the strong coordination with the molecules, the adatoms are "pulled" away from their equilibrium sites close to top sites of the Cu surface. The geometry of structure (b) is simply a translation of network (a) so that the adatoms instead sit close in hollow sites of the surface. The preference of the adatoms to adsorb to hollow sites gives rise to the energy

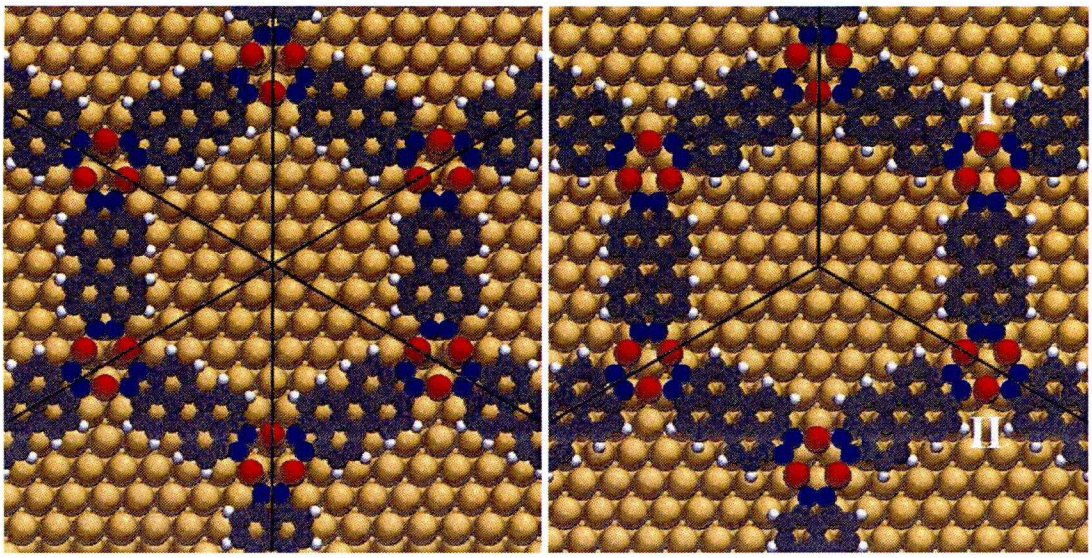

(a) (b)

Figure 4.12: Isomeric structures of the honeycomb networks of tridehydro-DPDI molecules coordinated to Cu adatoms, with adsorption energies (a) -3.96 eV molecule^{-1} and (b) -4.27 eV molecule^{-1}. Note that network (a) follows the six-fold symmetry of the first surface layer, while the network (b) has a three-fold symmetry. This allows the adatoms in (b) to sit in hollow positions, making the network with three-fold rotational symmetry (b) energetically favourable over the network with six-fold rotational symmetry (a). The black lines indicate the rotational symmetry of the networks and the adatoms are illustrated as red balls.

difference between the two networks, making network (b) 0.31 eV molecule^{-1} more stable than network (a).

Note that for the most stable network from tridehydro-DPDI molecules, illustrated in Figure 4.12 (b), the coordination network breaks the six-fold rotational symmetry of the first Cu layer and instead a three-fold rotational symmetry is obtained. The three-fold rotational symmetry of network (b) has the consequence that two inequivalent crossings of three molecules exist in each unit cell, labelled as I and II in Figure 4.12. In the simulated core-level shift this gives rise to a small chemical shift of 50 meV between nitrogen atoms in the two inequivalent crossings of three molecules per unit cell. This energy difference is too small to be resolved in the XPS experiments. However, the energy difference is experimentally observable in STM by the fingerprint associated with the coordination between molecules and adatoms, which gives additional support for this structure being formed, as will be discussed in Section 4.3.1.

It is worth noting that the tridehydro-DPDI honeycomb network, shown in Figure 4.12 (b) not only reproduces the XPS experiments with high accuracy, but gives also the heights of the nitrogen and carbon atoms in good agreement with XSW experiments. Finally, the adsorption energy of -4.27 eV molecule^{-1} compared to TAPP network with an adsorption energy of -2.40 eV molecule^{-1} is consistent with the experimental observation that the honeycomb network formed from DPDI molecules is considerably more stable than the TAPP network.

Summary

We have shown by a combined theoretical and experimental study that during the formation of the honeycomb network the DPDI molecule undergoes a chemical transformation, in which the nitrogen atoms are fully dehydrogenated, resulting in tridehydro-DPDI. The network is stabilised by Cu adatoms, where one adatom coordinates two nitrogen atoms of adjacent tridehydro-DPDI molecules, as illustrated in Figure 4.12 (b). This conclusion is supported by the fact that DFT can only reproduce all experimental data (STM, LEED, XPS, XSW) for this structure.

4.2.3 Resemblance between free and surface-commensurate networks

In this section we will discuss the importance of the commensurability of the coordination networks with the Cu(111) substrate and what role the substrate plays in determining the unit cell. First the TAPP network will be discussed, followed by the tridehydro-DPDI network. This section will end with a summary of the results for the two networks.

Note that the calculations done in this subsection were done using a 500 eV kinetic energy cut-off for the plane waves. This was done to make sure that energies obtained from using different unit cell sizes can be compared with a numerical accuracy of less than 1 meV.

TAPP network

From the simple bonding argument that for the most stable Cu–TAPP overlayer all N–Cu bond distances should be equal and also that the N–Cu–N bond angles should be the same, the most stable unit cell of the free Cu–TAPP overlayer has a D_{4h} symmetry. The two surface unit cell vectors are then of equal length, and perpendicular with respect to each other. By optimising the internal structure of the free Cu–TAPP overlayer for different unit cell sizes, constrained to have D_{4h} symmetry, the most energetically favourable unit cell was found, Figure 4.13. The dimension of this unit cell is 17.63 $\times$ 17.63 Å^2. However, the adatoms have a preference to adsorb on hollow sites of the Cu(111) substrate, hence for a long-ranged ordered structure to be formed a unit cell commensurate with the Cu(111) surface is essential. By sampling all possible unit cells commensurate with Cu(111), within reasonable deviations in size and shape from the optimised unit cell of the free overlayer, two unit cells were found: The experimentally observed cell, defined in Eq. (4.1), and a second possible unit cell defined by

$$\begin{pmatrix} 7 & 0 \\ 4 & 8 \end{pmatrix} \begin{pmatrix} \vec{a}_1 \\ \vec{a}_2 \end{pmatrix}, \tag{4.6}$$

where $\vec{a}_1$ and $\vec{a}_2$ are the primitive surface unit cell vectors of Cu(111).For the free Cu–TAPP overlayer, the two unit cells give very similar energies, with the alternative unit cell being the more stable one by 12 meV molecule^{-1}. However, when adsorbed on Cu(111), the experimentally observed unit cell was found to be 112 meV molecule^{-1} more stable than the alternative unit cell, from a comparison of the adsorption energies defined by Eq. (4.2). Thus,

the molecule-substrate interaction is decisive in determining the unit cell for the porous TAPP network on Cu(111).

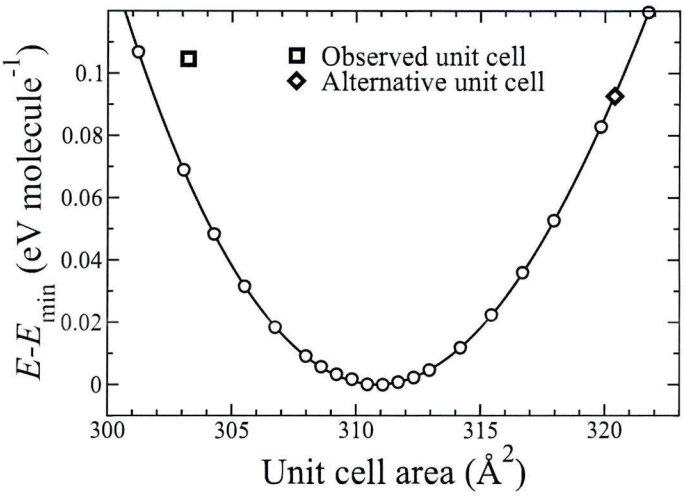

Figure 4.13: Energy as a function of unit cell area of isolated, structurally optimised, Cu-TAPP coordination networks. The solid line is the results for cells with D_{4h} symmetry. The areas and energies of the observed unit cell (□) and an alternative unit cell (◇), both being commensurate with the Cu(111) surface, are included.

The energy difference between the two unit cells when the Cu–TAPP overlayer is adsorbed on the Cu(111) surface can be partly understood from the structural deformation energies. For the Cu adatoms we defined this quantity as the energy difference between the system with the four adatoms on the surface in the geometry of the surface network and the four adatoms on the surface relaxed into the nearest hollow site on the surface (both systems with the TAPP molecules absent). The difference between structural deformation energies of the adatoms for the two unit cells is negligible (less than 1 meV per adatoms). Considering the deformation energy of the TAPP molecule, defined as the energy difference between the free molecule in the surface network geometry and the structurally optimised free molecule, this deformation energy is 62 meV larger for the surface network with the competing unit cell than the network with the experimentally determined unit cell. Hence the structural deformation energy can account for about 30% of the total energy difference between the surface networks with the two different unit cells.

The preference for the experimentally observed unit cell is better understood by considering the N–Cu bond lengths in the different networks. Table 4.4 gives the bond lengths for the two unit cells both for the free overlayers, and the surface coordinated overlayers. The N–Cu distance of the most energetically favourable D_{4h} unit cell is 1.87 Å. Hence for the free overlayers the observed unit cell gives slightly too small N–Cu distances, while the competing unit cell gives slightly too large N–Cu distances, comparing with the corresponding distances for the optimised free overlayer. However, when adsorbed on the Cu(111) surface, the Cu adatoms are displaced out of the molecular plane, resulting in an elongation of the N–Cu bond lengths.

Table 4.4: N-Cu bond lengths of the Cu-coordinated TAPP overlayer for the observed and alternative unit cells, with and without the Cu substrate. Note that in the isolated Cu-coordinated TAPP overlayer the optimum N-Cu distance is 1.87 Å.

	N-Cu bond length (Å)	
	On Cu(111)	Isolated
Observed unit cell	2.00–2.11	1.84
Alternative unit cell	2.12–1.18	1.93

This favours the observed unit cell which has N–Cu bond lengths closer to the optimised free overlayer than the surface network with the competing unit cell.

Tridehydro-DPDI network

In a similar manner as for the isolated TAPP network, the isolated honeycomb network of tridehydro-DPDI molecules and Cu atoms was structurally optimised using different unit cell sizes. Note that, in contrary to the unit cell of the surface network of TAPP, the surface network of tridehydro-DPDI already has the optimised symmetry. When searching for the optimised unit cell this symmetry of the unit cell was assumed which results in a perfect honeycomb pattern of tridehydro-DPDI molecules and Cu atoms. In other words, the surface unit cells under considerations are defined by

$$\delta \begin{pmatrix} 10 & 0 \\ 0 & 10 \end{pmatrix} \begin{pmatrix} \vec{a}_1 \\ \vec{a}_2 \end{pmatrix}, \tag{4.7}$$

where $\vec{a}_1$ and $\vec{a}_2$ are the primitive surface unit cell vectors of Cu(111) and δ is a real number (close to unity) that scales the experimental surface unit cell. In this unit cell all N-Cu bond lengths and N-Cu-N bond angles are allowed to be equal, hence allowing all N-Cu bonds to be optimised. For the isolated networks the Cu atoms are in the plane of the overlayer. The resulting unit cell area versus total energy plot is illustrated in Figure 4.14.

For the optimised unit cell the length of each of the two surface unit cell vectors is 17.76 Å, which is to be compared to 17.81 Å for the experimental unit cell. Hence, the results show that the experimentally observed (commensurate) unit cell is very close to the optimised one for the free network, with an energy difference between the optimised and experimental cell of less than 10 meV molecule^{-1}. The optimised N-Cu bond distance is 1.85 Å, which is in very close to that for TAPP of 1.87 Å. In the tridehydro-DPDI surface network this distance is found to be in the range 1.94–1.95 Å. The N-Cu distances are not all equal in the surface network due to the asymmetry between the two "crossings" per unit cell as discussed earlier.

4.2.4 Nature of the coordinative bonding

To understand the difference in structural stability between the Cu-TAPP and Cu-DPDI coordination network we have characterised the coordinative bonding in the two networks. This section will discuss the bonding mechanism by looking at the charge transfer between substrate,

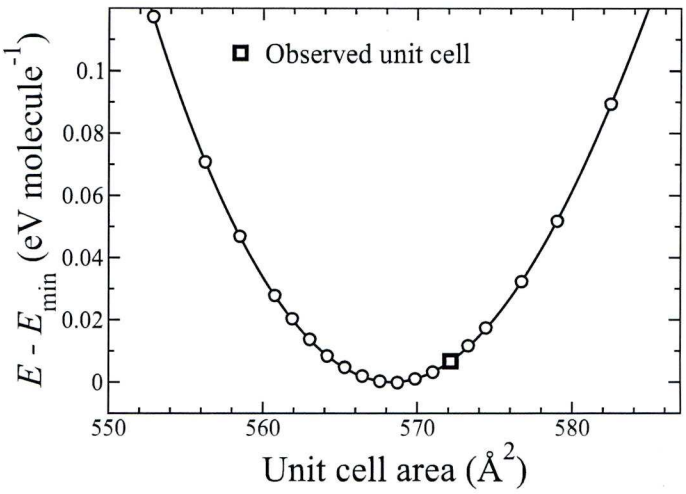

Figure 4.14: Energy as a function of unit cell area of isolated, structurally optimised, Cu-coordinated tridehydro-DPDI networks. The unit cells are given by Eq. (4.7) defining by symmetry considerations the most stable unit cell for the honeycomb network. The circles indicate the calculated data points and the square (□) indicates the experimentally observed unit cell, which is commensurate with the Cu(111) surface.

adatoms and molecules in the two systems through an atoms-in-molecules approach combined with an investigation of the orbitals of the molecules that are affected by the interaction with the Cu adatoms and substrate.

Bader charge analysis

The net electronic charge of the different fragments of the different systems was calculated according to the Atoms-in-Molecules (AIM) approach by Bader [116, 117]. Table 4.5 shows the net electronic charge of the molecules and Cu adatoms for the various systems, together with the charge for the Cu slabs which was calculated as the negative value of the total charge over molecules and Cu adatoms. Starting with the isolated Cu-TAPP network, each adatom donates -0.57 e to the TAPP molecules, resulting in a net charge of -1.14 e per molecule. For the surface network, the charge donation from the adatoms to TAPP is slightly reduced, and the network as a whole stays (almost) neutrally charged. The fact that the Cu adatoms are important for electron transfer into the TAPP molecules can be shown by artificially removing the adatoms from the network, in which case the TAPP molecules become close to neutral.

For the Cu-DPDI network a quite similar trend as the one for TAPP is observed, for the isolated network the net charge on the tridehydro-DPDI molecules and Cu atoms are almost identical as those for the Cu-TAPP network, +0.59 e per adatom and -1.18 e per molecule. However, for the surface network the net charge on the molecules stays almost constant for DPDI in contrast to TAPP, with most of the electrons contributed from the Cu adatoms. Furthermore, if the adatoms are removed, there is still a considerable charge transfer into the tridehydro-DPDI molecule from the surface, which is not the case for TAPP.

Table 4.5: Net electronic charges from the Bader analysis of molecules and Cu adatoms of the isolated coordination networks, the networks on Cu(111) and the networks on Cu(111) with either the molecules or the adatoms removed. The electronic charges of the Cu slabs are given the opposite value of the total charge over molecules and Cu adatoms, since the net charge of each system is zero. Note that for the Cu-TAPP network each unit cell holds two molecules and four adatoms, while for the Cu-DPDI network each unit cell holds three molecules and six adatoms.

	TAPP network		
	TAPP (e/molecule)	Cu adatoms (e/adatom)	Cu slab (e/cell)
Isolated network	-1.14	+0.57	–
Network on Cu(111)	-0.86	+0.47	-0.16
–Adatoms removed	-0.18	–	+0.18
	tridehydro-DPDI network		
	tridehydro-DPDI (e/molecule)	Cu adatoms (e/adatom)	Cu slab (e/cell)
Isolated network	-1.18	+0.59	–
Network on Cu(111)	-1.22	+0.53	+0.46
–Adatoms removed	-0.89	–	+2.65

Molecular orbital projected density of states

The mechanism behind the trend in the charge analysis becomes more transparent by considering the molecular orbital projected density of states (MO-PDOS). The MO-PDOS was calculated as projections of the orbitals of either TAPP or tridehydro-DPDI onto the electronic states for different networks: For either of the networks the MO-PDOS was calculated for an isolated network (no surface), the surface network, and for the surface network with the adatoms being artificially removed.

The MO-PDOS is shown for the TAPP network in Figure 4.15 and for the tridehydro-DPDI in Figure 4.16. For the isolated networks (a) the (former) lowest unoccupied molecular orbital (LUMO) is fully occupied for both systems. If instead considering the networks on Cu(111) (b) the LUMO of TAPP becomes only partially occupied, while the LUMO of tridehydro-DPDI stays completely filled well below the Fermi level. The average position of the LUMO is $E_F - 1.1$ eV for tridehydro-DPDI while it is $E_F - 0.2$ eV or TAPP. So it is more favourable to move electrons from the copper substrate to the LUMO of tridehydro-DPDI than to the LUMO of TAPP.

Furthermore the nitrogen lone-pair orbitals are more affected by the tridehydro-DPDI network than by the TAPP network. In the TAPP network the states associated with the N lone-pairs for the surface network (b) are on average shifted by -2.4 eV compared to the adatom free reference structure (c). The corresponding energy shift for the tridehydro-DPDI network is -3.3 eV.

How does the filling of the LUMO of tridehydro-DPDI contribute to the stability of the

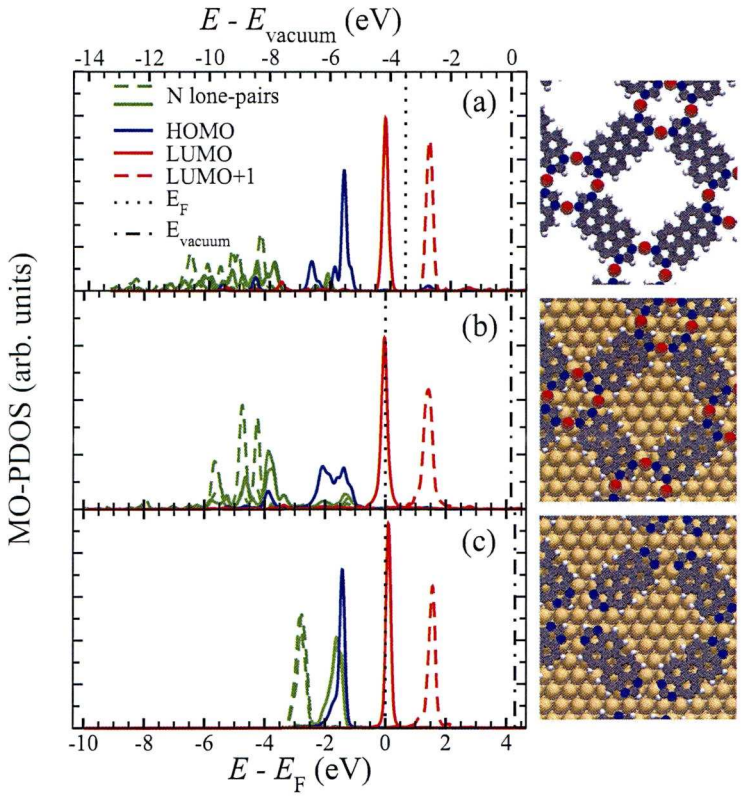

Figure 4.15: PDOS onto the molecular orbitals of TAPP of (a) the isolated network, (b) the network on Cu(111), and (c) the network on Cu(111) with the adatoms removed.

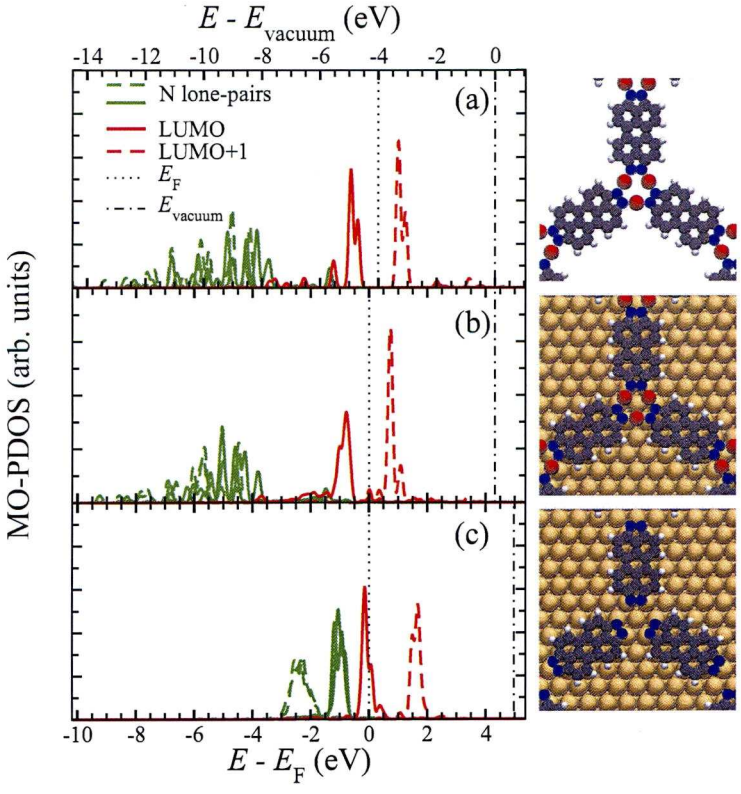

Figure 4.16: PDOS onto the molecular orbitals of tridehydro-DPDI of (a) the isolated network, (b) the network on Cu(111), and (c) the network on Cu(111) with the adatoms removed.

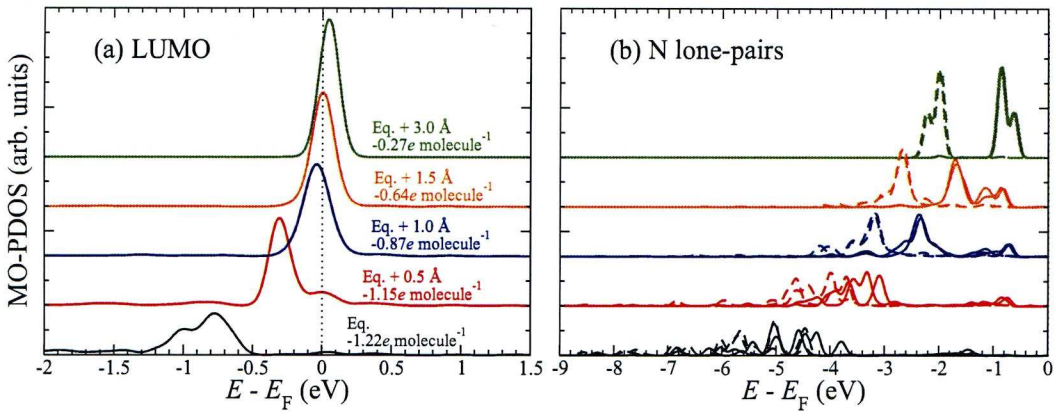

Figure 4.17: Evolution of the projected density of states onto the LUMO (a) and the orbitals associated with the nitrogen lone-pairs (b) of tridehydro-DPDI as the molecule is moved away from its equilibrium configuration on the surface. The perpendicular displacement of the molecule with respect to the surface, as well as the Bader charge integrated over the molecule is indicated for each curve. As tridehydro-DPDI is moved away from the surface the LUMO moves above the Fermi level and the molecule becomes less negatively charged, at the same time as the states associated with the nitrogen lone-pair orbitals shift to higher energy.

honeycomb network? The LUMO becomes filled when the molecule comes into contact with the substrate which results in an energy gain. However, what will happen to the occupancy of this LUMO if the molecule is lifted away from the surface? Figure 4.17 (a) illustrates how the LUMO is affected as tridehydro-DPDI is moved away from the surface showing that the LUMO is gradually moved above the Fermi level as the interaction between the molecule and the substrate is decreased. Thus, when forcing the molecule away from the surface, at the same time one forces the molecule to back donate electrons to the substrate. This result is in analogy with studies [71, 118] of another perylene derivative, namely 3,4,9,10-perylene-tetracarboxylic acid dianhydride (PTCDA). It has been shown both from experiments [118] and theory [71] that the electron transfer into the LUMO is dependent on the height of the PTCDA above the surface; the closer the molecule is to a metal surface the larger the electron transfer is into the LUMO. A similar behaviour is found for tridehydro-DPDI on the Cu(111) surface, as shown in Figure 4.16 (a). However, in contrast to the studies of the PTCDA molecule, the electron transfer into tridehydro-DPDI mainly comes from the copper adatoms and not the substrate. It is noteworthy that the Bader charges summed over the tridehydro-DPDI molecule follows exactly the trend of the LUMO, as the LUMO becomes less occupied the molecule becomes less negatively charged. This shows that the Bader charge analysis can be used as a consistent tool for analysing electron transfer in this type of molecular system on metal substrates.

The extraordinary stability of the tridehydro-DPDI compared to the TAPP network is a combination of the stronger interaction between the Cu adatoms with the N lone-pairs as well as a larger energy gain by filling the LUMO orbital in tridehydro-DPDI. Having in mind that there are four lone-pair orbitals, they have probably a larger influence on the stability compared to the single LUMO. The electron transfer into the LUMO may still affect the nitrogen lone-pair

orbitals: a type of bonding that can be understood in terms of the well-established σ-donor/π-backbonding interaction in coordination chemistry [119]. It is a well known effect that there is a synergism between the σ-donor and the π-backbonding interactions: a stronger σ-donation is accompanied with a stronger π-backbonding. The σ-donation in our coordination networks is reflected by the lowering of the lone-pair orbitals while the π-backbonding is reflected by the filling of the LUMO in our MO-PDOS plots [120]. Comparing the TAPP and tridehydro-DPDI networks the filling of the LUMO in the former is only partial and the nitrogen lone-pairs are lowered on average by 2.4 eV. On the other hand for the tridehydro-DPDI network the LUMO is completely filled and the nitrogen lone-pairs are lowered on average by 3.3 eV. Hence, the synergism between the σ-donation and the π-backbonding may be valid also for surface coordination networks, reminiscent with for example the bonding of carbon monoxide on transition metals [119].

The coordinative bonding is not only characterised by the covalent bonds reflected in lowering and hybridisation of molecular orbitals. Due to the charge rearrangement in the systems, also an electrostatic Coulomb contribution to the interaction has to be taken into account. This interaction comes not only from the attraction between the positively charged adatoms and negatively charged molecules, but also from the interaction of the negatively charged molecules with the metal substrate. Since the LUMO of tridehydro-DPDI is fully occupied while in the TAPP network it is only partially occupied, the electrostatic interaction between the copper substrate and tridehydro-DPDI is therefore stronger than for TAPP. This might explain why the height of the molecules in the tridehydro-DPDI network is in a better agreement with XSW experiments than for the molecules in the TAPP network.

To summarise the different interactions, there is a covalent contribution reflected in the hybridisation of nitrogen lone-pair orbitals together with the filling of the LUMO of the molecules. Due to negatively charged molecules, there is also an electrostatic contribution, both between the molecules and adatoms as well as between the molecules and the copper substrate. One important point is missing in this bonding picture, namely the contribution from non-local dispersion forces, which by definition are not included in the semi-local DFT calculations. In Section 4.5.2 the influence of these non-local interactions on the structure of the coordination networks is discussed, as well as the indirect influence on the coordinative bonding will be discussed.

4.3 STM fingerprint of metal-ligand coordination

In the previous section it was shown that in the porous surface networks formed by either TAPP or DPDI the molecules are coordinated to Cu adatoms. In neither of the two networks can the adatoms be resolved in topographic STM images. However, it is possible to find a distinct resonance for both networks in bias-dependent STM images, which was found to be a signature of the adatom–molecule coordination. In this section we will discuss how the adatoms can give rise to this signature.

4.3.1 LDOS of surface supported networks

TAPP network

In STM experiments, a characteristic protrusion is observed when tunnelling into the sample at high tunnelling voltages. Figures 4.18 (a-c) show a comparison of experimental topographic STM images of the TAPP network at -1.0 V (a) and at higher bias voltages where the characteristic bright protrusion is observed, +2.7 V (b) and +3.0 V (c).

The experimental STM images are well reproduced in the simulated constant current images, Figure 4.18 (d-f). At an energy of 1.0 eV below the Fermi level the LUMO of TAPP [112] provides the dominant contribution to the simulated image, Figure 4.18 (d). A bright protrusion, representing a high tunnelling current feature, was observed at the same location as in experiments when increasing the energy to 3.2 eV above the Fermi level, Figure 4.18 (e), and becomes even more dominant at energies of 3.4 eV above the Fermi level, Figure 4.18 (f). Hence, the experimentally observed high tunnelling current feature can also be identified within the simulated images, obtained by integration of the LDOS from the Fermi level to 3.2–3.4 eV.

Furthermore, from our theoretical study it is possible to show that Cu adatoms are a key ingredient for the appearance of this characteristic feature in the LDOS. When removing the adatoms from the porous network while keeping the geometrical structure of the adsorbed TAPP molecules fixed in the calculations, the bright protrusion in the common crossing of four molecules (equivalent with the geometrical centre of the four adatoms) was found to be absent at all energies. Figure 4.18 (g) shows the LDOS 6 Å above the first Cu layer as a function of the energy at the lateral position of the common crossing of four molecules for the network with adatoms and the network in the absence of the adatoms, as well as above the TAPP molecule. The LDOS indicates that the bright protrusion observed in the STM images of the porous surface network at large positive sample bias results from electronic states at an energy of about 3.3 eV above the Fermi energy (0.8 eV below the vacuum level). This resonance disappears when artificially removing the adatoms from the network. This supports our previous conclusion that the Cu adatoms are involved in the formation of the porous TAPP network.

So far we have shown that the characteristic high tunnelling current feature observed in the centre of four adatoms in STM is a signature of the adatoms being present in the network. Furthermore, it can be shown that also the molecules are important for this protrusion to appear, since it cannot be explained by solely the Cu adatoms. If the adatoms are held in their position in the porous network while the TAPP molecules are removed, a single bright protrusion with the same characteristics as the one for the TAPP surface network cannot be found in the simulated LDOS. It is possible to find a bright protrusion in the centre of the adatoms at distances far away from the surface (10Å), as the LDOS originating from the four adatoms merge into a single protrusion. However, at a distance of 6Å from the surface the adatoms in most cases give rise to four distinct protrusions, and more importantly, a single protrusion that is most dominant in the centre of the adatoms of the TAPP surface network cannot be found for this

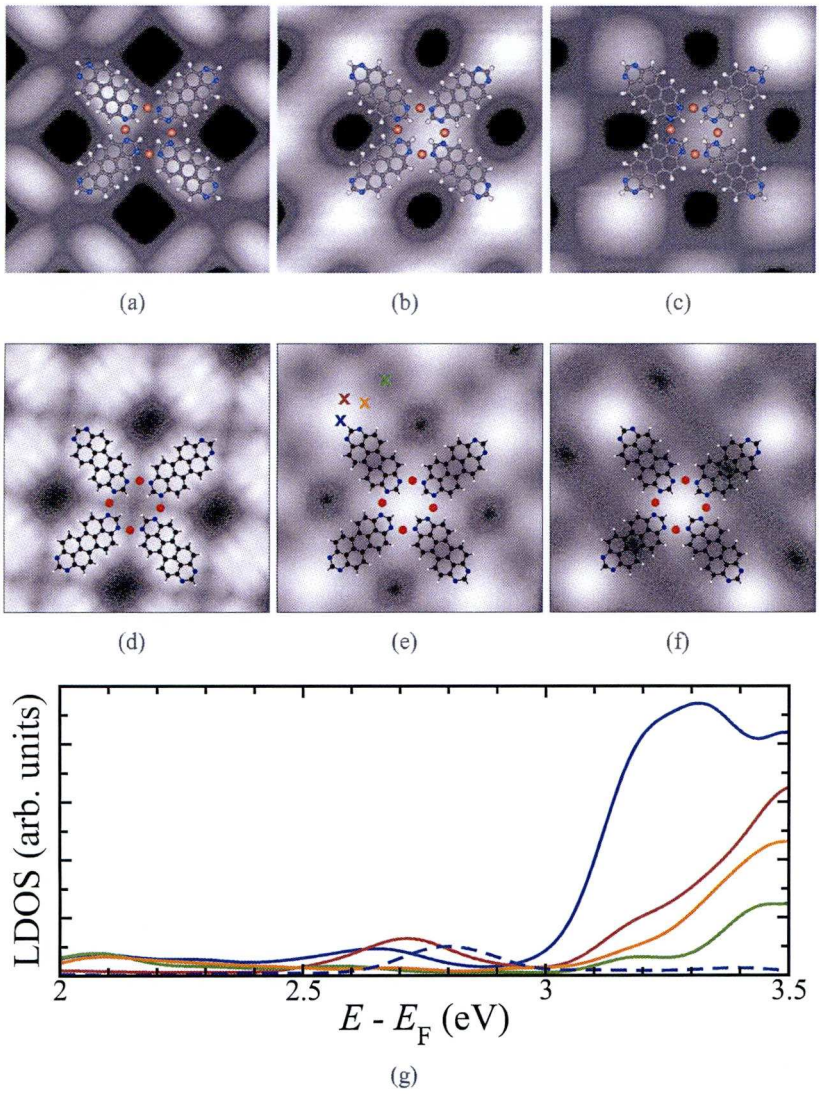

Figure 4.18: Bias dependence of (a-c) experimental and (d-e) simulated constant current STM images of the TAPP coordination network on Cu(111). The experimental images were obtained above the same region with an area of 4×4 nm^2. Tunnelling parameters were (a) -1V/20pA, (b) 2.7V/1pA, (c) 3V/1pA. The LDOS in the simulated images was integrated from the Fermi level, E_F, to (d) E_F-1.0 eV, (e) E_F+3.20 eV, (f) E_F+3.4 eV. Ball and stick models of the molecular structure of TAPP including the Cu adatoms (red balls) have been superimposed in the images. The images (a-e) are taken from [121]. The LDOS (g) was calculated at a height of 6Å above the uppermost Cu layer and at the lateral positions indicated in (e). The dashed curve shows the LDOS above the crossings in absence of the adatoms.

distance.

Tridehydro-DPDI network

A similar high tunnelling current phenomenon as the one observed for the TAPP network is seen in the STM images of the DPDI network. Figure 4.19 (a-c) shows the experimental topographic STM images at 1.5 V (a), 2.9 V (b) and 3.4 V (c). Note that, in contrast to the TAPP network, the tridehydro-DPDI network has two crossings per unit cell. In the experimental image taken at 2.9 V it is in fact possible to distinguish between the two crossings, Figure 4.19 (b), as the bright protrusions appear at different intensities in the two crossings. Figure 4.20 shows a line scan at 2.9 V through the two different crossings illustrating this quite small but significant effect.

The simulated constant current images correlate well with the experimental STM images, Figure 4.19 (d-f). At an energy of 1.5 eV above the Fermi level, Figure 4.19 (d) the molecules are imaged, almost without any submolecular contrast as observed in the experimental 1.5 V image, Figure 4.19 (a). When increasing the energy in the integration window to 3.3 eV above the Fermi level, Figure 4.19 (e), a bright protrusion appears also above one of the two common crossings of three molecules per unit cell. Finally, if increasing the energy further to 3.4 eV above the Fermi level, Figure 4.19 (f), a bright protrusion appears above the second crossing, with comparable intensity to the protrusion above the first crossing. Hence, the experimentally observed effect that one of the crossings per unit cell of the network appears brighter than the other one at 2.9 V is reproduced in the simulated LDOS, albeit at slightly higher energies.

The difference between theory and experiments is that the effect is more distinct in the theoretical results, as it is possible to image a bright protrusion above one of the crossings simultaneously as the other crossing appears with low intensity in the LDOS. This effect is better visualised in the LDOS as a function of the energy above the two inequivalent crossings per unit cell, Figure 4.19. The LDOS show dominant features above both crossings in the energy range 3.3–3.4 eV, with an energy difference between the two maxima of 50 meV. In Section 4.2.2 we showed that the geometrical structure of the honeycomb network has two inequivalent crossings per surface unit cell due to the three-fold rotational symmetry of the network, illustrated in Figure 4.12 (b). The geometrically inequivalent crossings of the honeycomb network give rise to the two maxima in the LDOS, and in fact an energy difference is also found between the simulated core-level shifts of the nitrogen atoms in the two crossings.

The fact that the different brightness of the two crossings is observable in the experimental STM images for the tridehydro-DPDI network gives not only support for an adatom supported structure, it also supports the formation of the theory predicted network with three-fold rotational symmetry on the Cu(111), as illustrated in Figure 4.12 (b).

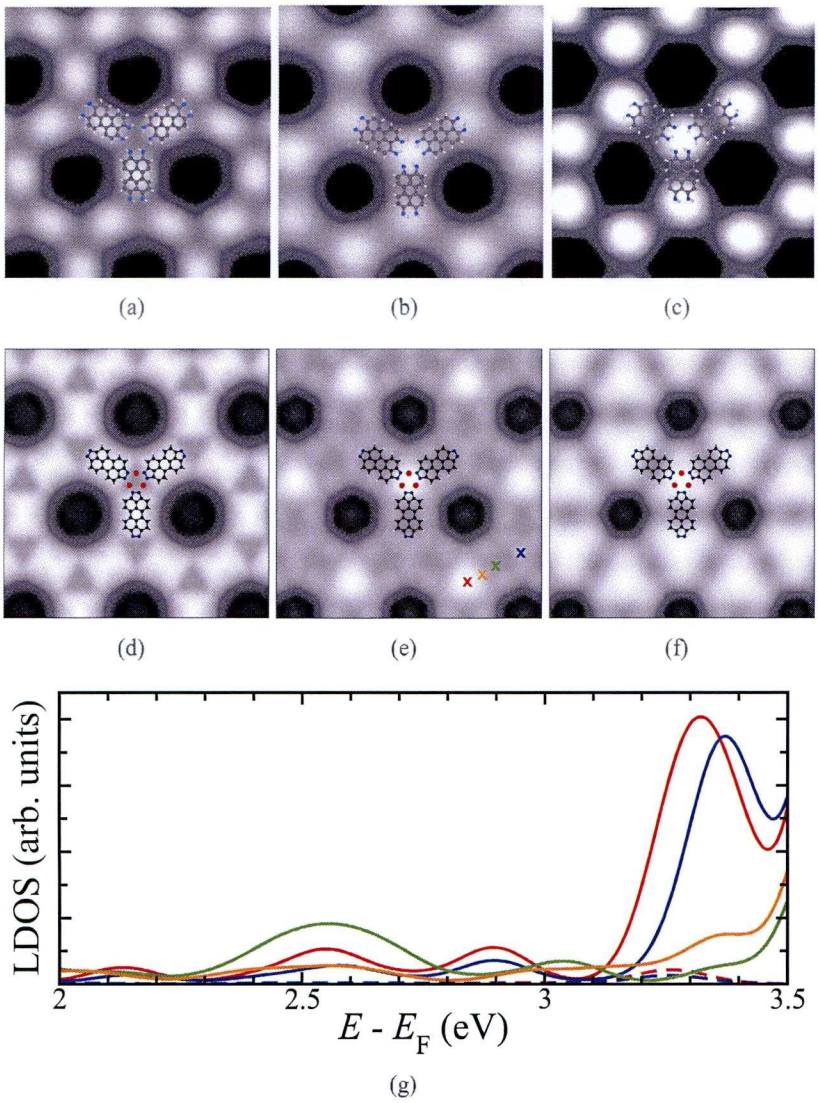

Figure 4.19: Bias dependence of (a-c) experimental and (d-e) simulated constant current STM images of the porous network formed by DPDI molecules on Cu(111). The experimental images were obtained at 5 K above the same region with an area of 6×6 nm^2 with bias voltages (a) 1.5V/10pA, (b) 2.9V/10pA, (c) 3.4V/10pA. The LDOS in the simulated images was integrated from the Fermi level, E_F, to (d) E_F+1.5 eV, (e) E_F+3.3 eV, (f) E_F+3.4 eV. Ball and stick models of the molecular structure of tridehydro-DPDI including the Cu adatoms (red balls) have been superimposed in the images. Note that the two bright protrusions per supercell appears at different intensities in the experimental image taken at 2.9 V (b) and that only one of the two crossings per supercell appear as a bright protrusion in the simulated LDOS at E_F+3.3 eV (e). The LDOS (g) was calculated at a height of 6Å above the uppermost Cu layer and at the lateral positions indicated in (e). The dashed curves show the LDOS above the crossing in absence of adatoms.

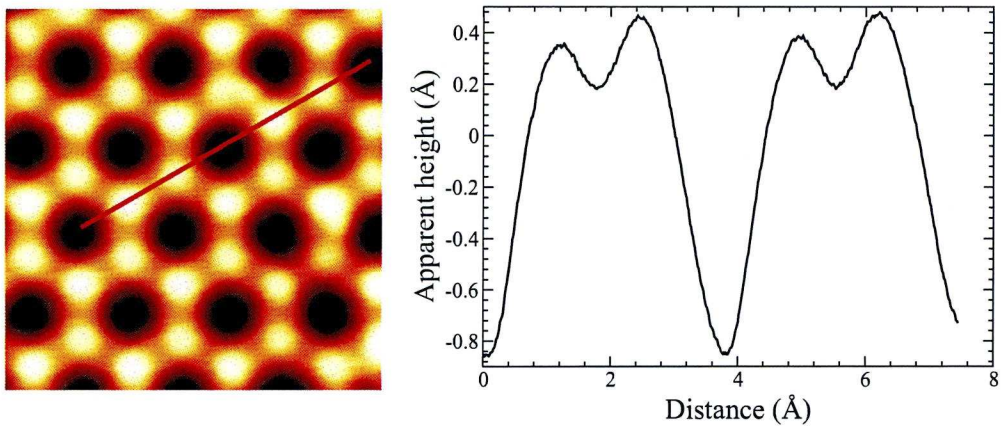

(a) (b)

Figure 4.20: (a) Experimental topographic STM image taken at 2.9 V, the two bright protrusions per surface unit cell appears with different intensities, which is illustrated by the line scan (b). The red line in (a) indicates where in the STM image the line scan was performed.

4.3.2 LDOS of free networks

The bright protrusion observed in the centre of the adatoms for both the porous surface networks depends on the presence of both the organic ligands and Cu adatoms, see Section 4.3.1. In this section we will show that this electronic feature appears solely due to the adatom-molecule interactions, and that the substrate only plays a subsidiary role. It will also be shown that the electronic states giving rise to the STM fingerprint have the same character in the two networks, and thus this can be expected to be a more general phenomenon.

By decomposing the total electron density into contributions from each electronic state it was possible to isolate an electronic state with the same character as the bright protrusion feature observed in STM experiments at high tunnelling voltage, for the networks formed from both TAPP and tridehydro-DPDI. Figure 4.21 (c,f) shows cross-sections of the charge density of this electronic state for the two networks, at a height of 5 Å above the networks.

The character of this electronic state in both of the two networks was revealed by iso-surface plots of the band-decomposed density at a much higher value of the density, shown in Figure 4.21 (a,d). The density is primarily localised around the Cu atoms as well as the carbon atoms of the organic ligands, and has a prominent p_z character for both networks. Furthermore, by decreasing the value of the density, Figure 4.21 (b,e), the density is found to decay more slowly into the vacuum around the Cu adatoms than on the molecule, giving rise to the bright protrusion observed in the STM images for the TAPP, as well for the tridehydro-DPDI porous surface networks.

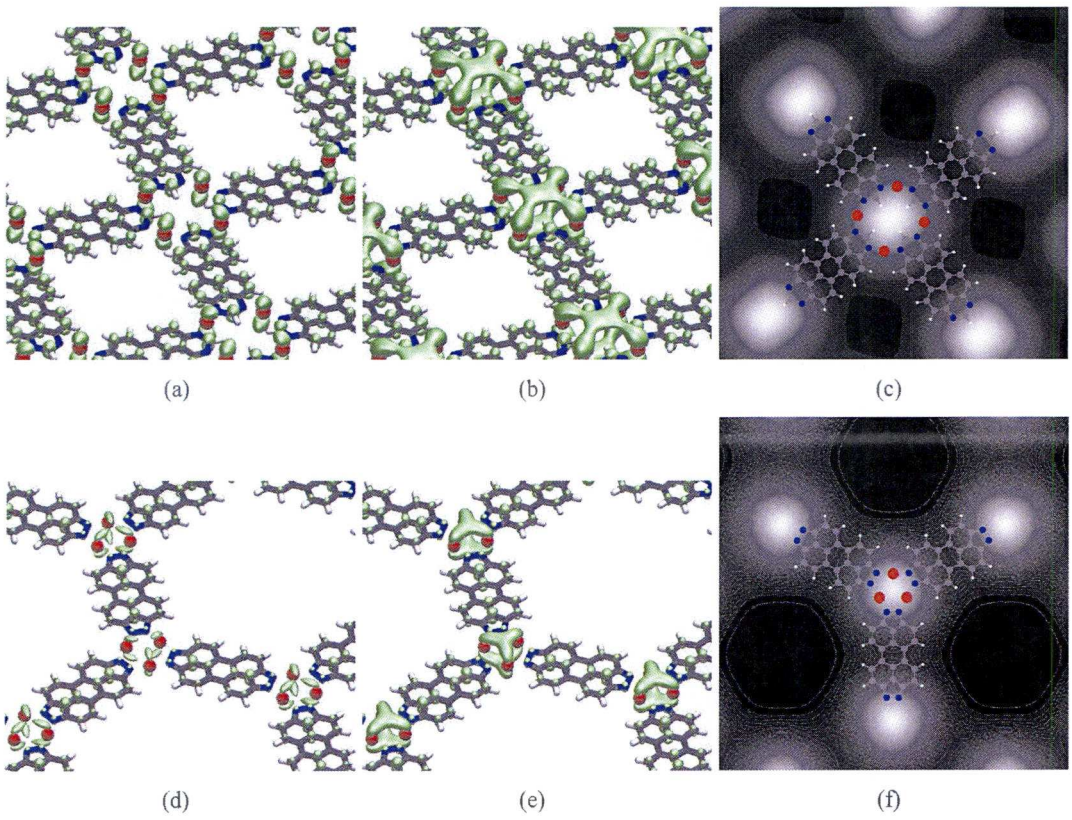

Figure 4.21: Visualisations of the band-decomposed electron densities of the states giving rise to the STM fingerprint for TAPP (a-c), Figure 4.18, and for DPDI (d-e), Figure 4.19. The surface contour plots (a,b,d,e) of the band-decomposed densities were produced at a value of -0.025 e Å^{-3} (a), -0.018 e Å^{-3} (b), -0.0088 e Å^{-3} (d), and -0.007 e Å^{-3} (e) The cross-sections (c,f) were made 5 Å above the (c) TAPP and (f) DPDI coordination networks covering an area of 4×4 nm^2. (c) is taken from [121].

4.4 Transformation of a porous network into covalently linked chains

The relatively low stability of the porous TAPP network, whose structure is destroyed at about 190°C, enables the formation of a new structure, namely oligo- and polymeric chains of TAPP molecules, which are formed around 250°C. The possibility to manipulate the chains with the STM tip without destroying their internal structure, along with the curved arrangement of some chains, provide support for covalently linked TAPP molecules [49]. The TAPP chains appear to have an arbitrary orientation on the Cu(111) surface. However, a statistical analysis of the observed directions of the chains with respect to the principal directions of Cu(111), revealed an influence of the substrate on the alignment of the chains. It was shown that a majority of the chains are aligned along the principle directions of the Cu(111) surface [61]. Thus, although the dominating interaction is provided by the covalent bonds between the molecules, the chains also have a strong preference to align with respect to the substrate.

From STM experiments the distance between TAPP monomers in the chains was deter-

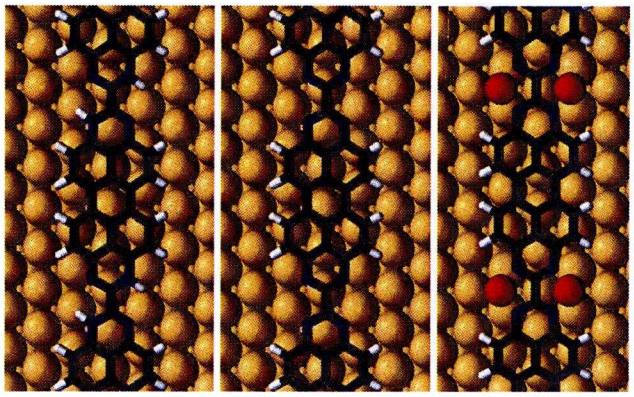

(a) poly(iso-TAPP) (b) poly(TAPP) (c) poly(TAPP-Cu)

Figure 4.22: Polymeric covalently linked chains consisting of (a) tautomerised TAPP molecules, (b) deprotonated TAPP molecules, and (c) deprotonated TAPP molecules with Cu adatoms coordinated to the nitrogen atoms.

mined to be (1.23 ± 0.12) nm. Using the experimental lattice constant of copper (3.610 Å) it is possible to construct a one-dimensional supercell commensurate with the copper substrate, where the Cu(111) surface unit cell has been repeated five times in the close-packed direction of the lattice, resulting in a supercell with the dimension of 1.28 nm. In the modelling of the chains a unit cell of p(5×8) was used which assumes commensurate chains along the principle axis of the lattice and ensures negligible interactions between chains in periodic images (the distance between neighbouring chains is larger than 11 Å).

4.4.1 Chemical nature of the chains

The first interpretation [49] of the chains assumed that they were formed through a tautomerisation of TAPP, illustrated in Figure 4.3. This model was also supported by simulated STM images of the tautomerised chain which resembled the experimental high resolution STM images of the chains very well. However, as will be shown, STM is not a suitable tool to determine the detailed structure of the chains as it is not able to distinguish between chains formed by different chemical bonds. Furthermore, XPS experiments reveal only one peak in the N1s spectrum of the chains, indicating that all nitrogen atoms experience the same chemical environment, and the interpretation of the chemical nature of the chains had to be re-considered.

Figure 4.22 shows three different types of chains considered, with the respective formation energies summarised in Table 4.6. It is found that the chain formed by dehydrogenation of TAPP, poly(TAPP), is energetically disfavoured. However, coordination of this chain to Cu adatoms, in a similar fashion to the porous network with one Cu adatom shared between two nitrogen atoms of adjacent molecules, stabilises the chain, with a reaction energy of -2.21 eV molecule^{-1}. This chain is referred to as poly(Cu-TAPP) and is even more stable than poly(iso-TAPP) formed by tautomerised molecules.

The nitrogen atoms of the three different chain structures poly(iso-TAPP), poly(TAPP) and

Table 4.6: Reaction energies of the three different types of chains illustrated in Figure 4.22.

Type of chain	Reaction energy (eV molecule^{-1})
poly(iso-TAPP)	-1.12
poly(TAPP)	+0.29
poly(Cu-TAPP)	-2.21

poly(Cu-TAPP) exhibit in each case different chemical environments and are therefore XPS should be able to differentiate between different models. The N1s chemical shifts of the chains with respect to the N1s core-level binding energy of the porous network were calculated in the final state approximation using two different methods to model the core-ionised systems: the Z+1 approximation, and a core-ionised PAW potential. Details on how the calculations of chemical shifts were done are given in Section 3.3. The results using the two methods are summarised in Table 4.7. Note that the trend of the core-level shifts is consistent between the two methods.

Table 4.7: Calculated chemical shifts of the N core level of poly(iso-TAPP), poly(TAPP) and poly(TAPP–Cu). Note that poly(iso-TAPP) has two types of nitrogen atoms with different chemical shifts. The shifts were calculated using the final state approximation using two different methods to model the core-ionised systems, as described in Section 3.3. The chemical shift from XPS experiments is -0.21 eV.

Type of chain		Z+1 (eV)	Core-ionised PAW (eV)
poly(iso-TAPP)	C=N-C	-0.43	-0.43
	C-NH-C	+1.71	+1.54
poly(TAPP)	C=N-C	-0.87	-0.82
poly(Cu-TAPP)	N-Cu	-0.23	-0.23

Figure 4.23 compares the simulated N1s core-level shifts of the different chains compared with the observed shift from XPS experiments. The simulated shift of poly(Cu-TAPP) gives an excellent agreement with the experiments, while the simulated chemical shifts of the other chains are not able to reproduce the experiments. Together with the reaction energies of the different chains, these results give the conclusive result that poly(Cu-TAPP) is the predominant structure of the chain.

Figure 4.24 depicts a comparison between an experimental high resolution STM image and the simulated LDOS of poly(taut-TAPP) and poly(Cu-TAPP). Although one might imagine that the structural differences between the two chains would make the chains distinguishable in STM, the simulated images for the two chains both reproduce very well the main features of the experimental image. Thus the suitability of STM in making conclusions about detailed structures is in this case very limited.

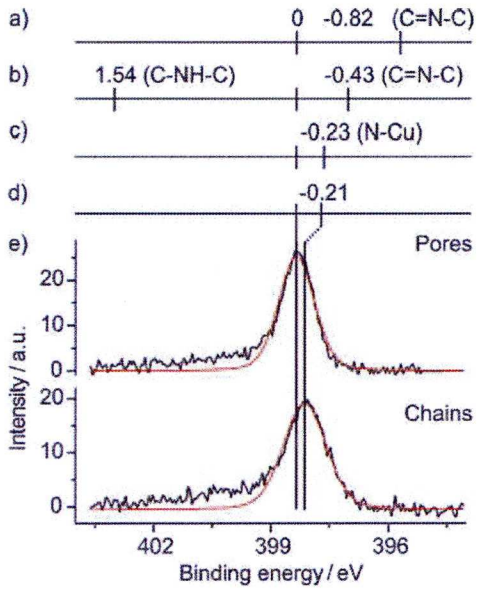

Figure 4.23: Calculated chemical shifts of the N1s core-level of a) poly(TAPP), b) poly(iso-TAPP) and c) poly(Cu-TAPP). d) Chemical shift of the chains obtained from the fits of the e) N1s spectra from XPS experiments of the chains shown in e). All chemical shifts are given with the N1s peak of the coordination network of TAPP as reference. From [61].

4.5 Effect of non-local dispersion forces

All the results presented up to here were obtained from semi-local DFT calculations, using a GGA XC-functional (PW91) which does not account for non-local correlation effects, generally known as van der Waals (vdW) interactions. In this section we aim to summarise the calculations which have been done to account for non-local dispersion interactions for the TAPP and DPDI systems. The main objective is to investigate how these interactions influence the structure of the different systems, but also any indirect effects on the electronic structure due to the corrected geometrical structure will also be discussed, such as core-level shifts, local density of states, molecular orbital projected density of states and Bader charges.

The calculations were carried out using the correction scheme by Grimme from 2006 [77] as well as the van der Waals density functional (vdW-DF) [11] which was implemented self-consistently by Jiri Klimes. The Grimme calculations were based on the PBE functional [10], while the vdW-DF correction was applied to the revPBE functional [88] as well as the PBE functional. The vdW-DF calculations based on the revPBE functional are referred to as revPBE-vdW and the ones based on PBE as PBE-vdW. Further details of how the calculations were performed are discussed in Sections A.1.1 and A.1.2 for the vdW-DF and Grimme corrections, respectively.

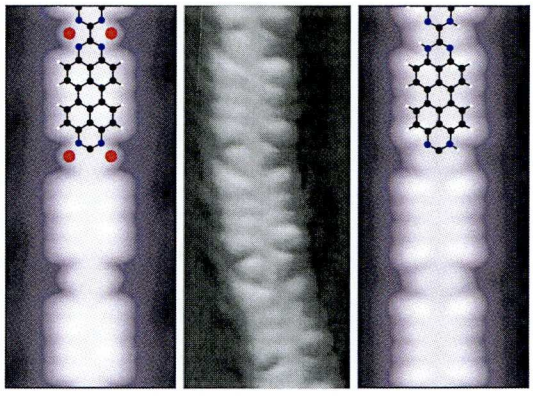

(a) (b) (c)

Figure 4.24: Simulated STM images of (a) poly(TAPP–Cu) and (c) poly(iso-TAPP). (b) Experimental constant current STM image at a sample bias of -0.6 V, which is well reproduced by the simulated images in (a) and (c). The simulated STM images show the local density of states integrated from the Fermi level to -0.6 eV, thus corresponding to a constant current image at -0.6 V. All images have the size 1.8×4 nm^2.

4.5.1 Isolated DPDI on Cu(111)

Structure and energies

For the isolated DPDI molecule on Cu(111) the investigated corrections to the dispersion problem was applied to the three most stable adsorption geometries found from the semi-local DFT calculations, illustrated in Figure A.1 (a), (d) and (e). The adsorption energies for the different corrections and adsorption geometries were calculated as

$$E_{\text{ads}} = E_{\text{DPDI/Cu(111)}} - \left(E_{\text{DPDI}} + E_{\text{Cu(111)}}\right), \tag{4.8}$$

where $E_{\text{DPDI/Cu(111)}}$ is the total energy of DPDI adsorbed on Cu(111), E_{DPDI} is the total energy of the DPDI molecule in vacuum and $E_{\text{Cu(111)}}$ is the total energy of the free Cu(111) surface. Note that the corrections have also been applied to the reference structures.

The general trend is that each vdW-correction contributes with a more or less constant term to the total adsorption energy, as shown in Table 4.8. Thus the trend of the adsorption energies is the same, irrespective of the employed vdW-correction. More specifically, each method predicts the same adsorption configuration to be the most stable one, namely (e), followed by configuration (d) which is found to be less stable by 10–20 meV throughout all methods. It is not possible to make conclusions about which method gives the best description of the magnitude of the adsorption energy since to date no experiments have been performed to estimate this quantity for the DPDI and TAPP systems. In the next paragraphs the structural changes imposed by the various corrections as well as their indirect influence on the core-level binding energies will be discussed.

Table 4.9 summarises the distances from the first surface layer of the carbon atoms and the two different nitrogen species of the isolated DPDI network in its most energetically favourable

Table 4.8: Adsorption energies of the three most stable structures of the isolated DPDI on Cu(111) (from semi-local DFT) when employing different corrections to account for the non-local dispersion interaction. The structures are illustrated in Figure A.1.

	Adsorption energy (eV)		
	Structure (a)	Structure (d)	Structure (e)
PW91 (no corr.)	-0.46	-0.52	-0.54
PBE-Grimme	-3.13	-3.34	-3.36
PBE-vdW	-2.49	-2.54	-2.56
revPBE-vdW	-1.55	-1.60	-1.61

adsorption site, illustrated in Figure 4.11, for the different corrections as well as the semi-local PW91 results.

The results without correction are in good agreement with the experimental XSW data considering the nitrogen atoms. As observed in XSW, the amine and imine nitrogen atoms adsorb at different heights above the surface. However, the imine nitrogen atoms are predicted at a slightly too large distance from the surface. Furthermore the average distance of the carbon atoms is far too large compared to the XSW data.

The conventional form of the vdW-DF based on the revPBE functional (revPBE-vdW) increases the error of the distances for both nitrogen and carbon atoms compared to the non-corrected PW91 calculations. In other words, revPBE-vdW is not a suitable choice for describing the structure of this type of system and will therefore be excluded from the study of the other systems. If vdW-DF is instead based on PBE exchange (PBE-vdW), the distances of the nitrogen atoms stay roughly the same as for PW91, and the carbon atoms move slightly closer to the surface. Hence, PBE-vdW corrects the adsorption height of the DPDI, although the error for the average height of the carbon atoms is still larger than 0.5 Å.

The best agreement with the experimental data is found for the Grimme correction. This semi-empirical scheme gives a perfect agreement with the XSW data for the imine nitrogens, while the amine nitrogens are adsorbed too close to the surface, almost at the same height as the imine nitrogens. Most remarkable is however the treatment of the perylene core, as the average height of the carbon atoms is almost within the error margin of the XSW measurements. The height of the carbon atoms are only slightly overestimated, and compared to the other methods the Grimme correction gives the best agreement with experimental results for this particular system.

Core-level shifts

Table 4.9 shows, in addition to adsorption heights, the effect on the core-level shifts, generated due to the structural geometrical difference imposed by the different vdW corrections, for the isolated DPDI molecules on Cu(111). The calculations were done using a core-ionised PAW potential for the core-ionised atom, and assuming that the difference in the non-local correlation energy is negligible between the neutral and the core-ionized state. Hence as before in this

Table 4.9: Core-level shifts of NH and NH_2 nitrogen atoms, and average heights above the first surface layer of the nitrogen atoms as well as carbon atoms in the isolated DPDI on the Cu(111) surface using indicated vdW-corrections. The core-level shifts are given with respect to the NH nitrogen in the PW91 geometry and for all geometries the shifts were calculated using the PW91 functional and a core-ionised PAW potential for the core-ionised atom as described in Section 3.3.

	Chemical shift (eV)		Distance to first Cu-layer (Å)		
	NH	NH_2	NH	NH_2	C-atoms
Experimental	0	1.82±0.11	2.20±0.03	2.40±0.11	2.68±0.06
PW91 (no correction)	0	1.86	2.31	2.42	3.36
PBE-Grimme	-0.06	1.79	2.20	2.22	2.61
PBE-vdW	-0.13	1.80	2.32	2.46	3.22
revPBE-vdW	-0.09	1.65	2.45	2.81	3.40

Table 4.10: Adsorption energies of the metal-organic coordination networks formed from either TAPP or DPDI molecules on the Cu(111) surface when employing different corrections to account for the non-local dispersion interaction. The structure of the TAPP network is illustrated in Figure 4.5 a and the structure of the DPDI network in Figure 4.12 b.

	Adsorption energy (eV molecule^{-1})	
	TAPP network	tridehydro-DPDI network
PW91 (no correction)	-2.40	-4.27
PBE-Grimme	-5.48	-7.18
PBE-vdW	-4.21	-5.98

thesis the PW91 XC-functional was used to evaluate the core-level shifts, but using the relaxed structural geometries given by the different corrections.

The calculated chemical shifts between the amine and imine nitrogen atoms were found to be within the error margin of the experiments for all the applied vdW-corrections.

4.5.2 TAPP and DPDI coordination networks

Structure and energies

For the porous networks formed from either TAPP or DPDI molecules, we used the structure found from semi-local DFT as the starting point for the PBE-Grimme and PBE-vdW calculations. The revPBE-vdW was excluded from this study due to its large errors for a single DPDI on Cu(111). The geometries of the TAPP and tridehydro-DPDI networks are illustrated in Figure 4.5 a and Figure 4.12 b, respectively.

The adsorption energies for the different corrections of the two networks are summarised in Table 4.10, together with the results from the non-corrected PW91 calculations. A similar trend as for the isolated DPDI on Cu(111): Each correction adds a more or less constant term, and the relative energy between different structures within each correction scheme follows the same trend as in the semi-local DFT calculation.

Table 4.11 summarises the heights of carbon and nitrogen atoms above the first surface

layer for the TAPP and tridehydro-DPDI networks. The results are compared to experimental XSW data. Both Grimme and PBE-vdW give close agreement with the experiments for the nitrogen atoms. These atoms pose no problem in semi-local DFT since the PW91 calculations are also in good agreement with the experiments. The carbon atom heights in the tridehydro-DPDI are also treated relatively well by the PW91 calculations. The error when applying either of the two correction schemes is about the same magnitude, but of opposite sign for the Grimme correction. For the TAPP network the carbon atoms are adsorbed more than 0.6 Å too far away from the surface when using PW91. In this case both the Grimme and PBE-vdW give a height within 0.15 Å from the experimental value.

The calculated core-level shifts for the network formed by DPDI molecules are also included in Table 4.11. The calculated shifts are given relative to the core-level binding energy of the NH nitrogen atom of the isolated DPDI on Cu(111), from the structure of respective correction scheme.

Table 4.11: Average heights of the nitrogen and carbon atoms of the porous TAPP and tridehydro-DPDI networks above the surface plane, when using different corrections to the GGA-DFT calculations. For the DPDI network also the simulated core-level shifts for the dispersion-corrected structures are given relative the core-level binding energy of the NH-nitrogen of the corresponding vdW-corrected structure of the isolated DPDI molecule on Cu(111). The experimental core-level shift is given relative to the low energy peak of the XPS experiments of the mobile (isolated DPDI) phase.

	Distance to first Cu-layer (Å)				Chemical shift
	TAPP		*tridehydro-DPDI*		*tridehydro-DPDI*
	N-atoms	C-atoms	N-atoms	C-atoms	N-atoms
Experimental	2.89	2.81	2.83 ± 0.03	3.00 ± 0.04	1.50 ± 0.10
PW91 (no corr.)	3.12	3.43	2.90	3.20	1.47, 1.52
PBE-Grimme	2.93	2.90	2.77	2.79	1.58, 1.64
PBE-vdW	2.73	2.95	2.94	3.21	1.72, 1.74

Effects on the coordinative bonding

The vdW interaction is a purely non-local phenomenon and does not contribute directly to the chemisorption bond of a molecule to a surface. However, this non-local dispersion interaction is necessary for chemisorption in systems where the attractive chemical interaction cannot overcome the Pauli repulsion between the molecule and substrate. One example is provided by the PTCDA molecule adsorbed on Ag(111) which only physisorbs in the GGA, but chemisorbs to the surface when vdW-interactions are included [71]. Hence although the van der Waals interaction does not have a covalent character, this interaction can allow a molecule to come closer to the substrate, into a regime where short-range chemical interactions take place.

In the case of our metal-organic coordination networks these interactions are not essential for the formation of chemisorption bonds between organic ligands and adatoms. However, the strength of the chemical interaction and hence of the coordinative bonding is still sensitive to

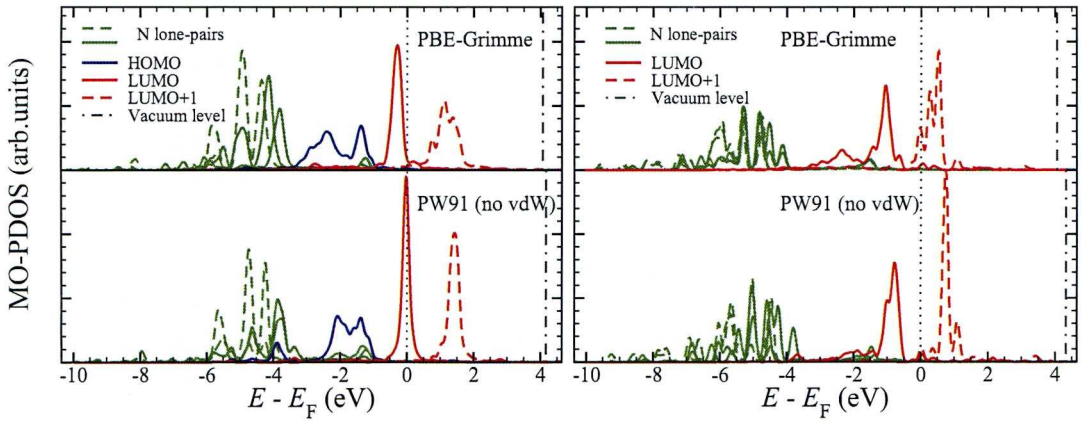

Figure 4.25: PDOS projected onto the molecular orbitals of (a) TAPP and (b) DPDI for respective porous network. The PDOS was calculated both for the structures determined by semi-local DFT (PW91) and by the Grimme corrected calculations (PBE-Grimme).

the vdW-interactions. Figure 4.25 illustrates how the molecular orbitals are affected for both the TAPP and DPDI honeycomb networks due to the structural changes imposed by non-local dispersion forces as described by the Grimme correction.

For the TAPP network both the LUMO and the nitrogen lone-pair orbitals are shifted down by 0.3 eV in average relative to the Fermi level. As concluded in Section 4.2.4 the effect on these orbitals defines the coordinative bonding, and hence the chemical bonding is slightly strengthen by the non-local vdW-interactions. Notably the energy level of the HOMO is not sensitive to the vdW-interactions.

In the case of the tridehydro-DPDI network all of the frontier orbitals are shifted down in energy by around 0.4 eV, except for the orbitals associated with the nitrogen lone-pairs, which are only shifted down by 0.2 eV. The rigid shift of the molecular orbitals of tridehydro-DPDI is probably due to an electrostatic effect, since also the vacuum level is shifted down by 0.3 eV (compared to 0.1 eV for the TAPP network). The reason why the nitrogen lone-pair orbitals are less shifted than other orbitals may be because they are shared with the Cu adatoms. Therefore, these orbitals do not share the reference level with the other molecular orbitals, which is the vacuum level, but rather the reference level of the metal substrate, which is the Fermi level.

4.5.3 Discussion

In Figure 4.26 the calculated adsorption heights using the different vdW-corrections are compared to the data from XSW experiments. Considering the nitrogen atoms both PBE-Grimme and PBE-vdW give adsorption heights that agree well with the experimental observations. Also the PW91 calculations without any correction work well in describing the height, in most cases better than the correction schemes. Only for the porous TAPP network do the PW91 results give a considerably larger adsorption height for the nitrogen atoms.

For the carbon atoms PW91 works much more poorly in predicting the adsorption height

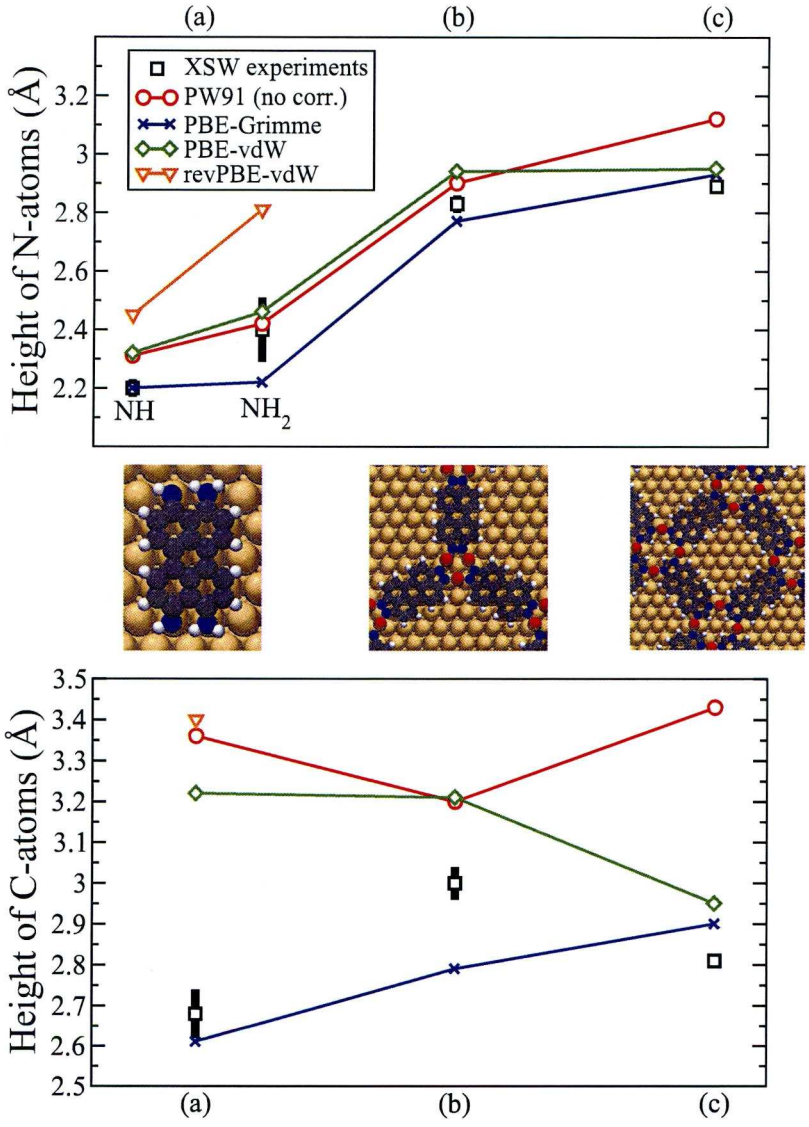

Figure 4.26: The heights of the nitrogen atoms (top) and carbon atoms (bottom) for (a) the single DPDI molecule, (b) the tridehydro-DPDI honeycomb network, and (c) the porous TAPP network, using the different vdW-corrections, indicated in the legend. The calculated data are compared to data from XSW experiments. Note that for the single DPDI molecule the heights of the two different types of nitrogen atoms are shown and for the carbon atoms the average heights above the Cu(111) surface are given.

than for the nitrogen atoms. It is only for the tridehydro-DPDI network it gives a deviation from experiments which is less than 0.3 Å while for both the TAPP network and the adsorption of a single DPDI molecules it gives a deviation larger than 0.6 Å. The PBE-vdW calculations gives a reasonable description of the two coordination networks, but fails dramatically for the more closely bonded single DPDI molecule. The PBE-Grimme calculations, on the other hand, gives a very good description of the adsorption height both for the TAPP network and the isolated DPDI molecule, although the adsorption height for the DPDI network is slightly too small. An interesting observation is that the DPDI network for which Grimme overcorrects is the structure for which the semi-local PW91 calculations give the best agreement with experiments. Note that the revPBE-vdW calculations were only performed for the single DPDI molecule, for which it gives too large heights for both nitrogen and carbon atoms. We can expect this to be the general case, since revPBE-vdW will always give larger separations than PBE-vdW since the exchange part of the revPBE functional is more repulsive than the exchange part of the PBE functional.

Summarising the results of the adsorption heights it is obvious that PBE with the Grimme correction gives the overall best performance of the tested methods for our perylene derivatives on Cu(111). Hence, if one desires to describe adsorption geometries in this type of systems this correction is a fairly good choice and will improve the adsorption height compared to semi-local DFT. The question is also whether the Grimme correction (or any vdW-correction) can be used to compare the energetics of different systems. For the studied systems no experimental reference exists for the binding energies, although it has been shown [122] that the Grimme correction overestimates binding energies for molecules adsorbed on metals.

Although the absolute binding energies given by the Grimme may be too large, our results do suggest that it is possible to compare the energies within this correction. From Table 4.8 comparing the adsorption energies for an isolated DPDI molecule on Cu(111) it was shown that the trend of the binding energies for the different corrections follows closely the trend of the binding energies given by the semi-local PW91 calculations.

Our results suggest that for molecules that are partly chemisorbed to a surface, as our perylene derivatives, the energy difference between adsorption sites originates mainly from the chemisorption interactions and it is sufficient to compare energies of different sites using semi-local DFT. It is necessary to include the dispersion forces only to correct the structure for the most stable adsorption configuration(s).

Although we find that the Grimme correction scheme works fine for our systems this is not necessarily transferable to other systems. This benchmark has to be extended not only to different systems, but also future studies applying different correction schemes to the vdW-interactions are necessary. For example the C_6-scheme by Tkatchenko and Scheffler [79] is one possible option, but also an updated version of the vdW-DF has recently become available [123].

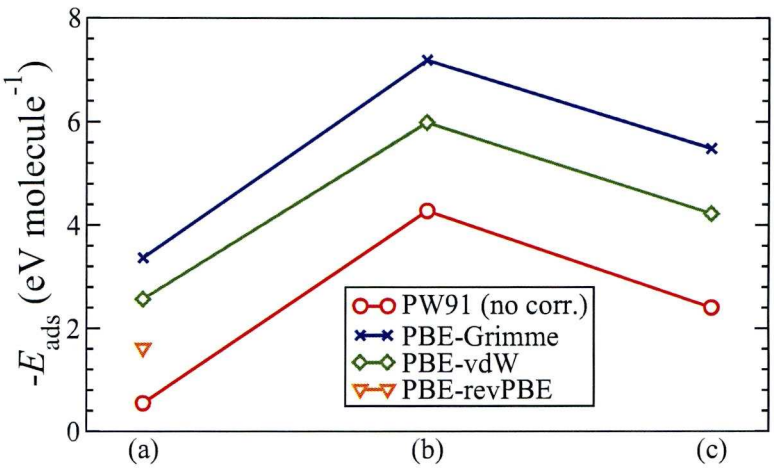

Figure 4.27: Summary of adsorption energies for (a) the single DPDI molecule, (b) the tridehydro-DPDI honeycomb network, and (c) the porous TAPP network, using different vdW-corrections as indicated in the legend.

4.6 Summary

In this chapter the structure and bonding in the porous surface networks formed by either the TAPP or DPDI molecule on the Cu(111) have been discussed and compared. It was shown that both networks are stabilised by copper adatoms coordinated to the nitrogen atoms of the molecules. Furthermore, the formation of the porous network from DPDI molecules is driven by a complete dehydrogenation of the nitrogen atoms, resulting in a network consisting of tridehydro-DPDI molecules.

Experimentally it has been observed that the tridehydro-DPDI network has a greater thermal stability compared to the TAPP network. The difference in stability between the two networks is partly due to the different strength of the coordination bonds in the networks. In the tridehydro-DPDI network the LUMO of the tridehydro-DPDI molecules is completely filled well below the Fermi level of the substrate, while the LUMO of the molecules in the TAPP network is only partly occupied in semi-local DFT but becomes fully occupied in the vdW-corrected structure. Furthermore, the lowering of the nitrogen lone-pair orbitals is greater for the tridehydro-DPDI network than for the TAPP network. Furthermore, it was investigated how close the commensurate network structures are to those of the free isolated coordination networks. It was found that the commensurate surface unit cell of the tridehydro-DPDI surface network is closer to the optimised unit cell of the isolated network, compared to the TAPP network.

It is possible to identify the copper adatoms indirectly in STM due to the interaction with the organic ligands in both the TAPP and tridehydro-DPDI porous networks. The metal-ligand interactions give rise to an unoccupied electronic state which is observable as a resonance in bias-dependent STM imaging. The fact that this electronic state is observed experimentally in STM, gives further evidence for the adatom-supported structures.

The polymeric chains formed from TAPP molecules consist of deprotonated TAPP molecules and not tautomerised ones which was the original interpretation. Furthermore, as for the TAPP porous network the chains are coordinated to copper adatoms, which is supported by XPS experiments and simulated core-level shifts.

Finally, it has been illustrated how non-local dispersion forces influence the structure of a single DPDI molecule as well as the tridehydro-DPDI and TAPP networks. It was shown that the semi-local Grimme gives the overall best description of the different structures. Furthermore it was shown that the energetic ordering of chemisorbed molecules is not changed by the van der Waals correction, but only the absolute adsorption energies. Finally, the structural differences induced by van der Waals interactions have some influence on the molecular orbitals of the molecules, slightly strengthening the coordination bond in the case of the TAPP network, and rigidly shifting all frontier orbitals down in energy for tridehydro-DPDI.

Chapter 5

An organic paramagnet on Cu(110)

In the previous chapter the structural stabilities and electronic properties of two porous metal-organic coordination networks were discussed. These networks were designed partly because of their properties to host smaller functionalised guest molecules. Here we will have a look at a possible candidate of such a functionalised guest molecule, namely the adsorption of a free radical on a metallic substrate. It will be shown from our combined theoretical and experimental study that the organic molecule retains its paramagnetic properties upon adsorption on the paramagnetic Cu(110) surface. This work was done in collaboration with the experimental group of Prof. Rasmita Raval at University of Liverpool.

5.1 2,2,5,5-tetramethyl-3-carboxypyrrolidine nitroxide (3-CP)

The 2,2,5,5-tetramethyl-3carboxypyrrolidine nitroxide (3-CP) molecule is a free radical due to the un-paired spin centred on the NO-group, making the molecule paramagnetic in the gas-phase. The molecule, whose structure is shown in Figure 5.1, is tailored with four methyl groups protecting the NO moiety from interacting with other molecules. Furthermore, it is designed with a carboxylic acid group that can interact with other molecules or, as will be shown here, de-protonate and bond to the Cu(110) surface.

5.2 Elucidation of the adsorption geometry

5.2.1 Adsorption configurations

To obtain information on the orientation and adsorption site of the 3CP molecule on Cu(110) a number of different adsorption sites were investigated. The most stable of the adsorption sites investigated are illustrated in Figure 5.2. Note that for the structures (c-e) in Figure 5.2 the 3CP molecule is deprotonated, while for the structures (c-e) in Figure 5.2 the molecule stays intact. For the intact adsorption, (structure (a) and (b)), the adsorption energy was defined as

$$E_{\text{ads}}^{\text{intact}} = E_{\text{3CP/Cu}} - [E_{\text{3CP}} + E_{\text{Cu}}], \tag{5.1}$$

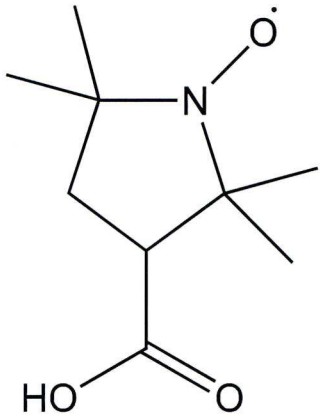

Figure 5.1: Schematics of the 3CP molecule.

and in the case of the deprotonated adsorption as

$$E_{\text{ads}}^{\text{deprot}} = E_{\text{3CP/Cu}} + E_{\text{H/Cu}} - [E_{\text{3CP}} + 2E_{\text{Cu}}], \tag{5.2}$$

where $E_{\text{3CP/Cu}}$ is the total energy of the molecule adsorbed on Cu(110), E_{3CP} the total energy of the structurally optimised free 3CP molecule, E_{Cu} the total energy of the optimised bare Cu(110) slab, and $E_{\text{H/Cu}}$ the total energy of atomic hydrogen adsorbed on Cu(110). Note that a negative value of the adsorption energy indicates a stabilisation compared to the reference systems.

The results, summarised in Table 5.1, show a strong preference for the molecule to deprotonate and bond with the resulting carboxylate group to the short bridge site, Figure 5.2 (a), which has an adsorption energy of -1.31 eV. However, the deprotonation of the molecule will only occur at activated temperatures to overcome the energy barrier for deprotonation. If the molecule instead stays intact upon adsorption to the surface, the adsorption with the NO-group to the short bridge, Figure 5.2 (c), is the most energetically favourable adsorption site, which has an adsorption energy of -0.72 eV. It is also possible for the intact 3CP molecule to adsorb with the carboxylic acid group to the surface, but this is much weaker compared to adsorption with the NO group to the surface.

Since the deprotonation is an activated process, it is not possible to make predictions of whether the 3CP molecule adsorbs with the NO group to the surface, or with the NO group pointing away from the surface as a result of a deprotonated 3CP molecule bonding with the carboxylate group to the surface from consideration of the adsorption energy alone. It is known from literature [124, 125] that carboxylic acid groups deprotonate at elevated temperatures on the Cu(110) surface. For example benzoic acid has been found to deprotonate in the temperature range 119–175 K [124] and formic acid has been found to deprotonate around 270 K [125]. However, although literature seems to suggest a deprotonation, we need additional data to support this hypothesis for our system. To gain more information of the bonding configurations we performed calculations of IR spectra that were compared with the experiments.

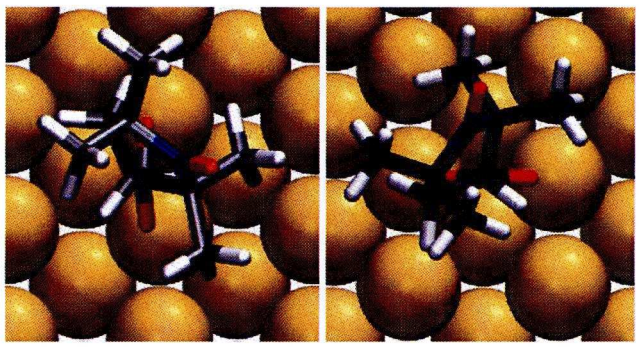

(a) COO^- to short bridge (b) COO^- to long bridge

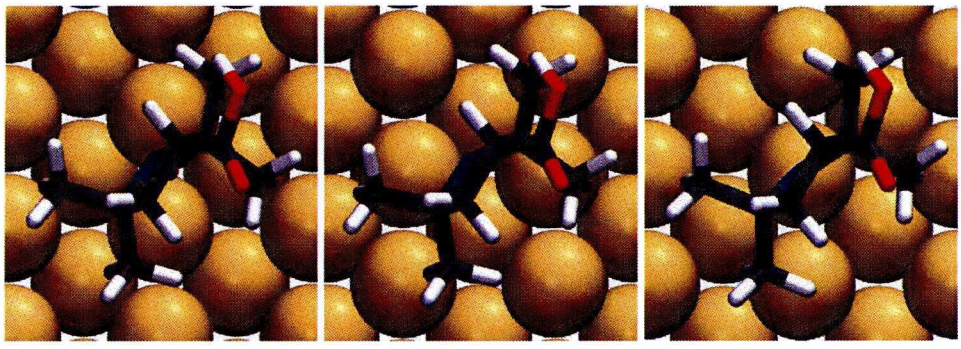

(c) NO to short bridge (d) NO to long bridge (e) NO to top

Figure 5.2: The most stable adsorption configurations found for the 3CP molecule on the Cu(110) surface with the (carboxylate group (a,b) adsorbed to either the short bridge (a) or the long bridge (b) site of the surface, and with the NO group (c-e) adsobed to either the short bridge (c), the long bridge (d) or the top (e) site of the surface. In structure (a) and (b) the carboxylic acis group of the 3CP molecule has deprotonated and the molecule is anchored with the resulting carboxylate group to the surface.

Table 5.1: Calculated adsorption energies of the 3CP molecule adsorbed on Cu(110). For the two "radical up" adsorption sites the molecule was deprotonated and the adsorption energy was calculated using Eq. (5.2) while for the three "radical down" adsorption sites the molecule was assumed to stay intact and the adsorption energy was calculated using Eq. (5.1). Note that the more negative is the value of the adsorption energy, the more energetically stable is the adsorption.

	Adsorption site	Adsorption energy (eV)
Radical up, Figure 5.2(a,b)		
(a)	COO^- on short bridge	-1.31
(b)	COO^- on long bridge	-1.22
Radical down, Figure 5.2(c-e)		
(c)	NO on short bridge	-0.72
(d)	NO on long bridge	-0.47
(e)	NO on top	-0.35

5.2.2 Infrared spectroscopy

Infrared spectra and intensities were calculated within the framwork of the harmonic approximation, as described in Section 3.2. Figure 5.3 depicts a comparison between the room-temperature RAIR spectrum and the two simulated spectra, with 3CP adsorbed either with the carboxylate group (de-protonated molecule) or the NO-group (intact molecule) to the Cu(110) surface. The agreement between the measured spectrum and the spectrum of the 3CP molecule adsorbed with the carboxylate group, as shown in Figure 5.2 (a), agrees well in the fingerprint region, 1000–1800 cm^{-1}. In particular the dominant peak at 1396 cm^{-1} in experiments is found at 1408 cm^{-1} in the calculations. The smaller, but still significant, peaks at 1450 cm^{-1} and 1134 cm^{-1} in the experimental spectrum is found at 1468 cm^{-1} and 1136 cm^{-1}, respectively, in the simulated spectrum. Furthermore, the peak at 1345 cm^{-1} in the simulated spectrum can be seen as a shoulder of the experimental 1396 cm^{-1} peak. The largest discrepancy between the simulated spectrum of the deprotonated molecule adsorbed with the carboxylate group to the surface (radical up) and the experimental room temperature spectrum is the high frequency region ($\sim$3000 cm^{-1}), which appears to be almost absent in the simulated spectrum. The reason for this discrepancy is explained below. Furthermore, a small peak is observed in experiments at 831 cm^{-1}, which could not be explained from the simulated spectrum.

The simulated spectrum with the intact 3CP molecule adsorbed with the NO group to the short bridge site, Figure 5.2 (c), does not reproduce the RAIR spectrum, Figure 5.2 (a). In the simulated spectrum there is no prominent peak at $\sim$1400 cm^{-1}, but instead at 1776 cm^{-1} due to the C=0 stretch, which is not observed experimentally. It is worth noting that a prominent peak in the region 1700–1800 cm^{-1} is observed experimentally at temperatures well below room temperature. However, at room temperature our combined theoretical and experimental analysis gives strong indication that the 3CP molecule deprotonates and bonds with the carboxylate group preferably to the short bridge site of the Cu(110) surface.

Enhancement of the calculated infrared intensity in the fingerprint region

Despite that the fingerprint region of the simulated spectrum of the deprotonated 3CP molecule being adsorbed with the carboxylate group to the Cu(110) surface correlates well between the experimental room temperature, it appears that the infrared intensities of the high frequency modes ($\sim$3000 cm^{-1}) are too weak in the simulated spectrum. However, this appearance is rather due to an enhancement of the calculated infrared intensities in the fingerprint region. This can be shown by comparing the calculated intensities in this spectrum with the calculated intensities in the high frequency region of the calculated spectrum with the NO group anchored to the surface, Figure 5.3 (c). In the latter spectrum, the relative intensities between high frequency and fingerprint region compares better with the measured spectrum in Figure 5.3 (a). At the same time the intensities of the high frequency regions of the two simulated spectra are of the same order of magnitude. Hence the normal modes intensities of the fingerprint region are overestimated in Figure 5.3b.

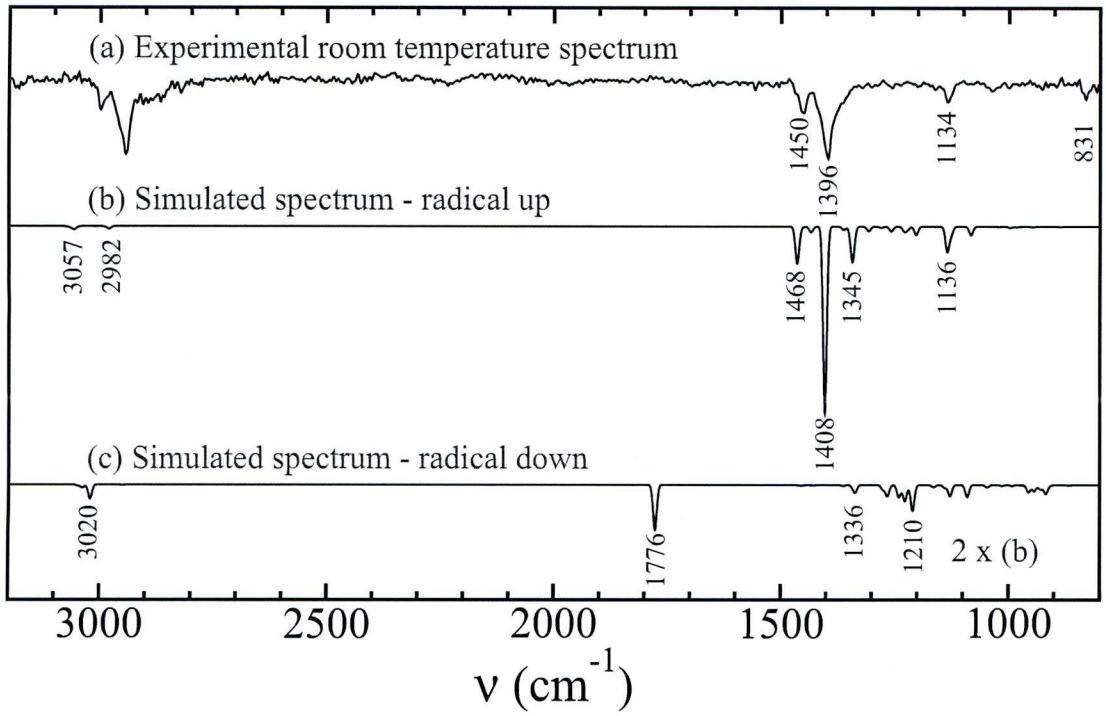

Figure 5.3: (a) Experimental RAIR spectrum of 3CP/Cu(110) taken at room temperature. Simulated spectra of (b) the deprotonated 3CP molecule adsorbed with the resulting carboxylate group to the short bridge of Cu(110) and (c) the intact 3CP molecule adsorbed with the NO-radical to the short bridge of Cu(110). The intensities of the peaks in (c) have been scaled twice with respect to the intensity of the peaks in (b). The intensities between the experimental and theoretical spectra are not directly related to each other. Assignment of the peaks is found in Table 5.2

Table 5.2: Peak assignment of the main peaks in the simulated IR-spectra in Figure 5.3 (b) and (c).

Spectrum in Figure 5.3 (b)

Frequencies (cm^{-1})	Assignment
1050–1250	Ring deformations, skeletal C-$(CH_3)_2$
1345	ν(NO), ν_s(COO), $\delta_s(CH_3)$
1408	ν(NO), ν_s(COO)
1468	$\delta_{as}(CH_3)$, $\delta_{as}(CH_2)$
2982	$\nu_s(CH_3)$
3057	$\nu_{as}(CH_3)$, $\nu_{as}(CH_2)$

Spectrum in Figure 5.3 (c)

Frequencies (cm^{-1})	Assignment
910–960	Ring deformations
1040–1340	ν(C-O), δ(OH), $\delta(CH_x)$, ring deformations
1776	ν(C=O)
3020	$\nu_{as}(CH_3)$, $\nu_s(CH_2)$

This enhancement is attributed to an artefact of DFT arising from the electron delocalisation (or derivative discontinuity) problem of DFT [126] which results in the localised $2\pi^*$-orbital being fractionally charged for the deprotonated molecule adsorbed on the surface. Small displacements of the NO-group results in that the fractionally charged $2\pi^*$-orbital change its occupancy, with the Cu-substrate acting as electron donor or acceptor. The dynamical dipole moment induced by the NO-group is therefore overestimated and vibrational modes with contributions from this group will hence have too large intensity in the calculated infrared spectra. The reason for the infrared intensities of the fingerprint region not being enhanced in the spectrum in Figure 5.3c is that the NO group has no fractional occupation.

5.3 Survival of the unpaired spin upon adsorption

In previous sections we have shown that upon adsorption on the Cu(110) surface at elevated temperatures the 3CP molecule deprotonates and bonds with the resulting carboxylate group with preference to the short bridge site of the Cu(110) surface, illustrated in Figure 5.2. In this adsorption geometry the NO group is almost perpendicular to the surface, however, it remains to show whether the unpaired spin on the NO group survives the adsorption or not, in other words, whether the 3CP molecule is still a radical once adsorbed on the Cu(110) surface.

5.3.1 Spin-polarised electron density

The first indication of what happens to the unpaired electron upon adsorption of the 3CP molecule in its most stable adsorption configuration was obtained from the calculated spin-polarised electron density, $\rho_{\uparrow-\downarrow}$. The spin-polarised electron density is defined as

$$\rho_{\uparrow-\downarrow}(\mathbf{r}) \equiv \rho_{\uparrow}(\mathbf{r}) - \rho_{\downarrow}(\mathbf{r}), \tag{5.3}$$

where $\rho_{\uparrow}$ is the electron density of electrons with spin up and $\rho_{\downarrow}$ is the electron density of electrons with spin down. In Figure 5.4 the spin-polarised electron density is visualised as surface contour plots, for both the isolated (intact) and adsorbed 3CP molecule. In both plots the value of the contours is chosen to be -0.1 e, to illustrate how much the unpaired electron is affected by the deprotonation and adsorption. The differences between the contours of the two molecules are only minor giving a first qualitative indication that the unpaired electron stays localised upon adsorption of the 3CP molecule on the Cu(110) surface.

5.3.2 Partial density of states

The second indication that the un-paired electron survives comes from the calculated partial density of states. The partial density of states of an atom is calculated as a projection of the Kohn-Sham orbitals of the total system onto spherical harmonics centred on the atom and integrated over an atomic sphere. Figure 5.5 shows the partial density of states calculated for the NO group both for the isolated (intact) 3CP molecule and deprotonated 3CP molecule

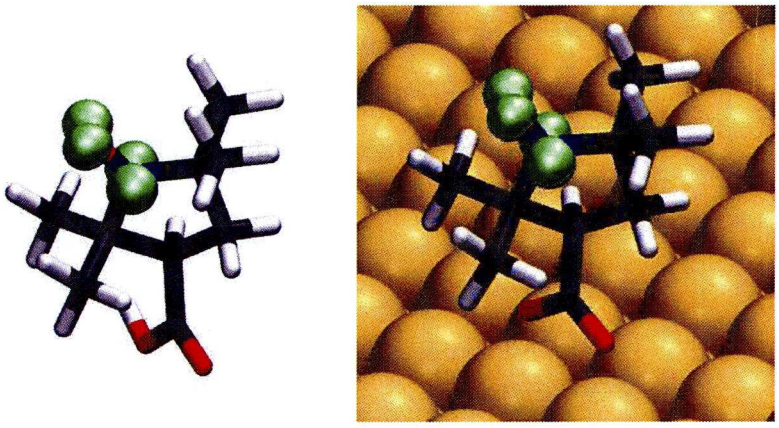

(a) (b)

Figure 5.4: Visualisation of the spin-polarised electron density as defined Eq. (5.3). The surface plots in green illustrates the spin-polarised density at a contour value of -0.1 e for the isolated 3CP molecule (a) and the deprotonated 3CP molecule adsorbed with the carboxylate group to the short bridge site (b).

adsorbed in its most stable adsorption configuration. The vacuum levels are aligned for the two systems.

The plots of the partial density of states in Figure 5.5 show that the electronic states centred on the NO-group are not much affected by the deprotonation and adsorption of the 3CP molecule on the surface. There is a minor rigid shift of all states with respect to the vacuum level, but apart from this no differences are found between the isolated and the adsorbed molecule, hence the NO-group is hardly affected at all by the adsorption. However, the $2\pi^*$-orbital, which gives rise to the spin-polarisation of the molecule, is only fractionallly charged for the adsorbed deprotonated molecule. This means that, in our calculations, the adsorbed molecule has a smaller spin-polarisation than the molecule in vacuum. The fractional charge is explained by the derivative discontinuity problem of DFT [126]. Furthermore, this fractional occupation is responsible for the increase of the peaks in the fingerprint region of the calculated IR-spectrum for this system, as discussed in Section 5.2.2.

5.4 Summary

The organic 3-Carboxy Proxyl (3-CP) molecule is a radical and paramagnetic because of its unpaired electron in the NO group. The NO group is surrounded by methyl groups, which prevent this radical from interacting with other molecules. Experiments using STM and infrared vibrational spectroscopy suggest that when bonding to the copper (1 1 0) surface at room temperature, the molecule deprotonates and bonds to the surface via the resulting carboxylate group. This bonding geometry leaves the NO-group unperturbed and indicates that the unpaired electron in the NO group survives on the surface.

The proposed nature of bonding of the molecule with the surface is corroborated from den-

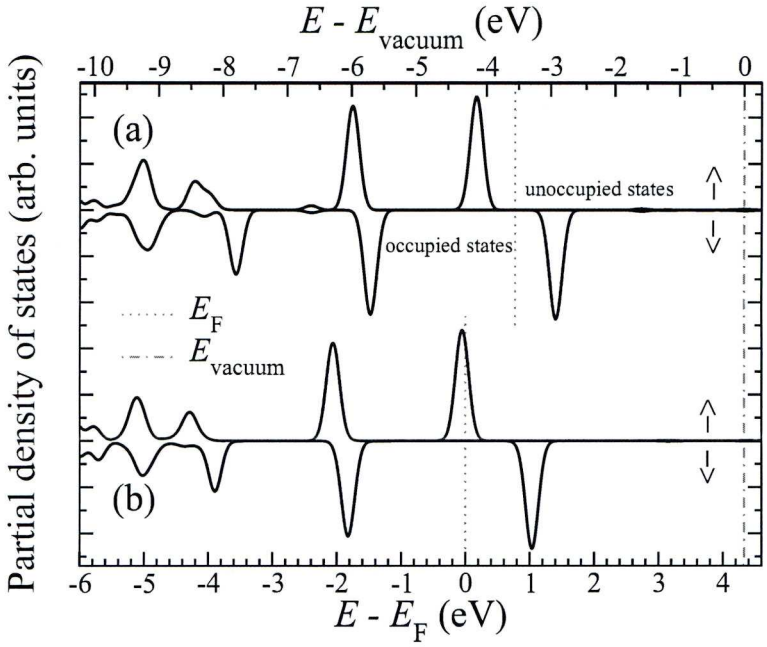

Figure 5.5: Spin-polarised partial density of states of the π-orbitals, showing the spin up ($\uparrow$) and spin down ($\downarrow$) contributions summed over the atoms in the NO-group for the isolated 3CP molecule (a) and the deprotonated 3CP molecule adsorbed with the carboxylate group to the short bridge site (b). The vacuum level of the two systems have been aligned and for the isolated molecule (a) the Fermi level was defined as the middle between the single highest occupied molecular orbital and the first unoccupied molecular orbital of the molecule.

sity functional calculations of the electronic structure and bonding geometry. The calculated IR spectra of the lowest energy structure are in good agreement with experimental spectra. The calculated spin-polarized charge density together with the partial density of states suggest that the un-paired spin in the NO-group survives upon adsorption of the molecule on the surface. Further experimental studies are needed to verify this theoretical prediction about the survival of the unpaired spin of the 3CP molecule upon adsorption on the Cu(110) surface, such as spin-polarised scanning tunnelling spectroscopy experiments.

Chapter 6

Polycyclic aromatic hydrocarbons on graphene

In this chapter, different methods for including the missing long-range dispersion term in semi-local DFT are benchmarked for twelve different polycyclic aromatic hydrocarbons (PAHs) adsorbed on graphene. These methods include the van der Waals density functional (vdW-DF) described in subsection 2.2.3, as well as the different semi-local C_6-correction schemes described in subsection 2.2.4. Results obtained from popular force-field methods are also included in the benchmark, and the theoretical results are compared to temperature programmed desorption experiments from literature [127]. Furthermore the role of the dispersive versus electrostatic Coulomb forces is investigated by a decomposition of the total interaction energy for a selection of PAHs. The calculations using the semi-local C_6-corrections as well as the revPBE energy decomposition were performed by Felix Hanke at the University of Liverpool, and the force-field calculations were carried out by Carlos-Andres Palma in Paolo Samori's group at the University of Strasbourg. The computational details for the work performed in this chapter are summarised in Subsection C.1.1 for the DFT calculations and in Subsection C.1.2 for the force-fields calculations.

6.1 Adsorption of PAHs on graphene

6.1.1 System setup and binding energy curves

For all molecules considered in this study it was assumed that a weak physisorption of a PAH on graphene does not affect the intramolecular geometry of either the PAH or the graphene. Similar to the stacking order in graphite and in bilayer graphene, the lowest-energy configuration for benzene adsorption was found to be the AB-type stacking, which was then used for the aromatic hydrocarbons throughout. This geometry is illustrated for the case of adsorbed hexabenzocoronene in Figure 6.1. Note that if one considers only nearest neighbour interactions any PAH molecule has two kinds of sp^2 carbon atoms: One type adjacent to three other carbons atoms and the second type with two carbon neighbours and one hydrogen neighbour.

For each PAH a binding energy curve was obtained by calculating the total energy at dif-

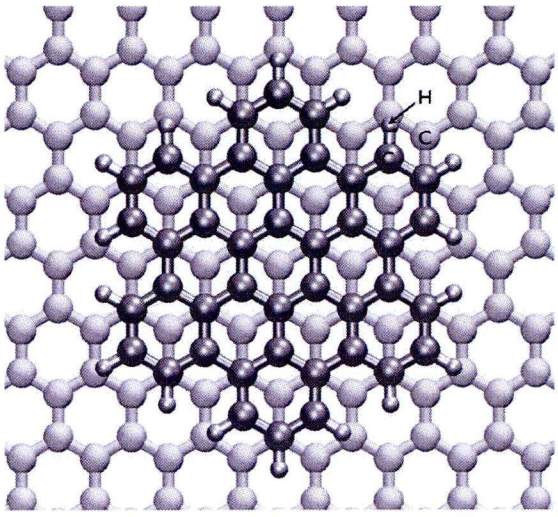

Figure 6.1: Lateral configuration of the AB stacking of hexabenzocoronene ($C_{42}H_{18}$) on a graphene sheet.

ferent heights of the molecule above the graphene plane with respect to the total energy of the molecules at a reference height as

$$E_{\text{tot}}(h) = E(h) - E(h_{\text{ref}}). \tag{6.1}$$

h_{ref} was chosen at a height where the interactions between the PAH and graphene can be neglected. A value of $h_{ref} = 14.0$ Å was used throughout the study. The equilibrium heights h_0 were determined as the height where the binding energy curve has a minimum:

$$\left.\frac{dE_{\text{tot}}}{dh}\right|_{h=h_0} = 0. \tag{6.2}$$

The total binding energy was determined by

$$E_{\text{bind}} = -E_{\text{tot}}(h_0). \tag{6.3}$$

Note that a negative value of the total energy indicates a stabilisation with respect to the reference system, while the binding energy is given as a positive quantity. In practice the height h_0 was determined by sampling the total energy around the equilibrium height until the height was determined within a numerical precision of ± 0.01 Å.

In Figure 6.2 the binding energy curves of the graphene dimer (a) and benzene on graphene (b) are illustrated for the different vdW corrections to DFT and the force-field methods. Also the values from semi-local DFT using the PBE and revPBE flavours of GGA are included in the comparison. Without any vdW correction these GGAs give virtually no bonding. The binding energies and heights of all the investigated PAHs for the different methods are summarised in Table C.1-C.4.

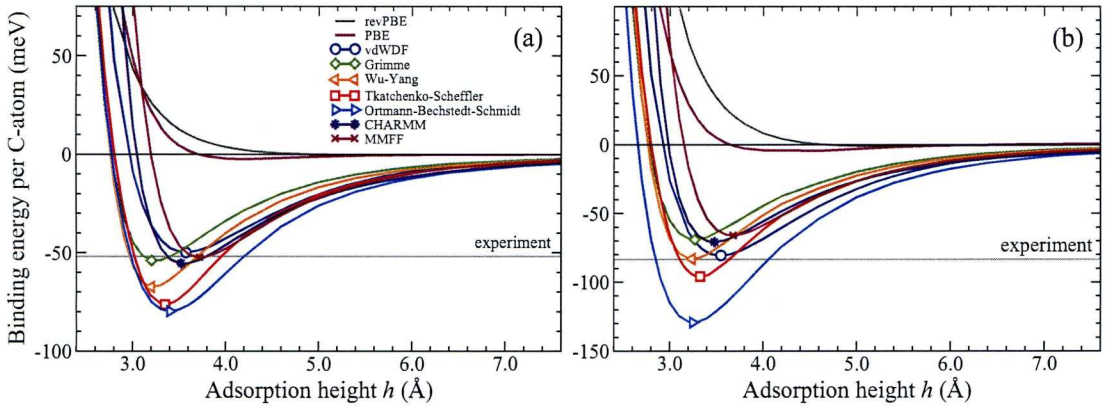

Figure 6.2: Potential energy curves of (a) graphene and (b) benzene adsorbed on graphene using different vdW corrections as indicated in the legend, and using the PBE and revPBE XC-functionals without correction. The experimental binding energies are taken from [127], which for graphene were obtained by an extrapolation of the measured binding energies of a series of PAHs.

6.1.2 Parametrisation of the binding energy

Figure 6.3 compares the binding energies as a function of the hydrogen to carbon ratio, N_H/N_C, for the twelve PAHs adsorbed on graphene. Also the experimental values of the binding energy for benzene, naphtalene, coronene and ovalene on graphite are shown, which were obtained from temperature programmed desorption (TPD) experiments by Zacharia and coworkers [127]. The binding energy of the bilayer of graphene is also shown in Figure 6.3. It should be noted that this value is not a direct experimental value but was obtained in Ref. [127] by an extrapolation of the binding energies of the other four adsorbates using the MM3 force-field [128].

Our results indicate that the first-principles vdW-DF method gives the best agreement with the data obtained from the TPD experiments with the lowest mean absolute error (MAE) of 6.1 meV/atom, see Table 6.1. Also the Wu-Yang scheme gives good agreement with the experimental data with a MAE of 7.7 meV/atom. The MAEs were calculated without taking the experimentally extrapolated binding energy of graphene into account. Including this value the vdW-DF gives the exclusively best agreement with experiments. Note that the data given by the OBS scheme could not be fitted into Figure 6.3.

The binding energy normalised per number of carbon atoms follows a linear trend with respect to the hydrogen-to-carbon ratio N_H/N_C for all models. The binding energy per carbon atom can hence be expressed as

$$E_{ads}/N_C = E_{CC} + (E_{CH} - E_{CC})\,\frac{N_H}{N_C}. \tag{6.4}$$

Here E_{CC} is the fitted binding energy per central carbon in the adsorbate (all covalent bonds to other carbon atoms) and E_{CH} is the adsorption energy per edge carbon with an adjoining hydrogen atom, the two different carbon types are illustrated for hexabenzocoronene in Figure 6.1.

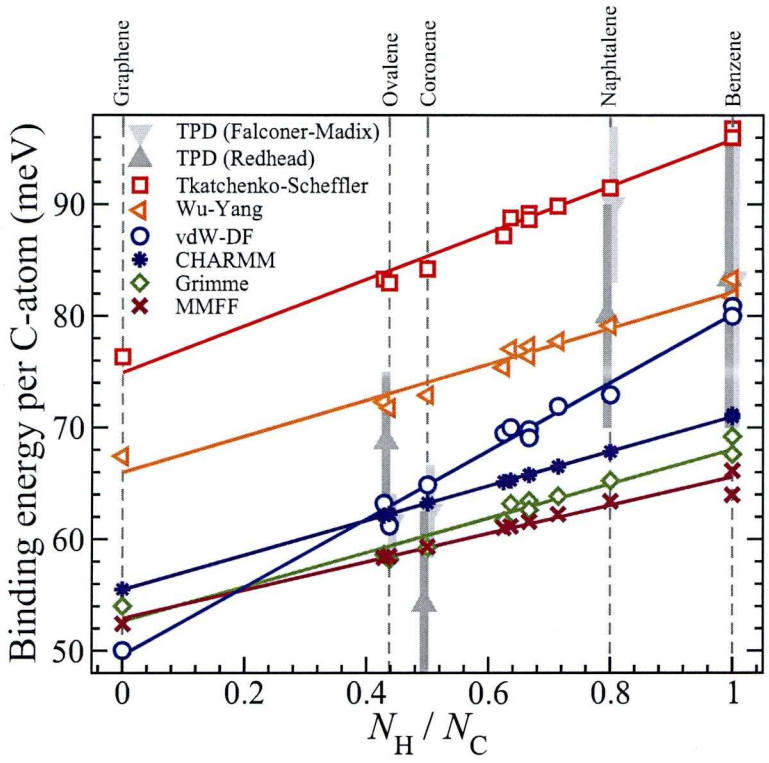

Figure 6.3: The binding energy normalised by the number of carbon atoms for aromatic aromatic hydrocarbons adsorbed on graphene. The grey error bars show data from temperature-programmed desorption experiments [127] for benzene, naphthalene, coronene and hexabenzocoronene, and the binding energy of bilayer graphene from an extrapolation of the TPD data. The vdW-DF binding energies of benzene, naphtalene and graphene agree well with the previous vdW-DF study [129] for these systems.

Table 6.1: Values for the energies E_{CC} and E_{CH}, from the linear fits in Figure 1 of the manuscript, together with the mean absolute error (MAE $= \sum_i |E_{\mathrm{fit},i} - E_{\mathrm{exp},i}|/N_{\mathrm{exp}}$) per atom of the fits with respect to the experimental data from Zacharia and coworkers [127]. The experimentally extrapolated binding energy of bilayer graphene was not included in the calculation of the MAEs.

	E_{CC} (meV)	E_{CH} (meV)	MAE (meV)
vdW-DF	49.2	80.1	6.1
Wu-Yang	66.0	82.1	7.7
CHARMM	55.5	70.9	9.5
Grimme	52.6	68.0	11.4
MMFF	52.9	65.5	12.7
Tkatchenko-Scheffler	74.9	95.8	16.2
Ortmann-Bechstedt-Schmidt	78.1	127.9	39.2

Table 6.1 gives the fitted values of the parameters E_{CC} and E_{CH} for the various correction schemes.

For the semi-empirical schemes (all models except vdW-DF and TS) the linear fit in Figure 6.3 is trivial, and it is merely a result of the assumed additivity of vdW-interactions in these schemes [128]. As all these schemes consider the same C_6 coefficient to be used for all the sp^2 hybridised carbon atoms the difference between the slopes of the curves in Figure 6.3, is a result of the binding energy contributed by the hydrogen atoms and it cannot be attributed to different binding energy for graphene-like and benzene-like carbon atoms.

In contrast to the empirical methods, the vdW-DF as well as the TS correction includes information on the local chemical environment of atoms, either through the non-local density functional or via a Hirshfeld charge decomposition. Notably, the slopes of the linear fits in Eq. (6.3) are larger for the vdW-DF as well as the TS model compared to the semi-empirical and empirical models. The slope is given by $E_{CH} - E_{CC}$, and is equal to 30.9 meV and 20.9 meV for the vdW-DF and TS, respectively, while it is found within the interval 12.6–16.1 meV for the other schemes. In other words, the group of an edge carbon with its adjoining hydrogen interacts stronger with graphene within the vdW-DF and the TS schemes than for any other scheme. There are two possible explanations for the different slopes: (1) In the vdW-DF and TS schemes the hydrogen atoms have a larger contribution to the binding than in the other schemes. (2) The carbon atoms in a PAH with an adjoining hydrogen atom are chemically distinguishable from those without, with the former binding stronger to the substrate. The current data set cannot conclude which of the interpretations (or a combination of the two) is correct, and a further investigation is needed before concluding about this.

From the MAE the vdW-DF is shown to give the best agreement with the experimental data and is thus the recommended correction to use for prediction of the adsorption energy in this type of system. However, although the vdW-DF correctly describes the adsorption energy it is questionable how well the adsorption height is described as the underlying revPBE functional is known to give too large bonding distances. This seems to be the case also in this kind of system, as our calculations of bulk graphite with the revPBE based vdW-DF give inter-layer distances of 3.55 Å, to be compared with the well known experimental value of 3.35 Å. The details of the graphite calculations are outlined in Section C.2.

6.2 Non-local correlation versus electrostatic contribution

It is a general belief in the chemistry community that the attractive interaction between π-systems is a complex interplay between non-local (London) dispersion forces and static Coulomb interactions. However any investigation of the different contributions to the total bonding for PAH on graphene including a quantification of the non-local correlation energy do not exist. Charlier and coworkers [130] approached this problem for the interplanar bonding in graphite. However in their study the exchange-correlation was calculated using LDA in which no non-local bonding effects are taken into account and instead the XC-part of the bonding comes from

the exchange energy.

To study the mechanism behind the bonding in our π-π stacked systems, we decomposed the total binding energy from the vdW-DF calculations into its individual contributions according to

$$E_{\mathrm{tot}}[n] = E_{\mathrm{es}}[n] + E_{\mathrm{c,nl}}[n] + E_{\mathrm{kin}}[n] + E_{\mathrm{x,GGA}}[n] + E_{\mathrm{c,LDA}}[n], \tag{6.5}$$

where E_{es} is the electrostatic Coulomb energy, $E_{\mathrm{c,nl}}$ is the non-local correlation energy, E_{kin} is the kinetic energy, $E_{\mathrm{x,GGA}}$ is the GGA exchange energy, and $E_{\mathrm{c,LDA}}$ is the LDA correlation energy. The total interaction energy, E_{tot}, along with the dispersive $E_{\mathrm{c,nl}}$ and electrostatic (Coulomb) E_{es} contributions are plotted in Figure 6.4 as a function of the separation between adsorbate and graphene layer. A full energy decomposition into all the components is shown in Figure C.2.

Around the equilibrium distance, the total interaction energy is a complex mixture of different interactions. Both the electrostatic energy and the non-local correlation energy has a significant contributions to the total energy, and hence this is in agreement with the general view of π-π stacking that the attractive part of the bonding is a mixture of electrostatic and non-local correlation interactions. However, the exact ratio between non-local correlation and electrostatic energies at the equilibrium separation is sensitive to the position of its energy minimum.

At bonding distances electrostatic and dispersive effects are both important for the stability of the bonds between PAHs and graphene. However, for distances larger than 4.5 Å the electrostatic contribution to the bonding is essentially zero for all adsorbates (and noteworthy even slightly repulsive at large enough distances). For these distances the attractive non-local correlation energy is still significant, and more specifically for distances larger than 4.5 Å the attractive part of the interaction is solely due to non-local correlation. As a consequence, the initial bonding of these systems would not be possible without the attractive vdW interactions. This is illustrated in Figure 6.5 where two binding energy curves are plotted with either the electrostatic or non-local correlation contribution missing, respectively. Without the non-local correlation energy almost no bonding is found between the PAHs and graphene. In the absence of the electrostatic interactions, bonding is still achieved between the PAHs and graphene. This result illustrates the importance of the vdW interactions for the initial formation of the complexes.

6.3 Summary

In summary, the adsorption properties of polyaromatic hydrocarbons on graphene have been investigated as an archetypical system with π-π-interactions. Six different corrections to DFT for dispersion together with two force-field methods have been benchmarked. We find that semi-empirical corrections based on the commonly used $-C_6/R^6$-functional form of the in-

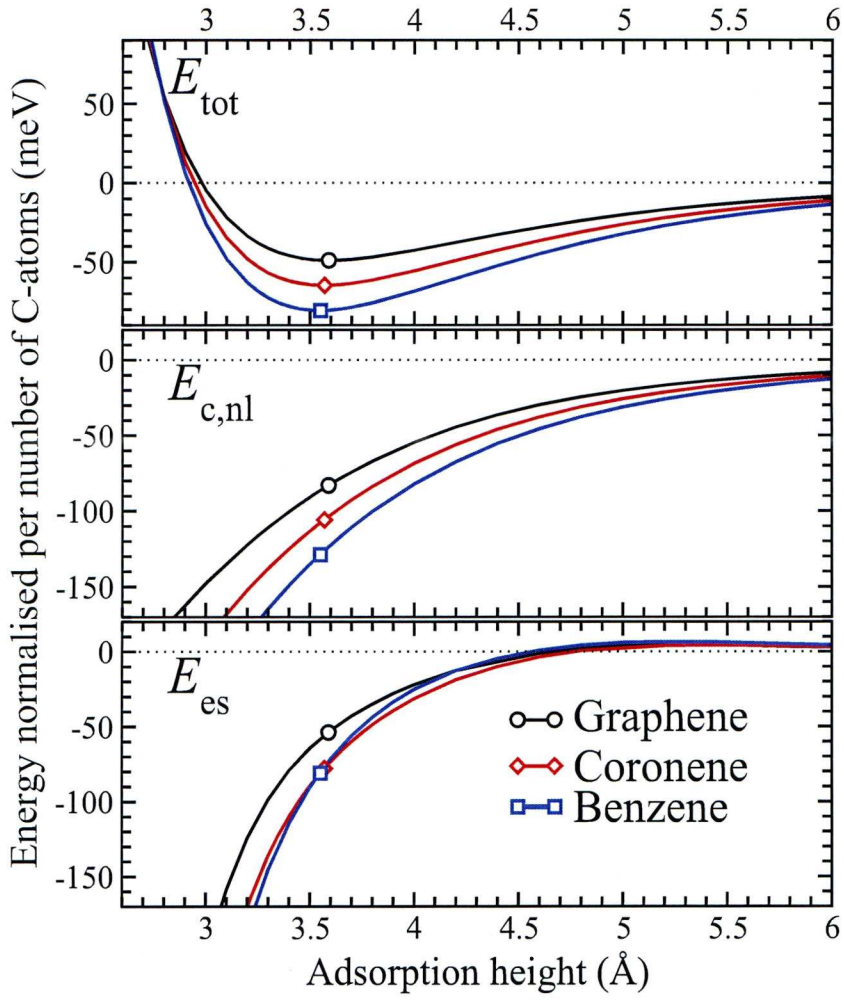

Figure 6.4: Contributions from the non-local correlation energy, $E_{\mathrm{c,nl}}$, and the electrostatic Hartree energy, E_{es}, to the total vdW-DF interaction energy, E_{tot}, for a number of representative hydrocarbons adsorbed on graphene. The circles, squares and diamonds indicate the global energy minima for the different adsorbates. The repulsive contribution at short distances comes from the Pauli repulsion is manifested in the kinetic energy as illustrated in the complete energy decomposition in Figure C.2.

teraction give generally fair results, while the vdW-DF resulted in a better agreement with available experimental data. The binding energy of aromatic hydrocarbons on graphene was found to be additive, hence the total binding energy can be decomposed into contributions from each atomic pair. In particular, a simple yet quantitative estimate of the binding energy for aromatic hydrocarbons on graphene was introduced: using the adsorption energies $E_{\mathrm{CC}} = 49.2$ meV and $E_{\mathrm{CH}} = 80.1$ meV (vdw-DF) per graphene-like and benzene-like carbon atom respectively, one obtains the binding energy for any given aromatic hydrocarbon simply by counting the number of hydrogen and carbon atoms. Within the vdW-DF we found that π-π interactions in physisorption are composed of a complex mixture of dispersive and electrostatic interactions. It is concluded that purely dispersive forces drive the docking of neutral adsorbates on graphene and that electrostatic interactions have an important contribution to the attractive part

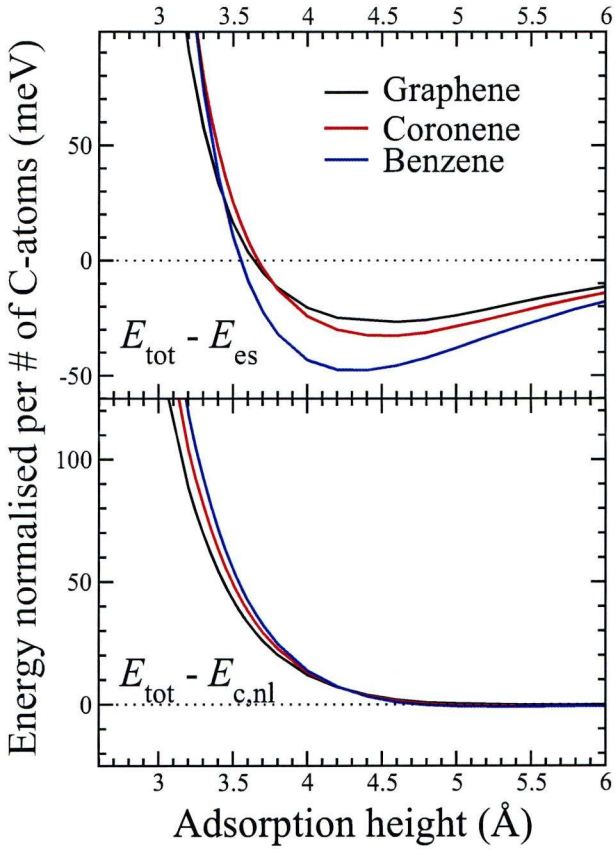

Figure 6.5: Binding curves for the vdW-DF with either the electrostatic (Coulomb) energy $E_{\rm es}$ or the non-local correlation energy $E_{\rm c,nl}$ missing for a number of representative hydrocarbons adsorbed on graphene. Note that a binding occur for all hydrocarbons if the $E_{\rm es}$ is missing while almost no bonding is observed if instead the $E_{\rm c,nl}$ term is neglected, illustrating the importance of the dispersion forces over the electrostatic (Coulomb) interactions for the formation of the complexes.

of the bonding around binding distances. The repulsive contribution at short distances comes from the Pauli repulsion which is manifested in the kinetic energy

Chapter 7

Concluding remarks and outlook

Theory and modelling of organic molecules on surfaces has been the common theme behind the results presented in this thesis. Three rather different types of systems have been investigated. The results for each of these systems are summarised at the end of Chapters 4-6, of which a few key results will be highlighted once again.

Porous network formation through adatom-coordination The two porous networks formed by either TAPP or DPDI molecules on the Cu(111) surface are stabilised through coordination of the molecules to copper adatoms. Furthermore, in the case of DPDI a complete dehydrogenation of the nitrogen atoms drives the network formation, resulting in a honeycomb structure of tridehydro-DPDI species.

Nature of N–Cu coordination bonds The interaction between adatoms and organic ligands in the porous networks are characterised by lowering in energy of the nitrogen lone-pair orbitals, as well as a partial filling of the lowest unoccupied molecular orbital. Furthermore, the results suggest that there is a synergism between the filling of the LUMO and the lowering of the nitrogen lone-pair orbitals. This is in analogy with the synergism between σ-donation and π-backbonding in coordination chemistry.

Fingerprint of metal-ligand interactions The interactions between copper adatoms and organic ligands give rise to a characteristic unoccupied electronic state. This state can be imaged in STM as a fingerprint of the coordination between the Cu adatoms and the organic ligands, and provides a method for proving that native adatoms are taking part in the formation of the networks.

Survival of un-paired electron of organic radical upon adsorption on a metal surface The organic radical 3CP molecule, deprotonates upon adsorption on the Cu(110) surface at room temperature and bonds to the surface with the resulting carboxylate group. The unpaired

spin, which resides in the NO group, is predicted to survive upon the adsorption of the molecule on the surface.

Van der Waals interactions for metal-organic interfaces A modified van der Waals density functional and the semi-empirical scheme by Grimme from 2006 give a fair description of the adsorption heights of the TAPP and tridehydro-DPDI porous networks. The Grimme correction scheme gives the general best description of the heights of the TAPP and DPDI molecules. None of the correction schemes changes the bonding trend from semi-local (PW91) calculations. Semi-local DFT is thus sufficient for comparing different adsorption configurations of these two molecules on the Cu(111) surface.

Prediction of binding energies of aromatic hydrocarbons on graphene The conventional form of the van der Waals density functional, which is based on revPBE exchange, gives the best prediction of the binding energy of polycyclic aromatic hydrocarbons on graphene, compared to six empirical van der Waals correction schemes to DFT. Furthermore, for all models the binding energy normalised by the number of adsorbate carbon atoms follows a linear trend with respect to the adsorbate hydrogen-to-carbon ratio. From this relationship the binding energy of any polycyclic aromatic hydrocarbon on graphene can be obtained without any additional calculations.

Nature of the π-π stacking between hydrocarbons and graphene The π-π stacking of polycyclic aromatic hydrocarbons on graphene is predominantly dispersive for separations larger than 4.5 Å, and is necessary for the initial formation of these complexes. For separations close to the equilibrium binding distance the binding is characterised by a complex mixing of dispersive and electrostatic interactions.

Outlook

The work presented here has provided some new insights into the phenomena of molecule-surface interaction, as well as the interaction between molecules adsorbed on a surface. I will round up this thesis by mentioning a few possible directions for future work.

The 3CP molecule is predicted to remain as a radical upon adsorption on the Cu(110) surface, but no long-range ordering of the molecule has been achieved. Is it possible to use the TAPP or DPDI porous network to host the 3CP molecule, hence creating an ordered array of 3CP molecules? This would require that (1) the molecule is still a radical also after adsorption on the Cu(111) surface and that (2) the porous template does not interfere with the unpaired spin.

The honeycomb network of tridehydro-DPDI network has been shown experimentally to confine the Shockley surface state of Cu(111). Is it possible to understand this confinement using theoretical modelling within the framework of DFT? In that case, how sensitive is the

confinement to the adsorption height; or how precise do we need to describe the molecular adsorption for modelling of the surface state?

For a reliable prediction of the adsorption of large organic molecules we need an accurate description of the van der Waals interactions. We have illustrated two seemingly rather contradictory results in this thesis: The van der Waals density functional was found to give the best prediction of the binding energy of polycyclic aromatic hydrocarbons on graphene, while the same functional gives too large adsorption heights of perylene deriative on Cu(111), for which instead the Grimme correction scheme performed best. Further benchmarking studies including other correction schemes, but also different kind of systems, are needed before the DFT community can agree on a universal method for including van der Waals forces into theoretical modelling of organic molecules on metal surfaces.

Bibliography

[1] G. Ertl, *Reactions at surfaces: from atoms to complexity*, Nobel lecture (2007).

[2] K. Honkala, A. Hellman, I. N. Remediakis, A. Logadottir, A. Carlsson, S. Dahl, C. H. Christensen, and J. K. Nørskov, *Ammonia Synthesis from First-Principles Calculations*, Science **307**, 555–558 (2005).

[3] A. Zangwill, *Physics at surfaces*, Cambridge University press (1988).

[4] Information gathered from *http://nobelprize.org*.

[5] G. Binnig, H. Rohrer, C. Gerber, and E. Weibel, *7 × 7 Reconstruction on Si(111) Resolved in Real Space*, Physical Review Letters **50**, 120–123 (1983).

[6] M. F. Crommie, C. P. Lutz, and D. M. Eigler, *Confinement of Electrons to Quantum Corrals on a Metal Surface*, Science **262**, 218–220 (1993).

[7] P. Hohenberg and W. Kohn, *Inhomogeneous Electron Gas*, Physical Review **136**, B864–B871 (1964).

[8] W. Kohn and L. J. Sham, *Self-Consistent Equations Including Exchange and Correlation Effects*, Physical Review **140**, A1133–A1138 (1965).

[9] J. P. Perdew, J. A. Chevary, S. H. Vosko, K. A. Jackson, M. R. Pederson, D. J. Singh, and C. Fiolhais, *Atoms, molecules, solids, and surfaces: Applications of the generalized gradient approximation for exchange and correlation*, Physical Review B **46**, 6671–6687 (1992).

[10] J. P. Perdew, K. Burke, and M. Ernzerhof, *Generalized Gradient Approximation Made Simple*, Physical Review Letters **77**, 3865–3868 (1996).

[11] M. Dion, H. Rydberg, E. Schroder, D. C. Langreth, and B. I. Lundqvist, *Van der Waals Density Functional for General Geometries*, Physical Review Letters **92**, 246401–246404 (2004).

[12] Y. Vaynzof, D. Kabra, L. Zhao, P. K. H. Ho, A. T.-S. Wee, and R. H. Friend, *Improved photoinduced charge carriers separation in organic-inorganic hybrid photovoltaic devices*, Applied Physics Letters **97**, 033309–033311 (2010).

[13] C. Joachim, J. K. Gimzewski, and A. Aviram, *Electronics using hybrid-molecular and mono-molecular devices*, Nature **408**, 541–548 (2000).

[14] J. V. Barth, G. Constantini, and K. Kern, *Engineering atomic and molecular nanostructures at surfaces*, Nature **437**, 671–679 (2005).

[15] T. D. Ladd, F. Jelezko, R. Laflamme, Y. Nakamura, C. Monroe, and J. L. O'Brien, *Quantum computers*, Nature **464**, 45–53 (2010).

[16] P. Feibelman, B. Hammer, J. Norskov, F. Wagner, M. Scheffler, R. Stump, R. Watwe, and J. Dumesic, *The CO/Pt(111) Puzzle a*, Journal of Physical Chemistry B **105**, 4018–4025 (2001).

[17] L. Schimka, J. Harl, A. Stroppa, A. Grüneis, M. Marsman, F. Mittendorfer, and G. Kresse, *Accurate surface and adsorption energies from many-body perturbation theory*, Nature Materials **9**, 741–744 (2010).

[18] B. Hammer, M. Scheffler, K. W. Jacobsen, and J. K. Nørskov, *Multidimensional Potential Energy Surface for H_2 Dissociation over Cu(111)*, Physical Review Letters **73**, 1400–1403 (1994).

[19] W. Ho, *Single-molecule chemistry*, Journal of Chemical Physics **117**, 11033 (2002).

[20] A. Kretschmann, M.-M. Walz, K. Flechtner, H.-P. Steinrück, and J. M. Gottfried, *Tetraphenylporphyrin picks up zinc atoms from a silver surface*, Chemical Communications 568–570 (2007).

[21] P. Liljeroth, J. Repp, and G. Meyer, *Current-Induced Hydrogen Tautomerization and Conductance Switching of Naphthalocyanine Molecules*, Science **317**, 1203–1206 (2007).

[22] M. E. Garah, B. Baris, B. Baris, V. Luzet, F. Palmino, and F. Chérioux, *Reversible Single Molecular Switch Operating at 300 K on a Surface*, Chemphyschem **11**, 2568–2572 (2010).

[23] Y. Shirai, A. J. Osgood, Y. Zhao, K. F. Kelly, and J. M. Tour, *Directional Control in Thermally Driven Single-Molecule Nanocars*, Nano Letters **5**, 2330–2334 (2005).

[24] M. Mannini, L. Sorace, L. Gorini, F. M. Piras, A. Caneschi, A. Magnani, S. Menichetti, and D. Gatteschi, *Self-assembled organic radicals on Au(111) surfaces: A combined ToF-SIMS, STM and ESR study*, Langmuir **23**, 2389–2397 (2007).

[25] D. Gatteschi, P. Carretta, and A. Lascialfari, *Molecular magnets and magnetic nanoparticles: new opportunities for μSR investigations*, Physica B **289–290**, 94–105 (2000).

[26] J. V. Yakhmi, *Magnetism as a functionality at the molecular level*, Physica B **321**, 204–212 (2002).

[27] J. Carrasco, A. Michaelides, M. Forster, R. R. Sam Haq, and A. Hodgson, *A one-dimensional ice structure built from pentagons*, Nature Materials **8**, 427–431 (2009).

[28] D. Menzel, *Water on a Metal Surface*, Science **295**, 58–59 (2002).

[29] M. Ortega Lorenzo, C. J. Baddeley, C. Muryn, and R. Raval, *Extended surface chirality from supramolecular assemblies of adsorbed chiral molecules*, Nature **404**, 376–379 (2000).

[30] R. G. Nuzzo and D. L. Allara, *Adsorption of bifunctional organic disulfides on gold surfaces*, Journal of the American Chemical Society **105**, 4481–4483 (1983).

[31] R. K. Smith, P. A. Lewis, and P. S. Weiss, *Patterning self-assembled monolayers*, Progress in Surface Science **75**, 1–68 (2004).

[32] R. Temirov, S. Soubatch, A. Luican, and F. S. Tautz, *Free-electron-like dispersion in an organic monolayer film on a metal substrate*, Nature **444**, 350–353 (2006).

[33] C. H. Schwalb, S. Sachs, M. Marks, A. Schöll, F. Reinert, E. Umbach, and U. Höfer, *Electron Lifetime in a Shockley-Type Metal-Organic Interface State*, Physical Review Letters **101**, 146801–146804 (2008).

[34] M. S. Dyer and M. Persson, *The nature of the observed free-electron-like state in a PTCDA monolayer on Ag(111)*, New Journal of Physics **12**, 063014–063022 (2010).

[35] J. Lobo-Checa, M. Matena, K. Müller, J. H. Dil, F. Meier, L. H. Gade, T. A. Jung, and M. Stöhr, *Band formation from coupled quantum dots formed by a nanoporous network on a cupper surface*, Science **325**, 300–303 (2009).

[36] Z. Cheng, J. Wyrick, M. Luo, D. Sun, D. Kim, Y. Zhu, W. Lu, K. Kim, T. L. Einstein, and L. Bartels, *Adsorbates in a Box: Titration of Substrate Electronic States*, Physical Review Letters **105**, 066104–066107 (2010).

[37] Z. Cheng, M. Luo, J. Wyrick, D. Sun, D. Kim, Y. Zhu, W. Lu, K. Kim, T. L. Einstein, and L. Bartels, *Power of Confinement: Adsorbate Dynamics on Nanometer-Scale Exposed Facets*, Nano Letters **10**, 3700–3703 (2010).

[38] N. Wintjes, D. Bonifazi, F. Cheng, A. Kiebele, M. Stöhr, T. Jung, H. Spillmann, and F. Diederich, *A Supramolecular Multiposition Rotary Device*, Angewandte Chemie International Edition **46**, 4089–4092 (2007).

[39] C. Dri, M. V. Peters, J. Schwarz, S. Hecht, and L. Grill, *Spatial periodicity in molecular switching*, Nature Nanotechnology **3**, 649–653 (2008).

[40] J. M. Lehn, *Supramolecular chemistry: concepts and perspectives*, Wiley-VCH (1995).

[41] S. Griessl, M. Lackinger, M. Edelwirth, M. Hietschold, and W. M. Heckl, *Self-assembled two-dimensional molecular host-guest architectures from trimesic acid*, Single molecules **3**, 25–31 (2002).

[42] C.-A. Palma, M. Bonini, A. Llanes-Pallas, T. Breiner, M. Prato, D. Bonifazi, and P. Samorì, *Pre-programmed bicomponent porous networks at the solid-liquid interface: The low concentration regime*, Chemical Communications **42**, 5289–5291 (2008).

[43] C.-A. Palma, J. Bjork, M. Bonini, M. S. Dyer, A. Llanas-Pallas, D. Bonifazi, M. Persson, and P. Samori, *Tailoring Bicomponent Supramolecular Nanoporous Networks: The Role of Phase Segregation and Polymorphism at the Solid-liquid interface*, Journal of the American Chemical Society **131**, 13062–13071 (2009).

[44] M. Mura, F. Silly, G. A. D. Briggs, M. R. Castell, and L. N. Kantorovich, *H-bonding supramolecular assemblies of PTCDI molecules on the Au(111) surface*, Journal of Physical Chemistry C **113**, 21840–21848 (2009).

[45] M. Mura, X. Sun, F. Silly, H. T. Jonkman, G. A. D. Briggs, M. R. Castell, and L. N. Kantorovich, *Experimental and theoretical analysis of H-bonded supramolecular assemblies of PTCDA molecules*, Physical Review B **81**, 195412– 195422 (2010).

[46] X. Sun, H. Jonkman, and F. Silly, *Tailoring two-dimensional PTCDA-melamine self-assembled architectures at room temperature by tuning molecular ratio*, Nanotechnology **21**, 165602 (2010).

[47] J. Adisoejoso, K. Tahara, S. Okuhata, S. Lei, Y. Tobe, and S. De Feyter, *Two-dimensional crystal engineering: A four-component architecture at a liquid-solid interface*, Angewandte Chemie International Edition **48**, 7353–7357 (2009).

[48] J. V. Barth, *Fresh perspectives for surface coordination chemistry*, Surface Science **603**, 1533–1541 (2009).

[49] M. Matena, T. Riehm, M. Stöhr, T. A. Jung, and L. H. Gade, *Transforming Surface Coordination Polymers into Covalent Surface Polymers: Linked Polycondensed Aromatics through Oligomerization of N-Heterocyclic Carbene Intermediates*, Angewandte Chemie International Edition **47**, 2414–2417 (2008).

[50] L. Grill, M. Dyer, L. Lafferentz, M. Persson, M. V. Peters, and S. Hecht, *Nano-architectures by covalent assembly of molecular building blocks*, Nature Nanotechnology **2**, 687 (2007).

[51] S. Weigelt, C. Busse, C. Bombis, M. M. Knudsen, K. V. Gothelf, E. Lægsgaard, F. Besenbacher, and T. R. Linderoth, *Surface synthesis of 2D branched polymer nanostructures*, Angewandte Chemie International Edition **47**, 4406–4410 (2008).

[52] D. F. Perepichka and F. Rosei, *Extending Polymer Conjugation into the Second Dimension*, Science **323**, 216–217 (2009).

[53] A. Dmitriev, H. Spillmann, N. Lin, J. V. Barth, and K. Kern, *Modular Assembly of Two-Dimensional Metal-Organic Coordination Networks at a Metal Surface*, Angewandte Chemie International Edition **42**, 2670–2673 (2003).

[54] N. Lin, S. Stepanow, M. Ruben, and J. V. Barth, *Surface-Confined Supramolecular Coordination Chemistry*, Topics in Current Chemistry **287**, 1–44 (2009).

[55] U. Schlickum, R. Decker, F. Klappenberger, G. Zoppellaro, S. Klyatskaya, M. Ruben, I. Silanes, A. Arnau, K. Kern, and J. V. B. H. Brune and, *Metal–Organic Honeycomb Nanomeshes with Tunable Cavity Size*, Nano Letters **7**, 3813–3817 (2007).

[56] F. Klappenberger, D. Kühne, W. Krenner, I. Silanes, A. Arnau, F. J. G. de Abaja, S. Klyatskaya, M. Ruben, and J. V. Barth, *Dichotomous Array of Chiral Quantum Corrals by a Self-Assembled Nanoporous Kagomé Network*, Nano Letters **9**, 3509–3514 (2009).

[57] Kühne, F. Klappenberger, R. Decker, U. Schlickum, H. Brune, S. Klyatskaya, M. Ruben, and J. V. Barth, *Self-Assembly of Nanoporous Chiral Networks with Varying Symmetry from Sexiphenyl-dicarbonitrile on Ag(111)*, The Journal of Physical Chemistry C **113**, 17851–17859 (2009).

[58] T. Classen, G. Fratesi, G. Costantini, S. Fabris, F. L. Stadler, C. Kim, S. de Gironcoli, S. Baroni, and K. Kern, *Templated Growth of Metal-Organic Coordination Chains at Surfaces*, Angewandte Chemie International Edition **44**, 6142–6145 (2005).

[59] D. Heim, D. Écija, K. Seufert, W. Auwärter, C. Aurisicchio, C. Fabbro, D. Bonifazi, and J. V. Barth, *Self-Assembly of Flexible One-Dimensional Coordination Polymers on Metal Surfaces*, Journal of the American Chemical Society **132**, 6783–6790 (2010).

[60] D. Kühne, F. Klappenberger, R. Decker, U. Schlickum, H. Brune, S. Klyatskaya, M. Ruben, and J. V. Barth, *High-Quality 2D Metal–Organic Coordination Network Providing Giant Cavities within Mesoscale Domains*, Journal of the American Chemical Society **131**, 3881–3883 (2009).

[61] M. Matena, M. Stöhr, T. Riehm, J. Björk, S. Martens, M. S. Dyer, M. Persson, J. Lobo-Checa, K. Müller, M. Enache, H. Wadepohl, J. Zegenhagen, T. A. Jung, and L. H. Gade, *Aggregation and contingent metal/surface reactivity of 1,3,8,10-tetraazaperopyrene (TAPP) on Cu(111)*, Chemistry - A European Journal **16**, 2079–2091 (2010).

[62] M. Stöhr, M. Wahl, C. H. Galka, T. Riehm, T. A. Jung, and L. H. Gade, *Controlling Molecular Assembly in Two Dimensions: The Concentration Dependence of Thermally Induced 2D Aggregation of Molecules on a Metal Surface*, Angewandte Chemie International Edition **44**, 7394–7398 (2005).

[63] A. P. Seitsonen, M. Lingenfelder, H. Spillmann, A. Dmitriev, S. Stepanow, N. Lin, K. Kern, and J. V. Barth, *Density Functional Theory Analysis of Carboxylate-Bridged Diiron Units in Two-Dimensional Metal-Organic Grids*, Journal of the American Chemical Society **128**, 5634–5635 (2006).

[64] G. Pawin, K. L. Wong, D. Kim, D. Sun, L. Bartels, S. Hong, T. S. Rahman, R. Carp, and M. Marsella, *A Surface Coordination Network Based on Substrate-Derived Metal Adatoms with Local Charge Excess*, Angewandte Chemie International Edition **47**, 8442–8445 (2008).

[65] P. Maksymovych and J. T. Yates, *Au adatoms in self-assembly of benzenethiol on the Au(111) surface*, Journal of the American Chemical Society **130**, 7518–7519 (2008).

[66] P. Maksymovych, D. C. Sorescu, and J. T. Yates, *Gold-Adatom-Mediated Bonding in Self-Assembled Short-Chain Alkanethiolate Species on the Au(111) Surface*, Physical Review Letters **97**, 146103–146106 (2006).

[67] J. Barth, J. Weckesser, N. Lin, A. Dmitriev, and K. Kern, *Supramolecular architectures and nanostructures at metal surfaces*, Applied Physics A: Materials Science & Processing **76**, 645–652 (2003).

[68] N. Lin, A. Dmitriev, J. Weckesser, J. V. Barth, and K. Kern, *Real-Time Single-Molecule Imaging of the Formation and Dynamics of Coordination Compounds*, Angewandte Chemie International Edition **41**, 4779–4783 (2002).

[69] C. C. Perry, S. Haq, B. G. Frederick, and N. V. Richardson, *Face specificity and the role of metal adatoms in molecular reorientation at surfaces*, Surface Science **409**, 512–520 (1998).

[70] D. Dougherty, P. Maksymovych, and J. Yates, *Direct STM evidence for Cu-benzoate surface complexes on Cu(1 1 0)*, Surface Science **600**, 4484–4491 (2006).

[71] L. Romaner, D. Nabok, P. Puschnig, E. Zojer, and C. Ambrosch-Draxl, *Theoretical study of PTCDA adsorbed on the coinage metal surfaces, Ag(111), Au(111) and Cu(111)*, New Journal of Physics **11**, 053010–053030 (2009).

[72] T. Thonhauser, V. R. Cooper, S. Li, A. Puzder, P. Hyldgaard, and D. C. Langreth, *Van der Waals density functional: Self-consistent potential and the nature of the van der Waals bond*, Physical Review B **76**, 125112–125122 (2007).

[73] O. A. Vydrov and T. V. Voorhis, *Nonlocal van der Waals Density Functional Made Simple*, Physical Review Letters **103**, 063004 (2009).

[74] A. Gulans, M. J. Puska, and R. M. Nieminen, *Linear-scaling self-consistent implementation of the van der Waals density functional*, Physical Review B **79**, 201105–201108 (2009).

[75] J. Klimes, D. R. Bowler, and A. Michaelides, *Chemical accuracy for the van der Waals density functional*, Journal of Physics: Condensed Matter **22**, 022201–022205 (2010).

[76] Q. Wu and W. Yang, *Empirical correction to density functional theory for van der Waals interactions*, Journal of Chemical Physics **116**, 515–524 (2002).

[77] S. Grimme, *Semiempirical GGA-Type Density Functional Constructed with a Long-Range Dispersion Correction*, Journal of Computational Chemistry **27**, 1787–1799 (2006).

[78] F. Ortmann, F. Bechstedt, and W. G. Schmidt, *Semiempirical van der Waals correction to the density functional description of solids and molecular structures*, Physical Review B **73**, 205101–205110 (2006).

[79] A. Tkatchenko and M. Scheffler, *Accurate Molecular Van Der Waals Interactions from Ground-State Electron Density and Free-Atom Reference Data*, Physical Review Letters **102**, 073005–073008 (2009).

[80] S. Grimme, J. Antony, S. Ehrlich, , and H. Krieg, *A consistent and accurate ab initio parametrization of density functional dispersion correction (DFT-D) for the 94 elements H-Pu*, The Journal of Chemical Physics **132**, 154104–154122 (2010).

[81] L. Spanu, S. Sorella, and G. Galli, *Nature and Strength of Interlayer Binding in Graphite*, Physical Review Letters **103**, 196401–196404 (2009).

[82] K. Burke, *ABC to DFT*, http://dft.uci.edu/materials/bookABCDFT/gamma/g1.pdf (2007).

[83] D. M. Ceperley and B. J. Alder, *Ground State of the Electron Gas by a Stochastic Method*, Physical Review Letters **45**, 566–569 (1980).

[84] S. H. Vosko, L. Wilk, and M. Nusair, *Accurate spin-dependent electron liquid correlation energies for local spin density calculations: a critical analysis*, Canadian Journal of Physics **58**, 1200–1211 (1980).

[85] J. P. Perdew and A. Zunger, *Self-interaction correction to density-functional approximations for many-electron systems*, Physical Review B **23**, 5048–5079 (1981).

[86] J. P. Perdew and Y. Wang, *Accurate and simple analytic representation of the electron-gas correlation energy*, Phys Rev B **45**, 13244–13249 (1992).

[87] P. Haas, F. Tran, P. Blaha, K. Schwarz, and R. Laskowski, *Insight into the performance of GGA functionals for solid-state calculations*, Physical Review B **80**, 195109–195121 (2009).

[88] Y. Zhang and W. Yang, *Comment on "Generalized Gradient Approximation Made Simple"*, Physical Reviev Letters **80**, 890 (1998).

[89] D. C. Langreth, M. Dion, H. Rydberg, E. Schröder, P. Hyldgaard, and B. I. Lundqvist, *Van der Waals Density Functional with Applications*, J Quant Chem **101**, 599 (2005).

[90] O. A. Vydrov, Q. Wu, and T. V. Voorhis, *Self-consistent implementation of a nonlocal van der Waals density functional with a Gaussian basis set*, The Journal of Chemical Physics **129**, 014106–014113 (2008).

[91] G. Román-Pérez and J. M. Soler, *Efficient Implementation of a van der Waals Density Functional: Application to Double-Wall Carbon Nanotubes*, Physical Review Letters **103**, 096102–096105 (2009).

[92] F. London, *Zur Theorie und Systematik der Molekularkräfte*, Zeitschrift für Physik A Hadrons and Nuclei **63**, 245–279 (1930).

[93] P. Jurecka, J. Sponer, J. Cerný, and P. Hobza, *Benchmark database of accurate (MP2 and CCSD(T) complete basis set limit) interaction energies of small model complexes, DNA base pairs, and amino acid pairs*, Physical Chemistry Chemical Physics **8**, 1983–1993 (2006).

[94] H. J. Monkhorst and J. D. Pack, *Special points for Brillouin-zone integrations*, Physical Review B **13**, 5188–5192 (1976).

[95] P. E. Blöchl, *Projector augmented-wave method*, Physical Review B **50**, 17953–17979 (1994).

[96] G. Kresse and D. Joubert, *From ultrasoft pseudopotentials to the projector augmented-wave method*, Physical Review B **59**, 1758–1775 (1999).

[97] G. Binnig, H. Rohrer, C. Gerber, and E. Weibel, *Surface Studies by Scanning Tunneling Microscopy*, Physical Review Letters **49**, 57–61 (1982).

[98] S. Chiang, *Scanning Tunneling Microscopy Imaging of Small Adsorbed Molecules on Metal Surfaces in an Ultrahigh Vacuum Environment*, Chemical Reviews **97**, 1083–1096 (1997).

[99] J. Repp, G. Meyer, S. M. Stojković, A. Gourdon, and C. Joachim, *Molecules on Insulating Films: Scanning-Tunneling Microscopy Imaging of Individual Molecular Orbitals*, Physical Review Letters **94**, 026803–026806 (2005).

[100] J. Bardeen, *Tunnelling from a Many-Particle Point of View*, Physical Review Letters **6**, 57–59 (1961).

[101] J. Tersoff and D. R. Hamann, *Theory and Application for the Scanning Tunneling Microscope*, Physical Review Letters **50**, 1998–2001 (1983).

[102] J. Tersoff and D. R. Hamann, *Theory of the scanning tunneling microscope*, Physical Review B **31**, 805–813 (1985).

[103] D. Porezag and M. R. Pederson, *Infrared intensities and Raman-scattering activities within density-functional theory*, Physical Review B **54**, 7830–7836 (1996).

[104] S. Bahn and K. Jacobsen, *An object-oriented scripting interface to a legacy electronic structure code*, Computing in Science & Engineering **4**, 56–66 (2002).

[105] S. Hüfner, *Photoelectron spectroscopy: Principles and applications 3th edition*, Springer-Verlag Berlin Heidelberg New York (2003).

[106] L. Köhler and G. Kresse, *Density functional study of CO on Rh(111)*, Physical Review B **70**, 165405–165413 (2004).

[107] B. Johansson and N. Mårtensson, *Core-level binding-energy shifts for the metallic elements*, Phys Rev B **21**, 4427–4457 (1980).

[108] J. Zegenhagen, *Surface structure determination with X-ray standing waves*, Surface Science Reports **18**, 202 – 271 (1993).

[109] D. P. Woodruff, *Surface structure determination using x-ray standing waves*, Reports on Progress in Physics **68**, 743–798 (2005).

[110] M. Matena, *Observing Cooperative Behaviour with Molecular Surface Structures*, Ph.D. thesis, University of Basel (2009).

[111] M. Wahl, *Reactions of Organic Molecules on Metal Surfaces studied by STM*, Ph.D. thesis, University of Basel (2006).

[112] T. Riehm, G. D. Paoli, A. E. Konradsson, L. D. Cola, H. Wadepohl, and L. H. Gade, *Tetraazaperopyrenes: A New Class of Multifunctional Chromophores*, Chemistry - A European Journal **13**, 7317–7329 (2007).

[113] K. W. Hellmann, C. H. Galka, I. Rüdenauer, L. H. Gade, I. J. Scowen, and M. McPartlin, *Metal-Ligand versus Metal-Metal Redox Chemistry: Thallium(I)-Induced Synthesis of 4,9-Diaminoperylenequinone-3,10-diimine Derivatives*, Angewandte Chemie International Edition **37**, 1948–1952 (1998).

[114] L. H. Gade, C. H. Galka, K. W. Hellmann, R. M. Williams, L. D. Cola, I. J. Scowen, and M. McPartlin, *Tetraaminoperylenes: Their Efficient Synthesis and Physical Properties*, Chemistry - A European Journal **8**, 3732–3746 (2002).

[115] T. Kammler and J. Küppers, *Interaction of H atoms with Cu(111) surfaces: Adsorption, absorption, and abstraction*, Journal of Chemical Physics **1111**, 8115–8123 (1999).

[116] W. Tang, E. Sanville, and G. Henkelman, *A grid-based Bader analysis algorithm without lattice bias*, Journal of Physics: Condensed Matter **21**, 084204–084210 (2009).

[117] R. F. W. Bader, *Atom in molecules – A quantum theory*, Clarendon Press, Oxford (1994).

[118] S. Duhm, A. Gerlach, I. Salzmann, B. Bröker, R. Johnson, F. Schreiber, and N. Koch, *PTCDA on Au(111), Ag(111) and Cu(111): Correlation of interface charge transfer to bonding distance*, Organic Electronics **9**, 111–118 (2008).

[119] L. H. Gade, *Koordinationschemie*, Wiley-VCH (1998).

[120] Private communication with Lutz H. Gade.

[121] J. Björk, M. Matena, M. S. Dyer, M. Enache, J. Lobo-Checa, L. H. Gade, T. A. Jung, M. Stöhr, and M. Persson, *STM fingerprint of molecule-adatom interactions in a self-assembled metal-organic surface coordination network on Cu(111)*, Physical Chemistry Chemical Physics **12**, 8815–8821 (2010).

[122] G. Mercurio, E. R. McNellis, I. Martin, S. Hagen, F. Leyssner, S. Soubatch, J. Meyer, M. Wolf, P. Tegeder, F. S. Tautz, , and K. Reuter, *Structure and Energetics of Azobenzene on Ag(111): Benchmarking Semiempirical Dispersion Correction Approaches*, Physical Review Letters **104**, 036102–036105 (2010).

[123] K. Lee, E. D. Murray, L. Kong, B. I. Lundqvist, and D. C. Langreth, *Higher-accuracy van der Waals density functional*, Physical Review B **82**, 081101–081104 (2010).

[124] Q. Chen, C. Perry, B. Frederick, P. Murray, S. Haq, and N. Richardson, *Structural aspects of the low-temperature deprotonation of benzoic acid on Cu(110) surfaces*, Surface Science **446**, 63–75 (2000).

[125] B. E. Hayden, K. Prince, D. P. Woodruff, and A. M. Bradshaw, *An IRAS study of formic acid and surface formate adsorbed on Cu(110)*, Surface Science **133**, 589–604 (1983).

[126] A. J. Cohen, P. Mori-Sànchez, and W. Yang, *Insights into Current Limitations of Density Functional Theory*, Science **321**, 792–794 (2008).

[127] R. Zacharia, H. Ulbricht, and T. Hertel, *Interlayer cohesive energy of graphite from thermal desorption of polyaromatic hydrocarbons*, Physical Review B **69**, 155406–1554012 (2004).

[128] N. L. Allinger, Y. H. Yuh, and J. H. Lii, *Molecular mechanics. The MM3 force field for hydrocarbons. 1*, Journal of the American Chemical Society **111**, 8551–8566 (1989).

[129] S. D. Chakarova-Käck, E. Schröder, B. I. Lundqvist, and D. C. Langreth, *Application of van der Waals Density Functional to an Extended System: Adsorption of Benzene and Naphtalene on Graphene*, Physical Review Letters **96**, 146107–166110 (2006).

[130] J.-C. Charlier, X. Gonze, and J.-P. Michenaud, *Graphite Interplanar Bonding: Electronic Delocalization and van der Waals Interaction*, Europhysics Letter **28**, 403–408 (1994).

[131] G. Kresse and J. Furthmüller, *Efficient iterative schemes for ab initio total-energy calculations using a plane-wave basis set*, Physical Review B **54**, 11169–11186 (1996).

[132] D. E. Hooks, T. Fritz, and M. D. Ward, *Epitaxy and Molecular Organization on Solid Substrates*, Advanced Materials **13**, 227–241 (2001).

[133] V. Blum, R. Gehrke, F. Hanke, P. Havu, V. Havu, X. Ren, K. Reuter, and M. Scheffler, *Ab initio molecular simulations with numeric atom-centered orbitals*, Computer Physics Communications **180**, 2175–2196 (2009).

[134] B. R. Brooks, R. E. Bruccoleri, B. D. Olafson, D. J. States, S. Swaminathan, and M. Karplus, *CHARMM: A program for macromolecular energy, minimization, and dynamics calculations*, Journal of Computational Chemistry **4**, 187 (1983).

[135] W. L. Jorgensen, D. S. Maxwell, and J. Tirado-Rives, *Development and Testing of the OPLS All-Atom Force Field on Conformational Energetics and Properties of Organic Liquids*, Journal of the American Chemical Society **118**, 11225–11236 (1996).

A

Appendix to Chapter 4

A.1 Computational details

All calculations were done within the framework of periodic density-functional theory using the Vienna Ab-initio Simulation Package (VASP) [131]. The ion-core interaction was described by the projector augmented wave method [95,96] and, unless stated otherwise, the generalised gradient approximation through the Perdew Wang 91 (PW91) functional [9] was used to describe exchange-correlation effects. The plane-wave basis set was expanded up to 400 eV.

The copper (111) substrates were modelled by four layer slabs separated by 15 Å of vacuum region. Structural optimisations were performed until the force acting on each atom in molecules, adatoms and the two outermost layers of the copper substrate was below 0.01 eV/Å. If not stated otherwise, the surface unit cells, and k-point sampling summarised in Table A.1 were used.

A.1.1 vdW-DF calculations

For the vdW-corrected calculations we used the same parameters as for the non-corrected PW91 calculations, as described above. Furthermore, the lattice constant of the copper substrate was adjusted to the optimised lattice constant for the vdW-DF with revPBE and PBE, which was found to be 3.719Å for the revPBE+vdW and 3.683Å for PBE+vdW. This is to be compared to the optimised lattice constant calculated with PW91 of 3.635Å.

A.1.2 Grimme calculations

The Grimme correction from 2006 [77] was used in these calculations, which is described in more detail in Section 2.2.4. The correction was only applied between atoms within the molecules, and atoms in the molecules with the atoms of the outermost copper layer. Hence interactions between the Cu atoms were neglected, to avoid a contraction of the Cu substrate. The number of Cu layers included in the Grimme correction was reduced to one to mimic the screening from the substrate, which has shown to lower the vastly overestimated adsorption

Table A.1: Summary of surface unit cell k-point sampling used, if not stated otherwise, in the calculations of the different structures based on either the TAPP or the DPDI molecule. The surface unit cells are expressed in the matrix representation [132], as well as via the lengths of the two unit cell vectors. The k-point sampling refers to a Monkhorst-Pack sampling translated to be centered around the Γ-point.

	Surface unit cell		k-point sampling
	Matrix	Size (Å^2)	
TAPP			
Porous network	$\begin{pmatrix} 8 & 5 \\ -1 & 6 \end{pmatrix}$	17.99×16.85	2×2
Polymeric chains	$\begin{pmatrix} 5 & 0 \\ 0 & 8 \end{pmatrix}$	12.85×20.56	2×1
DPDI			
Isolated molecules	$\begin{pmatrix} 7 & 0 \\ 0 & 9 \end{pmatrix}$	18.41×23.67	1×1
Porous network	$\begin{pmatrix} 10 & 0 \\ 0 & 10 \end{pmatrix}$	25.70×25.70	1×1

energy, but without having any considerable structural effects [122].

A.2 Adsorption of a single DPDI molecule on Cu(111)

Figure A.1 illustrates the different adsorption geometries considered for the isolated DPDI molecule on the Cu(111) surface. The adsorption energies of these structures, the height of the amine and imine nitrogen atoms, as well as the chemical shift between the two types of nitrogen atoms is summarised in Table A.2. The adsorption energy was defined as

$$E_{\text{ads}} = E_{\text{DPDI/Cu(111)}} - \left(E_{\text{DPDI}} + E_{\text{Cu(111)}}\right), \tag{A.1}$$

where $E_{\text{DPDI/Cu(111)}}$ is the total energy of DPDI adsorbed on Cu(111), E_{DPDI} is the total energy of the isolated DPDI molecule, and $E_{\text{Cu(111)}}$ is the total energy of the isolated Cu(111) surface.

The most stable adsorption geometry (e) in Figure A.1, with an adsorption energy of -0.54 eV is only 20 meV more stable than the adsorption geometry (d). These two structures are also the ones best correlating with the XSW and XPS experiments.

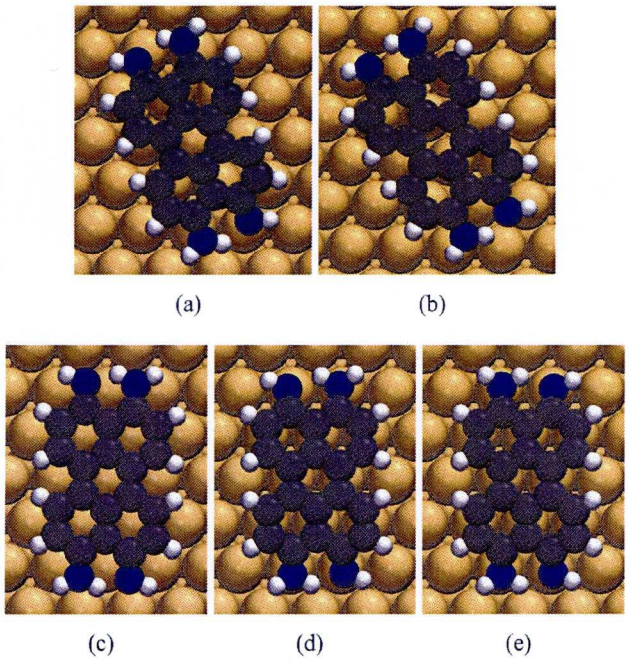

Figure A.1: Configurations investigated of the isolated DPDI molecule adsorbed on Cu(111). The calculated adsorption energies of the structures (a-e) are given in Table A.2, showing that structure (e) is the most energetically favourable adsorption configuration.

Table A.2: Calculated adsorption energies, core-level shifts of the amine (NH) and imine (NH_2) nitrogen atoms, as well the height above the first Cu layer of the amine and imine nitrogen atoms, for the different adsorption configurations of the isolated DPDI on Cu(111) shown in Figure A.1. The core-level shifts are given relative to the core-level binding energy of the amine nitrogens of structure (e) which was found to be the most energetically stable adsorption configuration.

	Adsorption energy (eV)	Core-level shift (eV)		Height above first Cu-layer (Å)	
Structure:		NH	NH_2	NH	NH_2
(a)	-0.46	-0.02	1.56	2.39	3.03
(b)	-0.25	-0.61	1.14	3.39	3.46
(c)	-0.24	-0.61	1.15	3.41	3.50
(d)	-0.52	0.00	1.85	2.29	2.41
(e)	-0.54	0.00	1.87	2.31	2.42

B

Appendix to Chapter 5

B.1 Computational details

All calculations were done within the framework of periodic density-functional theory using the Vienna Ab-initio Simulation Package (VASP) [131]. The ion-core intraction was described by the projector augmented waves method [95,96] and the generalised gradient approximation through the Perdew Wang 91 (PW91) functional [9] was used to describe exchange-correlation effects. All calculations were spin-polarised, the plane-wave basis set was expanded up to 400 eV and the structural optimisation was done until the force on each atom was less than 0.05 eV/Å. The copper (110) substrates were modelled by four layer slabs separated a vacuum region of 14 times the lattice spacing, and a 3×4 surface unit cell together with a 4×4 k-point sampling was used.

C

Appendix to Chapter 6

C.1 Computational details

C.1.1 DFT calculations

The revPBE results needed for the vdW-DF were obtained using the VASP package [131]. The PBE results needed for the semi-empirical schemes; Tkatchenko-Scheffler (TS) [79], Grimme [77], Wu-Yang (WY) [76] and Ortmann-Bechstedt-Schmidt (OBS) [78] schemes, were obtained using the all-electron code FHI-aims [133]. The calculations use a supercell approach, with integration settings converged to less than 1 meV/atom: A 2×2 k-point sampling is used for all systems, except for graphene with a 12×12 k-point grid. All VASP calculations have a plane wave energy cutoff of 450 eV, while the FHI-aims calculations use the internal *tight* species defaults. The supercell height is 35 Å in all calculations. Comparison between FHI-aims and VASP shows meV agreement in total binding energies, which confirms the overall convergence of these settings.

The vdW-DF is designed to take care of all non-local (including semi-local) correlation energies. To avoid double counting the GGA correlation energy is replaced by the LDA correlation energy. The GGA and LDA correlation energy and the non-local correlation energy was calculated non self-consistently using the pseudo-valence plus the pseudo-core density from the self-consistent revPBE calculation. The numerically challenging six-dimensional integral in the vdW-DF was evaluated following the approach by Gulans and coworkers [74] which was included in the VASP calculations using the Atomic Simulation Environment [104].

The C_6 corrections were computed by adding up all C_6/R^6 terms in successively larger supercells until the total energy was converged to within 1 μeV. Available reference data has been used to verify the implementations of the C_6-corrections in the FHI-aims code.

C.1.2 Force-field calculations

Contribution by Carlos-Andres Palma at the University of Strasbourg.

All force-field calculations were performed using the program CHARMM [134]. MMFF

calculations were performed using the implementation in the c35b1 update. A 10800 graphene C-atom slab was used with periodic boundary conditions and a cutoff 200 Å to simulate an infinite graphene slab for all molecular force field calculations. Molecular geometries were minimized in the presence of the C-atom slab below 0.0001 kcal/mol in energy using the same adsorption site as in the DFT calculations. The adsorption energy was calculated by subtracting the energy calculated after displacing the molecule 100 Å away from the substrate. In CHARMM all sp^2 carbons were parameterised with atom types 21 (i.e. C-aromatic), including the graphene slab, which corresponds to standard OPLS [135] parameters for benzene, hydrogens where assigned atom types 3 (i.e. H-aromatic). Except for ethane, partial charges are -0.15 for carbons and +0.15 for hydrogens. Note that the energy of adsorption in the force field does not depend on charge parameterization since the graphene slab was not assigned any charges. For the parameterization in MMFF, all sp^2 carbons were parameterized with atom types 37 (aromatic), while graphene was assigned an atom type 2 (vinylic). Hydrogens where assigned atom types of 5 (apolar H). As with the CHARMM parametrization, the same partial charges were used and no charges were assigned to the graphene slab.

C.2 revPBE-vdW calculations of bulk graphite

The calculations of bulk graphite were done by calculating the total energy as a function of the interplanar spacing. As reference structure we used an inter-planar spacing of 14 Å. The calculations were done with the vdW-DF method together with the revPBE functional. The calculations were performed using the same settings as for the calculations of PAHs on graphene, with the exception that a $12\times12\times6$ k-point sampling was used.

The resulting interlayer spacing versus interlayer binding energy is shown in Figure C.1 showing that the vdW-DF together with revPBE gives an interplanar spacing of 3.55 Å for graphite, which is to be compared to the experimental value of 3.35 Å.

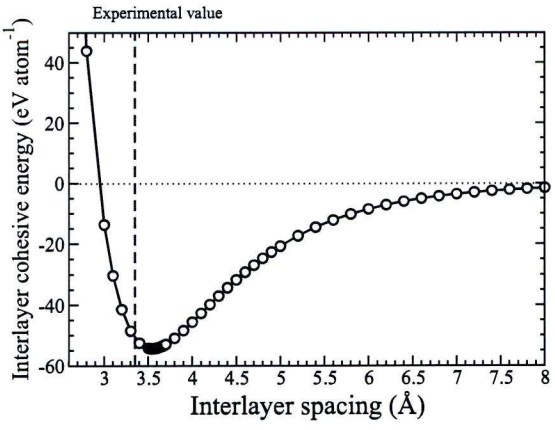

Figure C.1: Binding energy curve of the bulk graphite as a function of the spacing between the graphene planes.

C.3 Energy decompositions

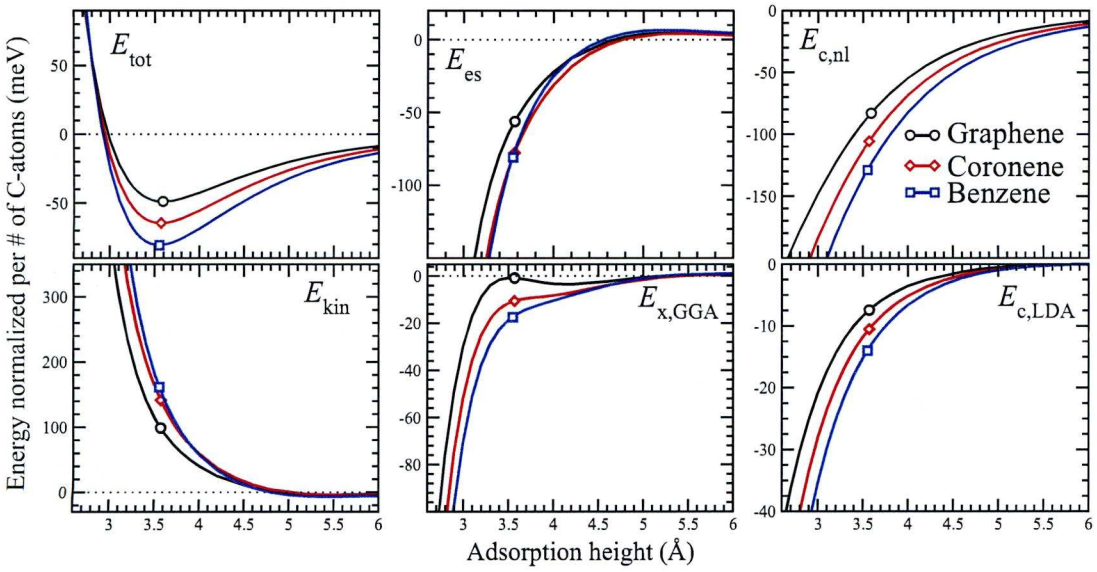

Figure C.2: The different energy components of the total vdW-DF binding energy E_{tot}: The electrostatic Coulomb energy (E_{es}), the non-local correlation energy ($E_{\mathrm{c,nl}}$), the kinetic energy (E_{kin}), the GGA-revPBE exchange energy ($E_{\mathrm{x,GGA}}$) and the LDA correlation energy ($E_{\mathrm{c,LDA}}$). The Pauli repulsion in manifested in the kinetic energy term.

C.4 Binding energies and heights

Table C.1: Surface unit cell sizes, binding heights $h_{\text{eq.}}$, total binding energies E_{bind}, and binding energies per carbon atom $E_{\text{bind}}/N_{\text{C}}$ for the PAHs adsorbed on graphene using the vdW-DF. The cell size is given as multiples of the lattice vectors of the primitive unit cell of graphene.

			vdw-DF		
Adsorbate	Formula	Cell size	$h_{\text{eq.}}$ (Å)	E_{bind} (eV)	$E_{\text{bind}}/N_{\text{C}}$ (meV)
Benzene	C_6H_6	6×6	3.55	0.485	80.8
18-annulene	$C_{18}H_{18}$	8×8	3.55	1.439	79.9
Napthalene	$C_{10}H_8$	7×6	3.59	0.729	72.9
Anthracene	$C_{14}H_{10}$	8×6	3.56	1.006	71.9
Tetracene	$C_{18}H_{12}$	9×6	3.59	1.243	69.1
Triphenylene	$C_{18}H_{12}$	8×8	3.56	1.256	69.8
Pentacene	$C_{22}H_{14}$	10×6	3.56	1.539	70.0
Pyrene	$C_{16}H_{10}$	7×7	3.60	1.071	66.9
Coronene	$C_{24}H_{12}$	8×8	3.57	1.556	64.8
Ovalene	$C_{32}H_{14}$	9×8	3.61	1.957	61.2
HBC	$C_{42}H_{18}$	10×10	3.58	2.619	62.4
Graphene	–	1×1	3.57	–	50.0

Table C.2: Binding heights $h_{\text{eq.}}$, total binding energies E_{bind}, and binding energies per carbon atom $E_{\text{bind}}/N_{\text{C}}$ for the PAHs adsorbed on graphene using the Tkatchenko-Scheffler and the Grimme schemes.

	Tkatchenko-Scheffler			Grimme		
Adsorbate	$h_{\text{eq.}}$ (Å)	E_{bind} (eV)	$E_{\text{bind}}/N_{\text{C}}$ (meV)	$h_{\text{eq.}}$ (Å)	E_{bind} (eV)	$E_{\text{bind}}/N_{\text{C}}$ (meV)
Benzene	3.33	0.575	95.9	3.27	0.415	69.2
18-annulene	3.33	1.723	95.7	3.27	1.216	67.6
Naphtalene	3.34	0.912	91.2	3.27	0.652	65.2
Anthracene	3.34	1.261	90.1	3.28	0.893	63.8
Tetracene	3.34	1.261	89.0	3.26	1.141	63.4
Triphenylene	3.33	1.602	89.3	3.27	1.126	62.6
Pentacene	3.33	1.607	89.5	3.25	1.389	63.1
Pyrene	3.35	1.970	86.0	3.27	0.986	61.6
Coronene	3.35	2.033	84.7	3.27	1.422	59.3
Ovalene	3.36	2.636	82.4	3.27	1.861	58.1
HBC	3.35	3.295	78.4	3.26	2.462	58.6
Graphene	3.35	–	76.3	3.24	–	54.2

Table C.3: Binding heights $h_{\text{eq.}}$, total binding energies E_{bind}, and binding energies per carbon atom $E_{\text{bind}}/N_{\text{C}}$ for the PAHs adsorbed on graphene using the Wu-Yang and the Ortmann-Bechstedt-Schmidt schemes.

	Wu-Yang			Ortmann-Bechstedt-Schmidt		
Adsorbate	$h_{\text{eq.}}$ (Å)	E_{bind} (eV)	$E_{\text{bind}}/N_{\text{C}}$ (meV)	$h_{\text{eq.}}$ (Å)	E_{bind} (eV)	$E_{\text{bind}}/N_{\text{C}}$ (meV)
Benzene	3.24	0.500	83.3	3.25	0.776	129.4
18-annulene	3.24	1.471	81.7	3.25	2.301	127.8
Naphtalene	3.24	0.791	79.1	3.28	1.182	118.2
Anthracene	3.24	1.088	77.7	3.29	1.592	113.7
Tetracene	3.23	1.391	77.3	3.29	2.008	111.6
Triphenylene	3.24	1.375	76.4	3.30	1.995	110.8
Pentacene	3.22	1.694	77.0	3.29	2.425	110.2
Pyrene	3.24	1.206	75.4	3.31	1.735	108.5
Coronene	3.24	1.749	72.9	3.33	2.443	101.8
Ovalene	3.24	2.295	71.7	3.34	3.155	98.6
HBC	3.23	3.034	72.2	3.33	4.414	98.6
Graphene	3.22	–	67.5	3.40	–	79.9

Table C.4: Summary of the binding heights $h_{\text{eq.}}$, total binding energies E_{bind}, and binding energies per carbon atom $E_{\text{bind}}/N_{\text{C}}$ for the PAHs adsorbed on graphene from the force-field calculations.

	CHARMM			MMFF		
Adsorbate	$h_{\text{eq.}}$ (Å)	E_{bind} (eV)	$E_{\text{bind}}/N_{\text{C}}$ (meV)	$h_{\text{eq.}}$ (Å)	E_{bind} (eV)	$E_{\text{bind}}/N_{\text{C}}$ (meV)
Benzene	3.48	0.425	70.9	3.68	0.397	66.1
18-annulene	3.5	1.280	71.1	3.7	1.151	63.9
Naphtalene	3.50	0.678	67.8	3.69	0.634	63.4
Anthracene	3.50	0.931	66.5	3.70	0.871	62.2
Tetracene	3.50	1.183	65.7	3.70	1.108	61.5
Triphenylene	3.49	1.183	65.7	3.68	1.108	61.6
Pentacene	3.52	1.435	65.2	3.70	1.345	61.1
Pyrene	3.51	1.042	65.1	3.69	0.976	61.0
Coronene	3.50	1.517	63.2	3.69	1.423	59.3
Ovalene	3.51	1.992	62.3	3.70	1.870	58.5
HBC	3.52	2.608	62.1	3.70	2.449	58.3
Graphene	3.54	–	55.5	3.72	–	52.4
12-annulene	3.5	0.848	70.7	3.7	0.792	66.0
8-annulene	3.49	0.565	70.6	3.7	0.526	65.7
4-annulene	3.48	0.282	70.5	3.72	0.263	65.8
ethene	3.5	0.172	86.0	3.70	0.160	80.0
ethyne	3.5	0.142	70.8	3.64	0.137	68.7

Acknowledgement

- First of all I like to thank my supervisor Prof. **Mats Persson** for giving me the opportunity of doing this PhD and for his guidance during the past three years. I also like to thank Dr. **Matthew Dyer** for patiently teaching chemistry to someone with a physics background and also for carefully proof-reading parts of this thesis, and Dr. **Felix Hanke** for all valuable discussions and for giving honest opinions as well as proof-reading. From our group I also gratefully acknowledge **Adolfo Fuentes**, still in the group, and Dr. **Ilja Makkonen**, now at Aalto University, Finland.

- Special acknowledgment is given to the following experimental colleagues: Dr. **Manfred Matena** at Donostia International Physics Center, San Sebastian, for the extensive discussions especially during the work on TAPP, but also for exchanging ideas about DPDI. Dr. **Meike Stöhr** at Zernike Institute, University of Groningen, for discussions during the TAPP project and for also trusting me with the DPDI project. Furthermore, **Mihaela Enache** in the group of Meike and Dr. **Jorge Lobo-Checa** at CIN2, Barcelona, made crucial contributions to the TAPP and DPDI projects and were involved in many fruitful discussions. All these people have scattered from the University of Basel where we initially met. I also like to acknowledge Prof. **Thomas Jung**, who is still in Basel.

- I also like to thank Dr. **Carlos-Andres Palma**, Dr. **Marco Cecchini** and Prof. **Paolo Samorí** at ISIS, University of Strasbourg, for the collaboration during the PAH project, and also during other projects not presented in this thesis. Especially I value the many discussions I have had with Carlos during the last years.

- Dr. **Abel Robin** and Prof. **Rasmita Raval** at Surface Science Research Centre in Liverpool are acknowledged for their nice work and the inspiring discussions during the 3CP project. I also like to thank all my friends and colleagues at the Surface Science Research Centre.

- Many thanks to **Andris Gulans** in the group of Prof. **Risto Nieminen** at Aalto University, Finland, for his implementations of the vdW-DF used in the PAH project. I also like to acknowledge **Jiri Klimes** in the group of Prof. **Angelos Michaelides** at University

College London, for his self-consistent implementation of the vdW-DF used in calculations of TAPP and DPDI.

- I gratefully acknowledge **Cliff Addison** and **Dave Love** for keeping the computer clusters in Liverpool running as well as for their prompt response to the problems that have been appearing.

- The people I like to thank the most are the ones I really got to know during the years in Liverpool. You may not have contributed scientifically, but you did make my time in Liverpool unforgettable. Special acknowledgements are given to (in alphabetic order): **Alejandro**, **Claudio**, **Ellie**, **Kay**, **Kenneth**, **Marco**, **Minos**, **Natalia**, **Paul**, **Raluca**, friends that I spent much of my time with. I also like to thank all other friends I got to know in Liverpool.

- Furthermore, I thank my landlady **Helen Green** who was the first to welcome me in Liverpool and all the people I have got to know living in Wavertree.

- Finally, I like to thank **Emma** and to my family for their love and support throughout the years.

Publications and contributions at conferences

Thesis is based on

- *Adsorption of aromatic and anti-aromatic systems on graphene through π-π stacking*
  J. Björk, F. Hanke, C.-A. Palma, M. Cecchini, P. Samori and M. Persson
  The Journal of Physical Chemistry Letters **1**, 3407 (2010)

- *STM fingerprint of molecule-adatom interactions in a self-assembled metal-organic surface coordination network on Cu(111)*
  J. Björk, M. Matena, M. S. Dyer, M. Enache, J. Lobo-Checa, L. H. Gade, T. A. Jung, M. Stöhr and M. Persson
  Physical Chemistry Chemical Physics **12**, 8815 (2010)

- *Aggregation and contingent metal/surface reactivity of 1,3,8,10-tetraazaperopyrene (TAPP) on Cu(111)*
  M. Matena, M. Stöhr, T. Riehm, J. Björk, S. Martens, M. S. Dyer, M. Persson, J. Lobo-Checa, K. Müller, M. Enache, H. Wadepohl, J. Zegenhagen, T. A. Jung and L. H. Gade
  Chemistry - A European Journal **16**, 2079 (2010)

- *Adsorption and Organization of the Organic Radical 3-Carboxyproxyl on a Cu(110) Surface: A combined STM, RAIRS and DFT study*
  A. Robin, L. Marnell, J. Bjork, M. S. Dyer, P. S. Bermudez, S. Haq, S. D. Barrett, M. Persson, A. Minoia, R. Lazzaroni and R. Raval
  The Journal of Physical Chemistry C **113**, 13223 (2009)

Other publications

- *Tailoring Bi-component Supramolecular Nanoporous Networks: The Role of Phase Segregation and Polymorphism at the Solid-liquid interface*
  C.-A. Palma, J. Bjork, M. Bonini, M. S. Dyer, A. Llanas-Pallas, D. Bonifazi, M. Persson, and P. Samori
  Journal of the American Chemical Society **131**, 13062 (2009)

- *Density functional theory based screening of ternary alkali-transition metal boro hydrides: A computational material design project*
  J. S. Hummelshoj, (...), J. Bjork, (...), T. Vegge
  The Journal of Chemical Physics **131**, 014101 (2009)

Contributions at international conferences as presenting author

- *The role of native adatoms in metal-organic coordination networks on the copper (111) surface* – **Poster**
  J. Björk, M. Matena, M. S. Dyer, M. Enache, J. Lobo-Checa, L. Gade, T. A. Jung, M. Stöhr and Mats Persson
  Psi-k conference (2010), Berlin, Germany

- *Porous metal-organic coordination networks of perylene derivatives on the copper(111) surface: Theory and experiments* – **Oral**
  J. Björk, M. Matena, M. S. Dyer, M. Enache, J. Lobo-Checa, L. Gade, T. A. Jung, M. Stöhr and Mats Persson
  European conference on surface science 27 (2010), Groningen, The Netherlands

- *The porous surface network of TAPP - Identifying adatoms and bonding mechanism* – **Oral**
  J. Björk, M. Matena, M. S. Dyer, M. Enache, J. Lobo-Checa, L. Gade, T. A. Jung, M. Stöhr and Mats Persson
  Symposium on surface science (2010), St. Christoph/Arlberg, Austria

- *Hydrogen bonding in bi-component supramolecular nanoporous networks* – **Oral**
  J. Björk, C.-A. Palma, M. S. Dyer, M. Bonini, A. Llanas-Pallas, D. Bonifazi, P. Samori, M. Persson
  Structure and dynamics of hydrogen bonded systems (2009), ICTP, Trieste, Italy

- *Adatom coordinated porous network and polymeric chains of TAPP molecules on the Cu(111) surface* – **Oral**
  J. Björk, M. Matena, M. S. Dyer, M. Enache, J. Lobo-Checa, L. Gade, T. A. Jung, M. Stöhr and Mats Persson
  European conference on surface science 26 (2009), Parma, Italy

- *Adatom driven self-assembly of TAPP molecules on Cu(111)* – **Oral**
  J. Björk, M. Matena, M. S. Dyer, M. Enache, J. Lobo-Checa, L. Gade, T. A. Jung, M. Stöhr and Mats Persson
  17th interdisciplinary conference surface science conference (2009), Reading, United Kingdom

- *Adatom driven self-assembly of TAPP molecules on Cu(111)* – **Oral**
  J. Björk, M. Matena, M. S. Dyer, M. Enache, J. Lobo-Checa, L. Gade, T. A. Jung, M. Stöhr and Mats Persson
  DPG spring meeting (2009), Dresden, Germany

- *3-carboxy proxyl on copper (110) - A density-functional theory study* – **Poster**
  J. Björk, A. Robin, M. S. Dyer, R. Raval and M. Persson
  European conference on surface science 25 (2008), Liverpool, United Kingdom